



Multiscale Modelling of Heteroepitaxial Thin Films

Tong Wang

Thesis submitted to the University of Leicester
in accordance with the requirements for the degree of
Doctor of Philosophy in the Faculty of Engineering

Supervisors: Dr. S. P. A. Gill
 Prof. A. C. F. Cocks

University of Leicester Engineering Department
Mechanics of Materials Research Group

Date of Submission: January 2006

UMI Number: U216707

All rights reserved

INFORMATION TO ALL USERS

The quality of this reproduction is dependent upon the quality of the copy submitted.

In the unlikely event that the author did not send a complete manuscript and there are missing pages, these will be noted. Also, if material had to be removed, a note will indicate the deletion.



UMI U216707

Published by ProQuest LLC 2013. Copyright in the Dissertation held by the Author.
Microform Edition © ProQuest LLC.

All rights reserved. This work is protected against
unauthorized copying under Title 17, United States Code.



ProQuest LLC
789 East Eisenhower Parkway
P.O. Box 1346
Ann Arbor, MI 48106-1346

Multiscale Modelling of Heteroepitaxial Thin Films

Tong Wang*

Mechanics of Materials Research Group,
Department of Engineering, University of Leicester,
Leicester, LE1 7RH, UK

Abstract

Multiscale models are developed to investigate the evolution of heteroepitaxial thin films at high temperatures via surface diffusion. Continuum models for the kinetics and thermodynamics are derived from atomistic potentials in chapter 2. A modified Lennard-Jones potential is used to introduce a coordination dependence to generate a surface stress. Novel hybrid atomistic-continuum models are developed in chapter 3 to investigate the static elastic field around a surface step. They have atomic scale resolution in the non-linear region around the defect. Linear elasticity is used away from the discontinuity,. An analytic force dipole model and the finite element method are chosen to represent the continuum.

The kinetics of surface evolution are then investigated using an atomistic off-lattice Kinetic Monte Carlo (KMC) model. This allows the atoms on the surface of a lattice statics simulation to evolve via diffusive events, and readily incorporates the non-linear effects of strain on the system thermodynamics and kinetics. The flattening process of a rough surface is considered in chapter 4. The results are compared with a derivative microscopic step flow model in chapter 5, which is extended to consider asymmetric steps. The parameters in the step flow model are obtained from the interatomic potentials and are used to determine the macroscopic surface mobilities.

The evolution of strained surfaces is investigated in chapter 6. The surface is found to be stable below a certain strain magnitude, in contradiction of the predictions of conventional theories. A new theory based on a discontinuous (cusped) surface energy orientation function is proposed to explain this. At high strains roughening of the film leads to the formation of sharp valleys. These stress concentration features are preferred sites for the nucleation of dislocations. The nucleation process is modelled along with the subsequent rearrangement of surface material due to the local strain relaxation.

Keywords:

Multiscale modelling, heteroepitaxial thin film, Off-lattice KMC, surface evolution, dislocation formation.

* E-mail: tongwng@hotmail.com

Acknowledgements

I would like to thank my supervisors, Dr. Simon Gill and Professor Alan Cocks, for their advice and support during my PhD project. Dr. Gill has given me much training in the field of materials modelling. His Java code has made my simulation results look beautiful and has allowed me to focus on new research areas. Professor Cocks introduced me to this new, challenging research field and motivated me to explore material modelling. I am grateful for my supervisors' support and patience. I would also like to acknowledge the UK Engineering and Physical Science Research Council (EPSRC) for financial support.

I would like to thank Dr. Paul Spencer for his help with the atomistic models and computer officer Dr. Phil Brown for his support of the Unix-system, because much of my computational work was performed on our groups 6-cpu SGI Origin2000 server. I would also like to extend my thanks to my colleagues within the Mechanics of Materials group and other groups in the Department of Engineering at the University of Leicester.

Lastly I would particularly like to thank my wife, Dan Liu, and my daughter, Danyu, for their encouragement and support, and my parents in China for their continued support.

CONTENTS

ABSTRACT I

ACKNOWLEDGEMENTS II

0.0 INTRODUCTION 1

1.0 INTRODUCTION TO SURFACES..... 3

1.1 Surface phenomena3

 1.1.1 Surface characterization.....3

 1.1.2 Relaxation and reconstruction of surface.....5

 1.1.3 Roughening transition temperature.....7

 1.1.4 Strained surfaces, heteroepitaxy and surface roughening.....7

1.2 Surface models10

 1.2.1 Atomistic surface models.....11

 (a) Inertial methods.....12

 (b) Non-inertial methods12

 1.2.2 Continuum surface models13

 1.2.3 Multiscale surface models.....15

 (a) Step flow models.....15

 (b) The quasicontinuum method.....16

 (c) Coarse-Grained Molecular Dynamics (CGMD)17

 (d) Accelerated Molecular Dynamics.....17

2.0 AN ATOMISTIC SURFACE MODEL..... 18

2.1 Interatomic potentials18

 2.1.1 Lennard-Jones (LJ) potential18

 2.1.2 Lennard-Jones with bond-order (LJ+BO) potential.....19

2.2 Bulk properties (“closed box”) for LJ potential20

 2.2.1 The fundamental cell.....20

 2.2.2 Analytical solutions of Young’s modulus and Poisson’s ratio22

 2.2.3 Non-linear excursions of the bulk strain energy density24

2.3 Surface properties (“open box”) for LJ potential.....24

 2.3.1 Surface energy and surface stress25

 (a) Surface energy.....25

 (b) Surface stress27

 2.3.2 Non-linear surface effects for LJ potential29

2.4 Surface properties for LJ+BO interatomic potential.....29

2.4.1 Analytical solution	30
2.4.2 Non-linear surface effects for the LJ+BO potential.....	32
2.5 Relaxation of a circular atomic cluster	32
2.5.1 Analytical solution	33
2.5.2 Numerical method.....	34
3.0 ANALYSIS OF A SURFACE STEP	37
3.1 Continuum force dipole model	38
3.2 A mixed atomistic and continuum force dipole model.....	39
3.2.1 The Model.....	39
3.2.2 Surface stress in the continuum dipole model	41
3.2.3 Numerical results for mixed atomistic-dipole model.....	42
3.3 Combined atomistic and finite element models	43
3.3.1 Using the Finite Element Method (FEM) in the continuum region.....	44
3.3.2 Surface transformation strain	45
3.3.3 Numerical implementation.....	47
3.3.4 Results and discussion	48
3.3.5 Summary	51
4.0 AN ATOMISTIC MODEL OF SURFACE DIFFUSION	52
4.1 Introduction	52
4.2 An off-lattice KMC model for surface diffusion.....	53
4.2.1 The on-lattice KMC model	53
4.2.2 The off-lattice KMC model	55
4.3 Calculating the activation energies	57
4.3.1 Adatom diffusion on an unstrained flat surface	57
4.3.2 Diffusion on a strained flat surface	59
4.3.3. Attachment/detachment to/from surface steps.....	61
4.4 Decay of an unstrained sinusoidal surface	67
4.4.1 Off-lattice KMC simulations	67
4.4.2 Flattening of a long wavelength sinusoid ($N_x=150$).....	70
(a) High temperature regime ($\bar{T}=0.3-0.45$)	70
(b) Low temperature regime ($\bar{T}=0.1-0.108$).....	72
4.4.3 Flattening of a short wavelength sinusoid ($N_x=61$).....	76
(a) High temperature regime ($\bar{T}=0.3-0.45$)	76
(b) Low Temperature Regime ($\bar{T}=0.1-0.108$).....	79
4.5 Discussion of simulation results for the decay of an unstrained sinusoidal surface.....	82
4.6 Summary	84

5.0	STEP FLOW MODELS OF SURFACE DIFFUSION.....	85
5.1	Basic step flow model for symmetric steps.....	85
5.1.1	Diffusion Limited versus Attachment-Detachment Limited Growth	87
5.2	Macroscopic constants from interatomic potentials	87
5.2.1	Equilibrium concentration of adatoms near a non-interacting step, \tilde{C}^{eq}	87
5.2.2	The attachment-detachment rate, k	89
5.2.3	The terrace diffusion coefficient, D_s	90
5.3	An asymmetric step flow model	91
(a)	The model	91
(b)	The step flow parameters	92
(c)	A simple macroscopic DL model.....	95
(d)	ADL growth.....	96
5.4	Elastic interaction from force dipole model.....	96
5.5	Step flow simulations of the decay of an unstrained sinusoidal surface.....	98
5.6	Summary	104
6.0	DIFFUSION ON STRAINED SURFACES.....	105
6.1	Morphological change.....	105
6.2	Stability of strained surfaces	106
6.2.1	Continuum theory	106
6.2.2	Roughness parameters	110
(a)	RMS roughness	110
(b)	Height-height correlation function.....	110
6.2.3	Off-lattice KMC simulation	111
(a)	Roughening of an LJ surface	112
(b)	Roughening of an LJ+BO surface	115
(c)	Comparison between the roughening wavelength of the LJ and LJ+BO surfaces	119
6.3	Relaxation of a rough surface by dislocation nucleation	120
(a)	Formation of a single dislocation.....	121
(b)	Formation of multiple dislocations	124
6.4	Summary	127
7.0	DISCUSSION AND CONCLUSIONS.....	129
APPENDIX	134
A	: Elastic constants from the atomistic model.....	134
B	: The displacement on the boundary.....	136

C : The relationship between the strains and displacements	137
C.1 Three-noded triangular element	137
C.2 Six-noded quadratic triangular element	139
D : Gaussian Quadrature.....	141
E : Surface diffusion and shape change.....	143
F : Orientational dependence of the surface energy for an unstrained surface .	145
F.1 An LJ surface	145
F.2 An LJ+BO surface	146
G : Newton-Raphson scheme for atomistic energy minimization.....	148
REFERENCES:.....	152

0.0 INTRODUCTION

Semiconductor thin films are the main components for fabricating modern electronic and optoelectronic devices. The performance of a device can be enhanced by a process known as ‘strain engineering’ for heteroepitaxial thin film systems. Epitaxy comes from the Greek words ‘epi’ meaning ‘on’ and ‘taxis’ meaning ‘arrangement’. Thin films are formed by the deposition of the film material on to an underlying substrate. In epitaxial systems, the film adopts the lattice structure (arrangement) of the substrate. Heteroepitaxial systems are ones in which the film and substrate are different materials with the same lattice structure but different lattice spacings. The film is consequently strained to be coherent with the substrate. This elastic mismatch strain dramatically affects the kinetics and thermodynamics on the film surface. At high temperatures a film will evolve to relieve this strain leading to a strain-induced morphological instability [1][2]. The competition between the elastic strain energy and the surface energy favours surface roughening at a particular wavelength. This is a promising processing route for producing self-organized nanostructures, such as quantum dots, which are difficult to be produced by standard lithographical techniques [3][4].

The promise of this type of nanotechnology to open up a new frontier in device performance has motivated many researchers in the fields of engineering, mechanics, physics, chemistry and mathematics to investigate the rich diversity of mechanical and electrical behaviour at the nanoscale in the last two decades. The influence of surfaces naturally becomes more important at small scales as the surface to volume ratio increases. Hence better understanding of surfaces is imperative for developing methodologies for controlling the evolution of surface morphologies, compositions and defect structures in heteroepitaxial thin films.

There are traditionally two separate approaches to modelling the evolution of surfaces: continuum models and atomistic models. Continuum models use macroscopic conservation laws and constitutive relations in order to obtain analytical and/or numerical predictions of material behaviour, e.g. [5]-[8]. They have been very successful for solving solid and fluid mechanics problems at the macroscopic length scale. They are, however, increasingly inaccurate as the length scale is reduced to the nanometer scale. This is particularly true near defects or discontinuities such as dislocation cores, crack tips, and steps on a surface. Full

resolution is only achieved through atomistic simulations [9]-[11] which can accurately model the physical processes underlying the materials behaviour. However, these methods are very restrictive on the size and simulation time of the models due to the large computational overhead.

In recent years, alternative modelling approaches have been developed to couple atomistic and continuum models [12]-[18] and smoothly pass information up the hierarchy of length and time scales. Step models [19]-[22] are a further step towards representing the inherent discreteness of surfaces at the atomic scale. They resolve the discontinuities in the surface (steps) individually and use classical elasticity theory to describe their interactions. The quasicontinuum method goes further by employing an atomistic description in the vicinity of the step where classical theory breaks down, and a classical continuum description to represent the equilibrium response due to the far field deformation. The bridge between the atomistic and continuum models needs to be carefully constructed to consistently transfer information between them.

The work in this thesis develops alternative models for the evolution of elastically strained surfaces and compares them with the predictions of results obtained using traditional approaches. There is a brief overview of some of the common physical phenomena observed on strained surfaces in Chapter 1, along with a discussion of the main modelling techniques. Macroscopic surface parameters are derived from atomistic models in Chapter 2 to develop a consistent continuum model. The elastic field around a single static surface step is investigated using novel hybrid atomistic-continuum models in Chapter 3. Atomistic simulations of sinusoidal surface evolution are presented in Chapter 4 and compared with a derivative step flow model in Chapter 5. Finally Chapter 6 models the strained surface roughening process through large morphological change and looks at the critical conditions for the nucleation of defects.

1.0 INTRODUCTION TO SURFACES

This chapter provides a brief review of some of the common surface phenomena that are observed on atomistic surfaces which are generally not accounted for in continuum representations of a surface. This is followed by a summary of current modelling techniques used in the analysis of surfaces.

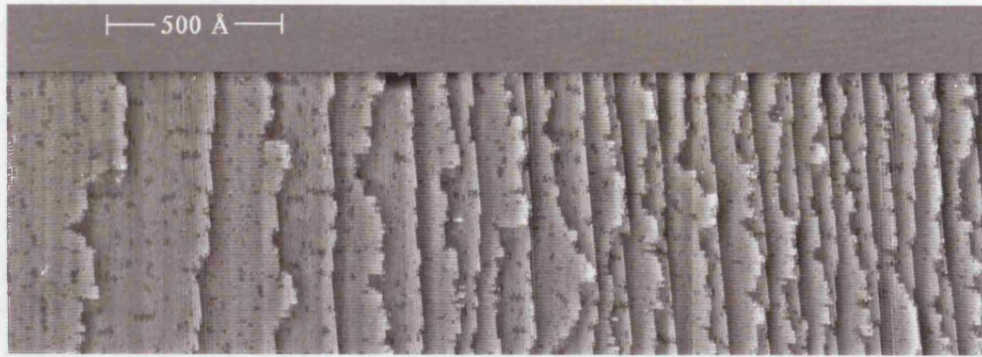
1.1 Surface phenomena

Surface physics has become an important branch of microscopic solid-state physics. This is a consequence of the development of advanced microscopy and experimental techniques. Semiconductor surfaces (or interfaces) are important as they exhibit unique electronic and optical properties which have important potential applications in novel microelectronic devices.

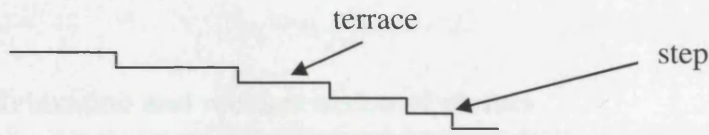
1.1.1 Surface characterization

From a mechanical perspective, an atomistic surface is characterised by the distribution of surface steps, the structure of those steps and the interactions between them. Figure 1.1(a) shows a picture of an Si(001) surface imaged by a Scanning Tunnelling Microscope (STM) [19]. The schematic side view shown in Figure 1.1(b) illustrates a simplified representation of this surface in two-dimensions (2D) as a number of steps separated by terraces. This 2D model necessarily assumes that the step fronts are straight which, as Figure 1.1(a) shows, is not always the case.

In practice semiconductor devices are fabricated on vicinal surfaces which have a small miscut angle from a high symmetry plane. Such surfaces generate a substantial density of steps. Elastic interactions between the steps can lead to step bunching under some conditions [24], as shown in Figure 1.2. Tersoff et al. [25] simulated the evolution of step-bunching based on Burton-Cabrera-Frank (BCF) theory [26]. The predicted evolution of the surface morphology is shown in Figure 1.3(a). Initially steps collect in small bunches but then the bunches progressively coarsen into larger bunches over time. Hence the number of steps bunching together rises over with time as in Figure 1.3(b). See reference [27] for a recent review on developments in this area.



(a)



(b)

Figure 1.1 : (a) Picture of an Si(001) surface [19]. (b) Schematic side view of (a) showing surface can be represented in 2D as a number of steps separated by terraces.

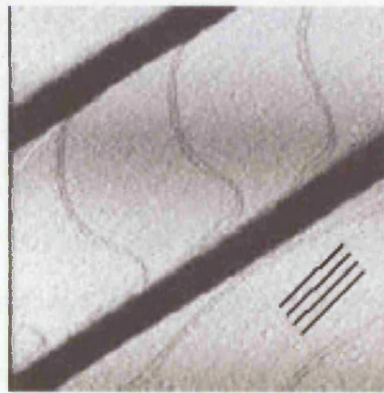


Figure 1.2 : A $15 \times 15 \mu\text{m}$ Atomic Force Microscopy (AFM) image of an Si(001) surface heated to 1040°C for 18h with the direction current applied along the [010] direction. The black bands are the step bunched regions. The bright regions between two bunched regions are the surface terraces [24].

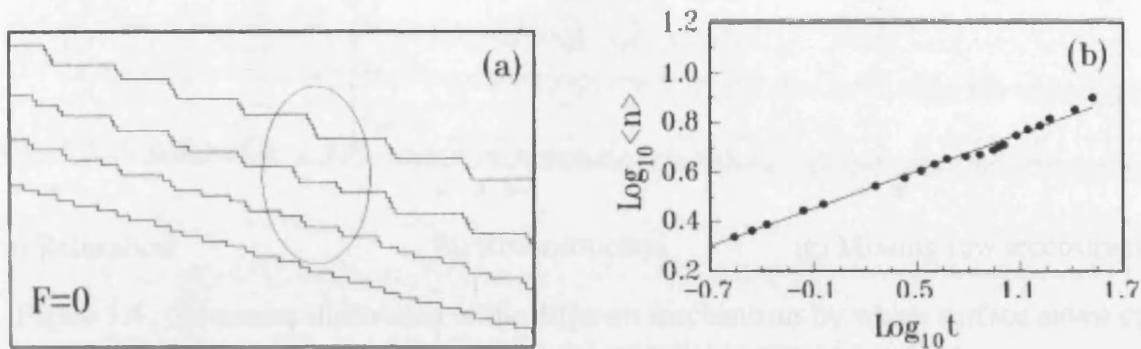


Figure 1.3 : Simulation of step-bunching [25]. (a) Surface morphology at evolution time $F=0$, 0.1, 0.7 and 4.7 from bottom to top, (b) Step-bunching size $\langle n \rangle$ vs time.

1.1.2 Relaxation and reconstruction of surface

This subsection describes the atomic structure of a surface in more detail. Unlike bulk atoms, surface atoms do not have full coordination with neighbouring atoms. Due to the absence of neighbouring atoms on one side, the interatomic forces in the uppermost lattice places are changed. The equilibrium position for surface atoms is different than that for bulk atoms. This type of lattice relaxation [28] is illustrated in Figure 1.4(a) for a simple cubic lattice with bulk lattice constant a . The topmost atomic layers relax normal to the surface by adopting a slightly different lattice spacing. Another surface relaxation process, common in covalently bonded semiconductors, is surface reconstruction. In Figure 1.4(b) the topmost atomic layer is reconstructed into a surface net with double periodicity distance $2a$ to minimize the total potential energy of the body. In Figure 1.4(c) the topmost atomic layer has alternatively empty rows. One of the most complex and beautiful surface reconstructions is the (7×7) reconstruction on the Si(111) surface [29] illustrated in Figure 1.5.

From a macroscopic point of view, surface reconstruction is considered as a phase transition in which surface energy and surface stress are discontinuous functions of strain and temperature. Recent experiments have been done by Brihuega et al. [52] to investigate the (3×3) to $(\sqrt{3} \times \sqrt{3})$ reversible phase transition of Pb on Si(111) surface by means of variable temperature scanning tunnelling microscopy as shown in Figure 1.6. It tracks the same surface region over various temperatures so that the transition can be observed directly.

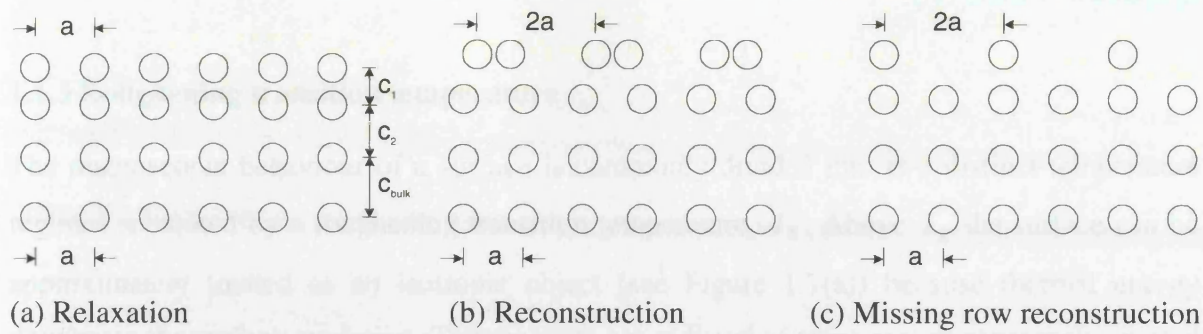


Figure 1.4 : Schematic illustration of the different mechanisms by which surface atoms can rearrange to minimize the total potential energy of a surface.

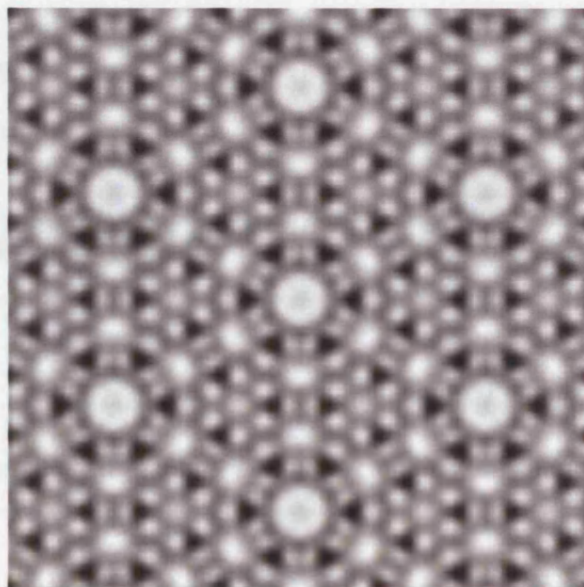


Figure 1.5 : High Resolution Electron Microscope (HREM) image of a (7×7) reconstruction on the Si(111) surface [29].

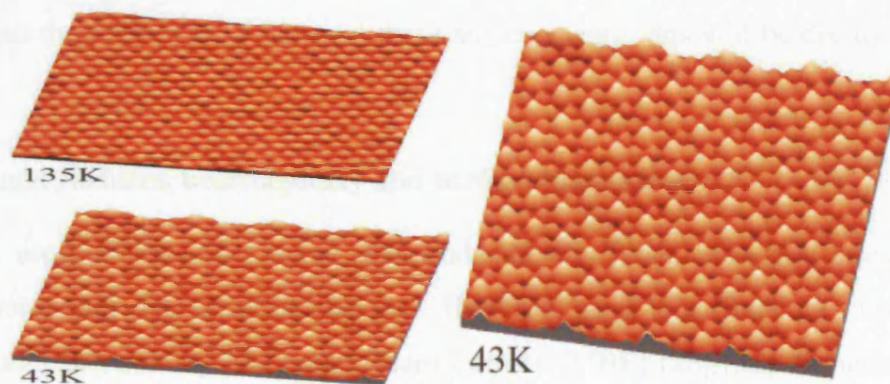


Figure 1.6 : Phase transitions of Pb on a Si(111) surface [52].

1.1.3 Roughening transition temperature

The macroscopic behaviour of a surface is commonly divided into two distinct temperature regimes separated by a roughening transition temperature, T_R . Above T_R the surface can be approximately treated as an isotropic object (see Figure 1.7(a)) because thermal energy dominates the surface evolution. Terrace sizes are reduced as steps are spontaneously created everywhere and the behaviour of individual steps becomes less important. Macroscopically it is observed that faceting of surfaces is reduced or even completely disappears. These observations are well explained by the widely used Herring-Mullins continuum theory in which the surface energy is a constant or a smooth function of orientation. This is discussed in more detail in Chapter 5.

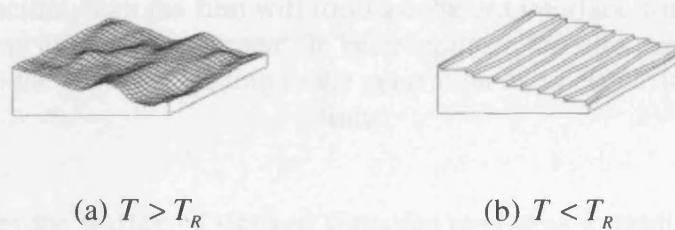


Figure 1.7 : Schematic illustration of equilibrium crystal shapes at finite T [32].

However, the situation is different below T_R . Surface energy dominates over thermal energy and governs the surface evolution. The evolution is therefore regulated by the behaviour of the steps. Macroscopically this causes the surface to adopt a faceted morphology. There are sharp cusped minima in the surface energy at particular orientations which favour the formation of facets at these angles. Again, this will be discussed further in Chapter 5.

1.1.4 Strained surfaces, heteroepitaxy and surface roughening

Thin films, especially heteroepitaxial semiconductor thin films, are widely used to fabricate microelectronic and optoelectronic devices. Heteroepitaxial thin films are most commonly deposited on a substrate by Molecular Beam Epitaxy (MBE) [28]-[31]. In heteroepitaxy the atomic lattice constant of the deposited film material is different from that of the substrate material. This is illustrated in Figure 1.8. Mismatch in heteroepitaxial thin films can generate

large elastic strains, e.g. in typical systems such as $\text{Si}_{1-x}\text{Ge}_x$ the strain is 4.2%, and in $\text{In}_x\text{Ga}_{1-x}$ as the strain is as high as 7%. This strain can enhance the electronic and optical properties of the subsequent device. The strain can be adjusted by altering the composition x of the film in a process known as ‘strain engineering’.

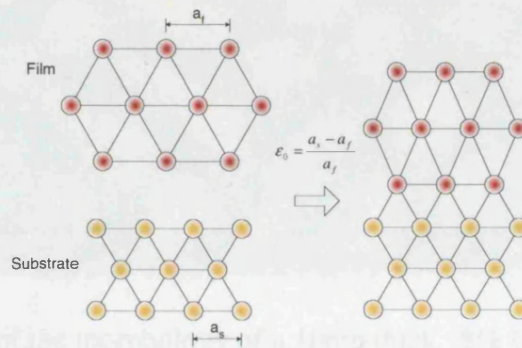


Figure 1.8 : If a film material is epitaxially deposited on to a substrate material with a similar crystal lattice structure, then the film will form a coherent interface with the substrate and adopt the underlying atomic arrangement. In heteroepitaxy, the film material has a different lattice constant than the substrate leading to the generation of an elastic mismatch strain in the film.

At high temperatures the surface of strained films can evolve as a result of kinetic processes, predominantly surface diffusion. The evolution is driven by the elastic mismatch strain. The initially flat surface of a stressed solid is unstable and causes the profile to roughen. The strain energy is minimised if the surface roughens with the smallest wavelength possible. However surface energy favours a flat surface (no roughening). The consequence of this competition between the two driving forces is a strong preference for a system to roughen at a particular wavelength [1][2][33]-[35]. This is clearly illustrated in Figure 1.9 which shows an AFM image of the morphology of a 10nm thick 18% Ge film annealed at 850°C for 5 min [50]. The surface has roughened and produced an undulating profile with a remarkably regular spacing of about 200nm. The smoothness of the profile indicates that the surface energy is fairly isotropic, i.e. independent of surface orientation. This suggests that the temperature is above T_R . The length and time scales associated with surface roughening are determined by the thermodynamics and the kinetic processes. In different case, some other driving forces and kinetic processes may be involved [36][37].

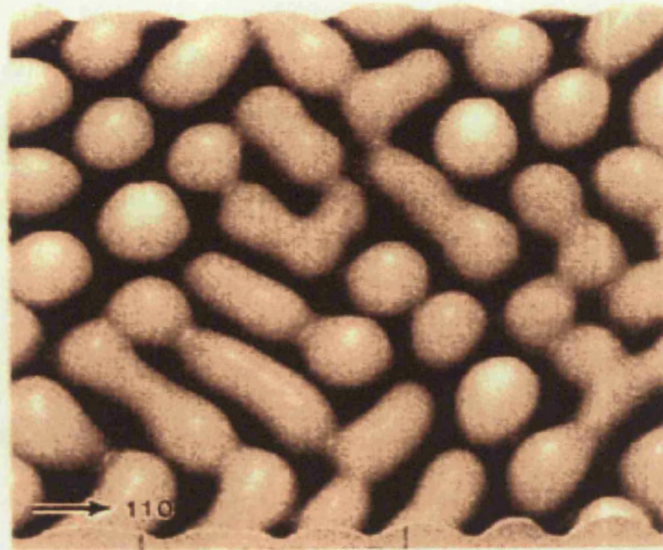


Figure 1.9 : AFM image of the morphology of a 10nm thick 18% Ge film annealed at 850 °C for 5 min due to surface roughening promoted by a 0.75% elastic mismatch strain [50].

The experiments by Floro et al [51] of a 20% Ge film deposited on a Si(001) buffer layer at a lower temperature of 750°C show the evolution of strain driven coherent islands during heteroepitaxial growth due to surface roughening, as shown in Figure 1.10. After only a small amount of material has been deposited, it can be seen in Figure 1.10a that a regular array of islands have formed. Unlike Figure 1.9 they are square-based pyramids with (501) facets. The surface energy dominates at this smaller scale and the lower temperature promotes facet formation. As more material is deposited, the shapes of the islands change from small huts to larger domes. This is because the islands start to impinge and repulsive elastic interactions between them become more important and larger islands are favoured.

These self-organised nanostructures, in which a periodic array of islands with a narrow size distribution is formed, are a potentially useful processing route for nanoengineered devices. If the islands are below about 50nm in width then they are known as 'quantum dots'. This is because they exhibit unique electronic properties due to quantum effects that are significant at this scale. For example, InGaAs dots have been demonstrated to produce lasers with light of a constant wavelength which is independent of temperature. This is potentially beneficial for use in fibre-optic communications networks, which currently require expensive control circuitry to compensate for changes in the wavelength with fluctuations in temperature.

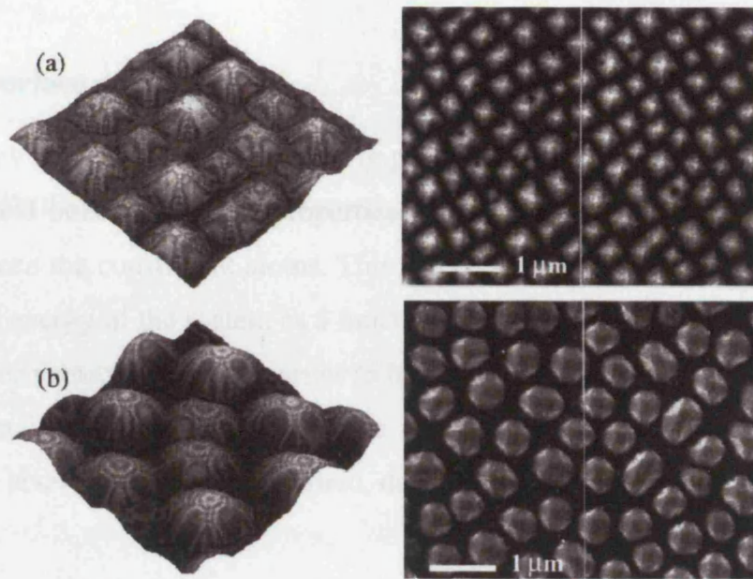


Figure 1.10 : Hut to Dome transition in $Si_{1-x}Ge_x / Si(001)$ with $x=0.2$ at 750°C . AFM & SEM images of (a) hut clusters (104\AA deposited) and (b) dome clusters (275\AA) [51].

1.2 Surface models

The sub-section gives a brief introduction to different modeling techniques. These surface models are classified as either atomistic, continuum (meaning macroscopic) or multiscale (indicating a continuum model incorporating an atomistic length or time scale). As illustrated in Figure 1.11, traditional models are pertinent to a particular single scale.

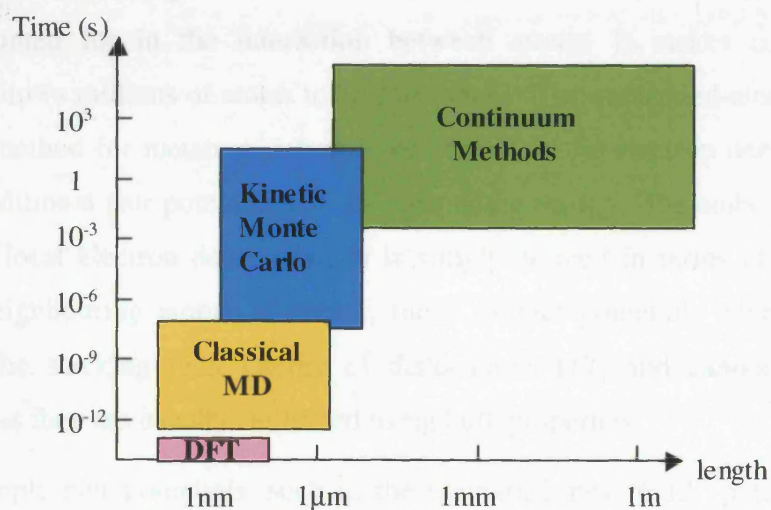


Figure 1.11 : A simple schematic diagram showing the current regions of application for different classical modeling methods.

1.2.1 Atomistic surface models

Material properties such as kinetic properties (e.g. surface diffusivity), surface properties (e.g. surface energy) and bulk mechanical properties (e.g. Young's modulus) are defined by the interactions between the constituent atoms. This can be expressed mathematically in terms of the total potential energy of the system as a function of the atomic coordinates. This permits a relationship between structure and properties to be constructed. The fundamental input into an atomic simulation is therefore the interatomic potential. As discussed below, the type of potential, and the level of complexity required, depends on the subtlety of the features that are being modelled.

Ab-initio (or first principles) methods are based on the laws of quantum mechanics. They can calculate the geometric and electronic structure of an atomic system simply from the most basic knowledge of the atomic number of the constituent atoms by solving Schrödinger's equation. A popular, simplified ab-initio method is (electronic) density functional theory (DFT) in which a description of all the electrons in the solid is reduced to the problem of determining the correct electron density. There are very high computational overheads associated with this method. Typically, it is restricted to 10~100 atoms [40]. Low-level methods such as these are required to accurately model some surface features such as surface reconstructions.

Empirical interaction potentials can be attractive to modellers as the electrons are not explicitly accounted for in the interaction between atoms. It makes computations less expensive and allows millions of atoms to be considered. The embedded-atom method [41] is a higher order method for metals which does not calculate the electron density explicitly. It consists of a traditional pair potential and the embedding energy. The embedding energy is a function of the local electron density which is simply defined in terms of the number and proximity of neighbouring atoms. However, these simpler potentials have been shown to underestimate the stacking fault energy of dislocations [17] and cannot predict surface reconstructions as they are usually calibrated using bulk properties.

Very simple pair potentials, such as the Lennard-Jones "6-12" potential, have been widely employed to describe rare-gas atoms and simple metals systems. However, this has no environmental dependence, such that the difference between behaviour on the surface and in the bulk is not accounted for [9]. In general, the more neighbours an atom has, the weaker the

bond to each neighbour will be [42]. For example, in the case of a free surface, the strength of surface atom bonds to their neighbours is bigger than the bonds of their bulk counterparts. This effect can be simply modelled by introducing a bond order term, which makes the pair potential a function of the atoms co-ordination number.

For covalent systems, such as semiconductors, a coupled two- and three-body interatomic potential is used. Three-body potentials have a dependence on the angle between bonds. One example is the Stillinger-Weber potential for Si [43]. This potential has been successfully applied in some range of atomistic simulation [43]-[46] although it cannot describe the behaviour of nantetrahedral silicon [47].

The different types of atomic simulation can be classified into inertial (dynamic) and non-inertial (quasi-static) methods.

(a) Inertial methods

Molecular Dynamics (MD) is used to model the kinetics of atomic rearrangement at finite temperature. The forces between atoms are computed from the spatial derivative of the total potential energy. The trajectories of the atoms are integrated over time using Newtons' law [49] given the mass of the atoms. Very large scale classical MD simulations can model up to 100 million atoms for up to a few nanoseconds.

(b) Non-inertial methods

At zero temperature, the method of Lattice Statics (LS) can be used to find the equilibrium configuration of an atomic lattice. The basic idea of the Lattice Statics approach is to compute the total energy of the system (sum of the interatomic potentials) in the vicinity of some local minimum. The total energy is then minimised as a function of the atomic displacements. The mass of the atoms actually plays no part in this method.

The Monte Carlo (MC) method offers a method for studying the evolution of such atomic systems over long time scales. This is a practical method for studying infrequent events such as diffusional rearrangement. The MC method can generate configurations of a system with the correct equilibrium statistical distributions if kinetics are not important. A number of possible events are allowed and the energy change associated with each event prescribed. Events are randomly chosen. If the energy decreases then the event is accepted, if the energy increases then the event is only accepted with a certain probability. There is no connection between the events chosen and real time so it is not applicable to kinetic models.

In many systems, the kinetics are critical in determining the final equilibrium state that it evolves to, if it reaches a final equilibrium state at all. In many processes, the time required to reach equilibrium is also of interest. Hence it is necessary to consider the driving force (energy change) and the kinetics to model the evolution of a dynamic system correctly. Kinetic MC has been developed to solve these problems [69][70]. This uses Harmonic Transition State Theory (HTST) to determine the transition rates between states from the transition energy barrier between the states. The probability of an event occurring is weighted according to its transition rate. Events are picked from this probability-weighted list of events. Hence the faster events are more likely to be picked and hence more likely to occur. Time is correctly incremented between events according to a Poisson distribution. Thus the two ingredients in the KMC method are the identification of all of the possible events in the system and the determination of the rates at which these events occur.

In the last few years, the off-lattice KMC model [71][72] has been developed to investigate island growth in heteroepitaxial thin film systems. It is based on a real crystal lattice and allows for continuous particle positions. It uses real interatomic potentials and hence the transition energies between states can be calculated exactly for any event. Thus it can faithfully include the effect of strain and defects and correctly represent the underlying physics of strain-induced film growth. The off-lattice KMC model is explained more fully in Chapter 4.

1.2.2 Continuum surface models

A continuum or macroscopic description of surface evolution is commonly used due to its simplicity and ability to cover a range of length and time scales. It can even be used to reasonably predict features close to the atomic scale in a few cases, such as the critical size for the nucleation of stable clusters. However, it is best suited to the representation of large collections of atoms undergoing (relatively) large scale rearrangement where particular details of the atomic surface are not important. This is most applicable above the roughening transition temperature, T_R .

The relaxation of a (1+1)D¹ unstrained sinusoidal surface has been widely investigated. Surface energy is the only significant driving force. This causes the surface to evolve towards a state which minimizes its surface area, i.e. it flattens. Above T_R , the wavy

¹ A two-dimensional model will naturally consider a one-dimensional surface. This type of surface model is commonly known as a (1+1)D model. In three-dimensions, the two-dimensional surface model is known as a (2+1)D model.

surface can be treated as an isotropic object, because terrace diffusion dominates the process at that high temperature and moving up and down steps is relatively easy. The widely used Herring-Mullins's theory [55] shows that a sinusoidal surface perturbation will decay as a sinusoid for an isotropic surface energy, i.e. $\gamma = \text{constant}$. This is shown schematically in Figure 1.12a. If the surface energy is orientation dependent ($\gamma = \gamma(\theta)$), as shown in Figure

1.12b, then the surface stiffness, $\beta = \gamma(\theta) + \frac{\partial^2 \gamma}{\partial^2 \theta}$, replaces the surface energy as the driving force². Below the roughening transition temperature, the surface energy is singular in the vicinity of a high symmetry orientation (see Figure 1.12c). This makes it difficult to be treated correctly by a continuum model. Step flow models have been developed to describe the surface dynamics below T_R in terms of discrete microscopic objects [55][56]. The surface chemical potential is discrete and facets are a natural result of the model description. It overcomes the singular problem of surface energy in continuum models. These are discussed later in Chapter 5.

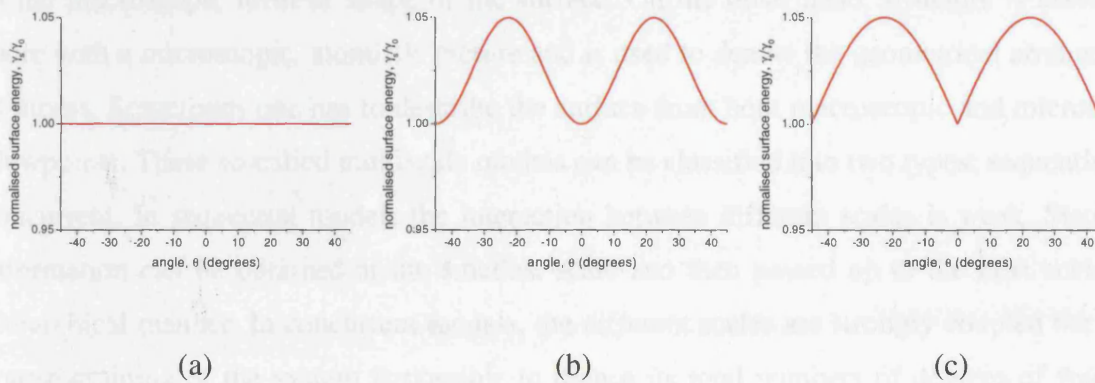


Figure 1.12 : Three common macroscopic surface energy descriptions (a) isotropic surface energy, (b) smooth orientation dependent surface energy and (c) cusped surface energy. The

first two are appropriate above the roughening transition temperature, where thermal excitations are sufficient for the surface not to get strongly trapped in a particular orientation, although (b) describes a weak orientational preference. Case (c) is applicable below the roughening temperature where thermal energy is less dominant and the surface has a strong driving force for facet formation at particular angles, e.g. for the case shown 0° and $\pm 45^\circ$.

² For a constant surface energy, the surface energy and surface stiffness are the same.

The relaxation of strained surfaces provides further challenges. The strain-induced morphological instability was first studied by Asaro and Tiller[33] and then further developed by Grinfeld [1] and Srolovitz [2] independently. It is known as the ATG instability. The linear ATG instability analysis for isotropic surface energy concludes that the initially flat surface of an elastically stressed body is unstable with respect to the growth of perturbations with wavelengths greater than a critical wavelength. A cusped surface energy can stabilise a film to perturbations of a critical size if it is orientated at a facet angle [39]. Nonlinear analysis allows the film evolution to be followed through large morphological changes, leading to the formation of cusp-like valleys with singular stress concentration near the cusp tip [4]. Such high stress concentrations act as potential sites for the nucleation of dislocations to relax the overall strain of an elastically stressed body. Latterly, 3D numerical methods for handling large amplitude surface fluctuation have also been developed [38] [39].

1.2.3 Multiscale surface models

In surface science, morphology is associated with a macroscopic property of solids and refers to the macroscopic form or shape of the surface. On the other hand, structure is associated more with a microscopic, atomistic picture and is used to denote the geometrical arrangement of atoms. Sometimes one has to describe the surface from both macroscopic and microscopic viewpoints. These so-called multiscale models can be classified into two types: sequential and concurrent. In sequential models the interaction between different scales is weak. Statistical information can be obtained at the smallest scale and then passed up to the next scale in a hierarchical manner. In concurrent models, the different scales are strongly coupled but some coarse-graining of the system is possible to reduce its total numbers of degrees of freedom. Elastic interactions provide a strong coupling between scales and hence this thesis concentrates on concurrent modelling techniques.

(a) Step flow models

As we have seen in section 1.1, a vicinal or rough surface typically consists of multiple terraces and steps. The analysis of individual surface steps is therefore essential to understand the interaction of steps with other steps, adatoms and vacancies. As discussed earlier, this is particularly important below the roughening transition temperature. Apart from entropy, the elastic field of a step is the dominant mechanism required for understanding interactions of adatoms, steps, and phase boundaries [21][22]. To model stress-induced crystal growth, one must first obtain a suitable description of the step-induced elastic field. Marchenko and

Parshin [19] first brought the notion of dipoles into linear elastic theory to model surface defects such as steps from classical electromagnetic theory. Rickman and Srolovitz [20] and Steward et al. [21] used methods based upon the same idea to model the elastic field as a multipole expansion of a mechanically equivalent force distribution on a half-plane. Kukta and Bhattacharya [22] obtained the second order solution for a single step and two steps which is an important modification as steps approach each other. The general conclusion is that the far field stress of an isolated surface step is well approximated by the force dipoles model in 2D half plane [19][20] although the strength of the dipoles depends on the atomistic detail of the step. A combined continuum/atomistic method for calculating the correct dipole strength is developed in Chapter 3.

Latterly, a continuum description of surface evolution based on the discrete features of the system has been paid more attention [8]. Such ‘step flow’ models describe the evolution on a strained or unstrained surface by following the motion of individual surface steps [8]. In these models the different kinetics of adatom diffusion across the terraces and attachment/detachment of atoms to/from steps can be incorporated. Variational principles based on step flow have even been developed to study the dynamics of nanoscale surface modulations below the roughening temperature [57]. These are simple multiscale models in the sense that they incorporate an atomistic length scale, the step height.

(b) The quasicontinuum method

This is a zero-temperature (Lattice Statics) method for crystalline solids in which the fine-grained atomistic region is replaced by a coarse-grained finite element representation where the macroscopic behaviour is predictable [13][14][58]. This reduces the total number of degrees-of-freedom in the system and allows large problems to be solved in a reasonable time. Interatomic potentials are used to inform the continuum regions about the constitutive response of the crystal to ensure consistency between the atomistic and continuum regions. The configuration that minimizes the total potential energy (sum over atomistic and continuum contributions) is then computed.

The quasicontinuum method has been developed [59]-[61] and successfully applied to the field of solid mechanics [62]-[64] to model the behaviour of defects such as dislocations, crack tips, grain boundaries and analyze nanoindentation experiments. It has also been applied to biological molecules in order to study the interactions of proteins and DNA [65]. There have recently been attempts to extend this method to finite temperature [90]. The principle difficulty encountered when going to finite temperature is phonon reflection at the fine-

grained/coarse-grained interface causing localised heating. Special matching conditions are required to avoid this [66][67].

Other similar approaches can also be found in the literature, in which a consistent hand shaking is implemented between the two regions [12][16]. Kohlhoff et al [12] constructed an overlap region between the atomistic core and the FE continuum and used non-local elasticity theory to describe this zone. Broughton et al [16] described the system in terms of a Hamiltonian, which was developed into a dynamic finite temperature parallel algorithm. This had three regions: a first-principles (DFT) quantum mechanics region embedded in a classical atomistic region embedded in a linear elastic finite element region.

(c) Coarse-Grained Molecular Dynamics (CGMD)

The equations of motion in CGMD are derived directly from finite temperature MD through a statistical coarse graining procedure [15]. They keep consistent with traditional MD as the mesh size is reduced to the atomic scale. This model is valid for dynamic perturbations to multiscale systems with defect-free crystalline lattices, such as the resonant behaviour of Nano-Electro-Mechanical Systems (NEMS).

(d) Accelerated Molecular Dynamics

MD is limited to very small time scales well below the time scales of diffusive events. In recent years, many approaches have been developed to overcome the limitations of MD by trying to accelerate it to model infrequent events such as surface diffusion. There are a number of accelerated molecular dynamics algorithms such as (modified potential) hyperdynamics, parallel replica dynamics and temperature accelerated dynamics [68]. However, these methods cannot yet reach macroscopic time scales and are still restricted to the nanometer length scale.

2.0 AN ATOMISTIC SURFACE MODEL

One goal of solid mechanics is to understanding the connection between the structure of a material and its properties. In this section, we wish to relate the continuum properties of a material to the properties of the underlying atomic lattice. This is vital for the development of consistent multiscale models in which the continuum region has the same linear elastic response as the atomistic region.

We look at two types of atomic interactions to calculate the total energy of the system: the Lennard- Jones (LJ) potential, and the LJ potential with an additional bond order (BO) term. Firstly we look at the bulk properties of Young's modulus (E) and Poisson's ratio (ν) using the LJ model and a "closed box" configuration. Then we investigate the surface properties of surface energy (γ) and surface stress (f) using an "open box" configuration. The analysis is then repeated for the LJ with BO model. Finally the LJ model with BO is employed to simulate the elastic relaxation of a circular atomic cluster.

2.1 Interatomic potentials

2.1.1 Lennard-Jones (LJ) potential

The LJ potential is a simple pairwise interaction potential, such that it is only a function of the distance between the nuclei of two atoms, r .

$$E = 4\omega_0 \left[\left(\frac{\sigma}{r} \right)^{12} - \left(\frac{\sigma}{r} \right)^6 \right] \quad (2-1a)$$

where the material parameter ω_0 defines the bond strength and σ defines the preferred interatomic separation. The LJ potential is illustrated in Figure 2.1. In the absence of other atomic interactions, the equilibrium atomic separation, $r_0 = 2^{1/6} \sigma = 1.12\sigma$, occurs at the energy minima, $E = -\omega_0$. The LJ potential generates a stable 2D structure with a regular triangular lattice. Equation (2-1a) is often rewritten as

$$E = \omega_0 \left[\left(\frac{r_0}{r} \right)^{12} - 2 \left(\frac{r_0}{r} \right)^6 \right]. \quad (2-1b)$$

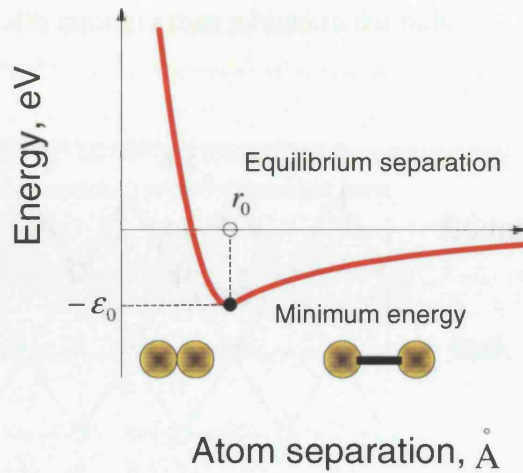


Figure 2.1 : Interatomic potential.

2.1.2 Lennard-Jones with bond-order (LJ+BO) potential

The LJ potential describes the interaction between bulk atoms, i.e. where every atom has a full coordination of 6 nearest-neighbour atoms. It does not account for the change in the strength of bonds between atoms of reduced coordination, such as at interfaces etc. As shown in Figure 2.2, atoms at a flat surface have a coordination number of 4. Bonds between these surface atoms are generally stronger than those between bulk atoms due to the enhanced electron density (due to unsaturated bonds). At the atomic scale, surface properties play a significant role and cannot be ignored. Consequently, a bond-order term [9] is introduced to incorporate a coordination number dependence on the bond strength. The LJ+BO potential is written as

$$E = \omega_0 \left[\left(\frac{r_0}{r_j} \right)^{12} - (b_{j1} + b_{j2}) \left(\frac{r_0}{r_j} \right)^6 \right], \quad (2-2)$$

where b_{j1} and b_{j2} are the half-bond strengths of the two connecting atoms which produces the bond j between them. Tersoff [9] gives their expression as follows

$$b_{ji} = D \left(1 + \beta^n Z_i^n \right)^{-\frac{1}{2n}} \quad (2-3)$$

where the parameters are $n = 10$, $\beta = \frac{1}{4}$, Z_i is the coordination number of atom i and D is a constant. To be comparable with the LJ potential we find that $D = 1.2258$ when $Z_i = 6$, i.e.

$b_{ji} = 1$. The bond strength for atoms with 4 nearest neighbours is therefore 1.184, i.e. this type of surface bond is 18.4% stronger than a bond in the bulk.

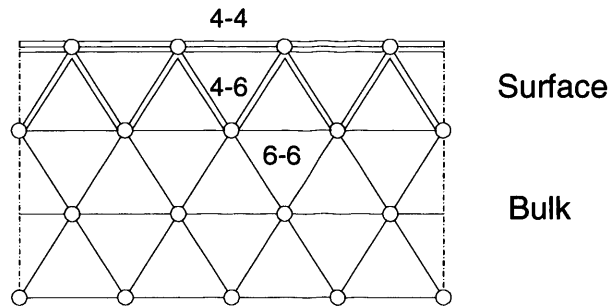


Figure 2.2 : Various bond strengths and coordination numbers for surface and bulk atoms.

2.2 Bulk properties (“closed box”) for LJ potential

In this section, the bulk properties of Young’s modulus and Poisson ratio are determined for the LJ atomistic potential. As there is always full coordination in the bulk, the BO term plays no role in these calculations.

2.2.1 The fundamental cell

The stable lattice structure is triangular (see Figure 2.3). We impose symmetrical boundary conditions on all sides of our “closed box” periodic unit cell. We will determine the elastic properties of the box by applying elastic strains, ϵ_{pq} , and determining the change in potential energy of the system. The indices $p, q = 1, 2$ relate to the two principal coordinate directions. From Figure 2.3 we can see that there are only 3 types of bonds ($j=1, 2, 3$) as shown in Figure 2.4.

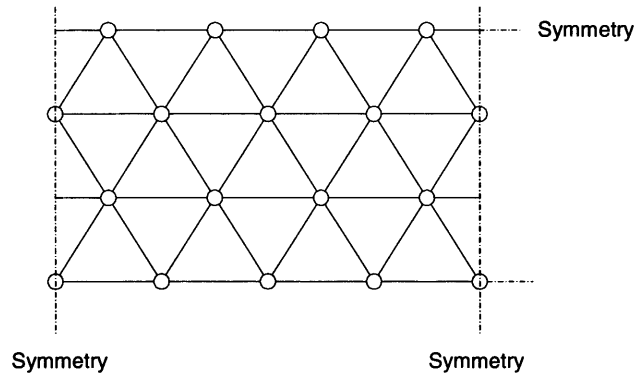


Figure 2.3 : “Closed box” unit cell.

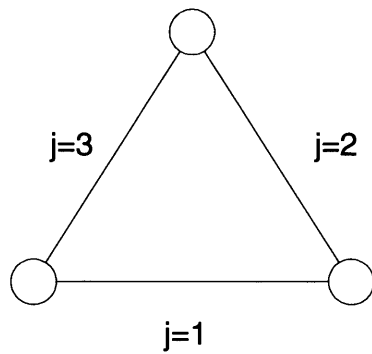


Figure 2.4 : Type of bonds.

We choose the smallest unit cell which can represent the whole lattice. This fundamental cell is shown in Figure 2.5. Its undeformed length is r_0 and width is $\frac{\sqrt{3}}{2} r_0$. We assume the thickness of each cell is r_0 such that the volume of a cell $V_0 = \frac{\sqrt{3}}{2} r_0^3$. In a bulk cell the number of bonds of the 3 types are $1 (= \frac{1}{2} + \frac{1}{4} + \frac{1}{4})$, 1, 1 respectively.

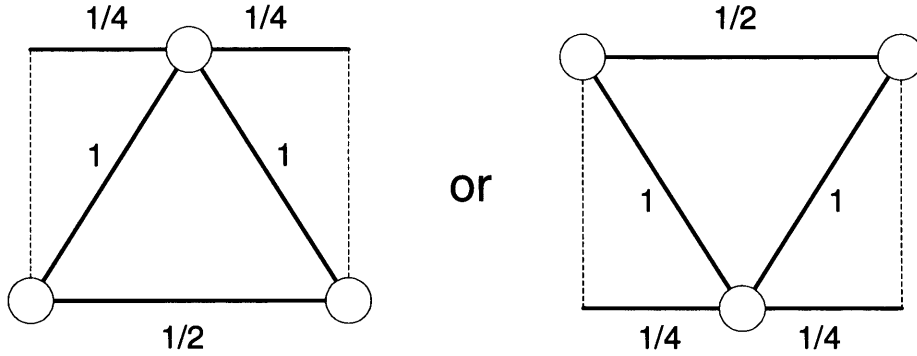


Figure 2.5 : Fundamental cell with distribution of bonds.

2.2.2 Analytical solutions of Young's modulus and Poisson's ratio

From the above fundamental cell, it is easy to calculate the total potential energy by summing over all of the bonds weighted contribution. In terms of the LJ potential, the energy per cell can be formulated as

$$\omega_b = \omega_0 \sum_{j=1}^3 \beta_j \left[\left(\frac{r_0}{r_j} \right)^{12} - 2 \left(\frac{r_0}{r_j} \right)^6 \right], \quad (2-4)$$

where ω_0 is the unit of energy (eV or J), r_0 is original atoms spacing (\AA or m), r_j is the length of bond j , and $\beta_1 = \beta_2 = \beta_3 = 1$ are the number of bonds of each type $j=1,2,3$ in a cell. It is convenient to use dimensionless parameters so we choose the unit of length to be r_0 , and the unit of energy to be ω_0 . Hence $r_j = \bar{r}_j r_0$, where \bar{r}_j is the dimensionless interatomic separation, and $\omega_b = \bar{\omega}_b \omega_0$, where $\bar{\omega}_b$ is the dimensionless bond energy.

When the fundamental cell is deformed elastically, the energy per cell can be written in terms of the strains as

$$\bar{\omega}_b = \sum_{j=1}^3 \beta_j \left[\frac{1}{(1 + \rho_j)^6} - \frac{2}{(1 + \rho_j)^3} \right], \quad (2-5)$$

where

$$\begin{aligned}\rho_1 &= 2\varepsilon_{11} + \varepsilon_{11}^2 + \varepsilon_{12}^2 \\ \rho_2 &= \frac{1}{2}\varepsilon_{11} + \frac{1}{4}\varepsilon_{11}^2 + \frac{3}{2}\varepsilon_{22} + \frac{3}{4}\varepsilon_{22}^2 + \varepsilon_{12}^2 + \frac{\sqrt{3}}{2}\varepsilon_{12}(2 + \varepsilon_{11} + \varepsilon_{22}). \\ \rho_3 &= \frac{1}{2}\varepsilon_{11} + \frac{1}{4}\varepsilon_{11}^2 + \frac{3}{2}\varepsilon_{22} + \frac{3}{4}\varepsilon_{22}^2 + \varepsilon_{12}^2 - \frac{\sqrt{3}}{2}\varepsilon_{12}(2 + \varepsilon_{11} + \varepsilon_{22})\end{aligned}$$

The normal strains, ε_{11} and ε_{22} , are in the x-direction and y-direction respectively, and γ_{12} is the shear strain. A detailed derivation of this transformation is given in Appendix A.

For small strains, the second order binomial expansion of equation (2-5) gives a quadratic approximation for the (dimensionless) energy per unit cell

$$\bar{\omega}_b = \sum_{j=1}^3 \beta_j (\rho_j^2 - 1) \quad (2-6)$$

or

$$\bar{\omega}_b = \frac{81}{2}\varepsilon_{11}^2 + \frac{81}{2}\varepsilon_{22}^2 + 54\gamma_{12}^2 + 27\varepsilon_{11}\varepsilon_{22} - 3. \quad (2-7)$$

The (dimensionless) bulk stresses at a point can be related to the bulk strains by

$$\bar{\sigma}_{ij} = \bar{c}_{ijkl} \varepsilon_{kl}, \quad (2-8)$$

where $\bar{\sigma}_{ij} = \sigma_{ij} V_0 / \omega_0$ are the dimensionless stresses and $\bar{c}_{ijkl} = c_{ijkl} V_0 / \omega_0$ are the dimensionless elastic constants. The (dimensionless) strain energy density and the elastic constants are therefore

$$\bar{\Omega}_b = \frac{1}{2} \bar{\sigma}_{ij} \varepsilon_{ij} = \frac{1}{2} \varepsilon_{ij} \bar{c}_{ijkl} \varepsilon_{kl}, \quad \bar{c}_{ijkl} = \frac{\partial \bar{\omega}_b}{\partial \varepsilon_{ij} \partial \varepsilon_{kl}}. \quad (2-9)$$

So the elastic constants, \bar{C} in this case, are obtained from (2-6), (2-7) and (2-9) as follows

$$\bar{C} = 81 \begin{bmatrix} 1 & \frac{1}{3} & 0 \\ \frac{1}{3} & 1 & 0 \\ 0 & 0 & \frac{1}{3} \end{bmatrix}.$$

Comparing this expression with the material stiffness matrix for an isotropic, linear elastic continuum under plane stress conditions

$$\bar{C} = \frac{E}{1-\nu^2} \begin{bmatrix} 1 & \nu & 0 \\ \nu & 1 & 0 \\ 0 & 0 & \frac{1}{2}(1-\nu) \end{bmatrix}$$

demonstrates that the LJ potential produces a linear elastic continuum consistent with a Poisson ratio of $\nu = \frac{1}{3}$ and a Youngs' modulus of $\bar{E} = 72$ or $E = 72\omega_0 / V_0$.

2.2.3 Non-linear excursions of the bulk strain energy density

We take a “closed box” as shown in Figure 2.3 with 20 atoms per row and 10 rows. A normal strain is applied in the x -direction. The atoms on the boundary are constrained such that they can only move tangential to the boundary.

The total sample energy for a range of normal strains (-6% to +6%) is shown in Figure 2.6 along with the analytical solution of (2-6). The analytical solution is symmetric about $\varepsilon_{11}=0$ as expected. This predicts that the material deforms the same under compression or tension which is reasonable for small strains less than 1%. The numerical results show that the material deforms less readily under compression at strains less than 1%, a regime which is pertinent to heteroepitaxial systems (where compressive mismatch strains can reach 5-10%).

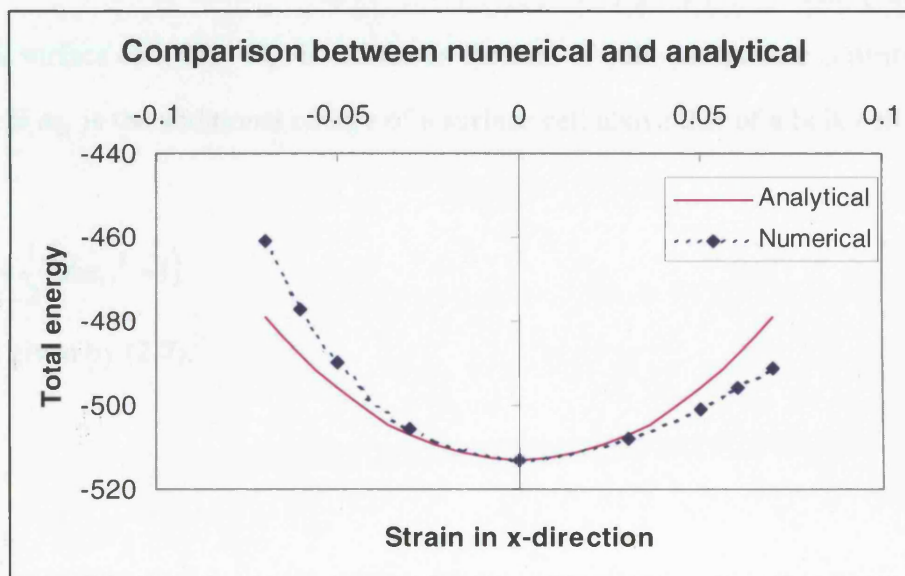


Figure 2.6 : Comparison between numerical and analytical results for bulk total strain energy as a function of normal strain.

2.3 Surface properties (“open box”) for LJ potential

In the next two sections we derive two surface properties, the surface energy (γ) and the surface stress (f), from the two interatomic potential models, LJ and LJ+BO.

2.3.1 Surface energy and surface stress

(a) Surface energy

Surface energy is due to the presence of unsaturated bonds at a free surface. These bonds have a higher energy than saturated bonds (in the bulk) and this increase in energy is represented by the continuum property of surface energy (energy per unit area of surface). We take as our reference state the situation where an infinite bulk material is cut in half between two layers and two surfaces are produced as shown in Figure 2.7. We consider an atomic sample with M atoms per row and N rows cleaved along the mid-horizontal plane. Figure 2.8 shows the consequent surface cell. The sample consists of $(M - 1)(N - 1)$ unit cells. Consider half the sample of size $N_x \times N_y$, where $M = N_x$ and $N = 2N_y$. The volume of the half sample is therefore $\bar{V}_b = (N_x - 1)(N_y - \frac{1}{2})$.

In the surface cell, the bonds are such that $\beta_1 = \frac{3}{2}$ and $\beta_2 = \beta_3 = 1$. The (dimensionless) energy per surface cell, $\bar{\omega}_s + \bar{\omega}_b$, is written as the sum of bulk and surface contributions, such that $\omega_s = \bar{\omega}_s \omega_0$ is the additional energy of a surface cell above that of a bulk cell. From (2-5) we have

$$\bar{\omega}_s = \frac{1}{2}(36\epsilon_{11}^2 - 1) \quad (2-10)$$

and $\bar{\omega}_b$ is given by (2-7).

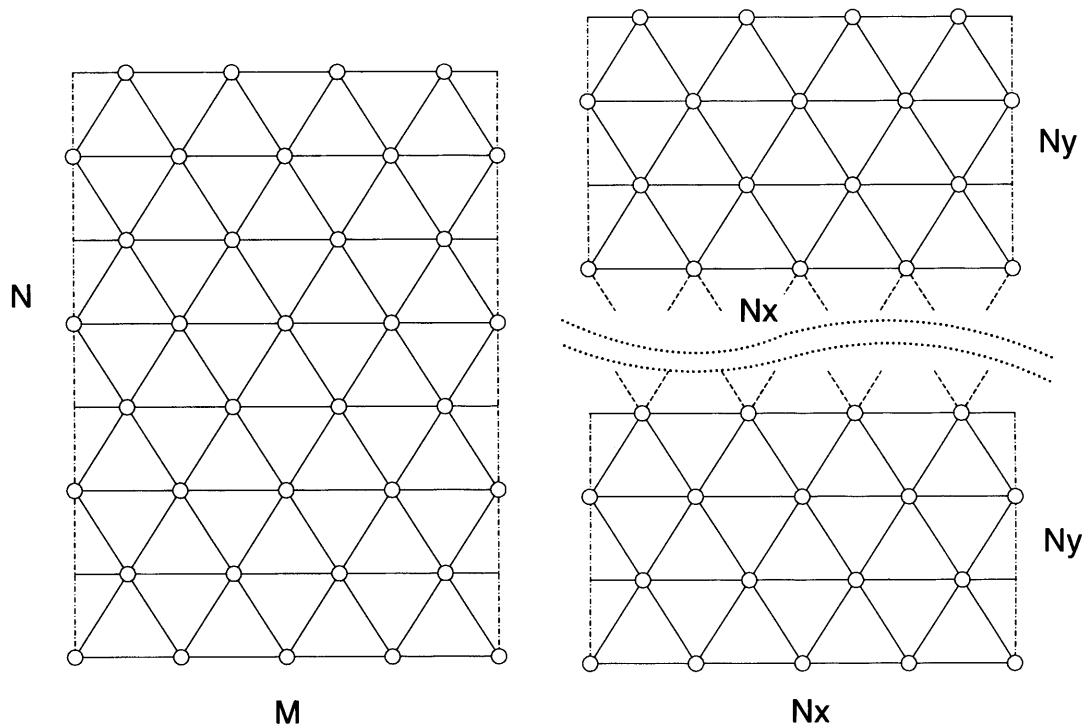


Figure 2.7 : The surface energy is calculated by dividing a bulk sample in half. The surface energy is the increase in energy.

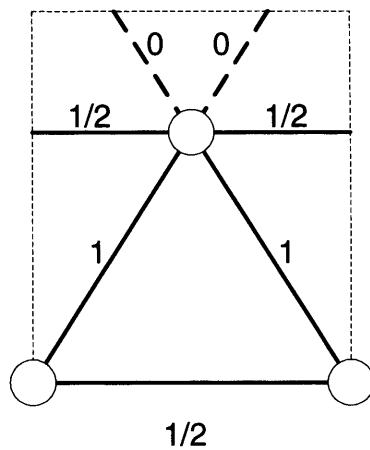


Figure 2.8 : The fundamental surface cell. Saturated bonds are solid lines. Unsaturated bonds are shown as dashed lines.

There are $(N_x - 1)$ surface cells in the half sample so the total energy per half sample is the sum of bulk (b) and surface (s) contributions

$$\begin{aligned}\bar{E} &= \bar{E}_b + \bar{E}_s \\ &= \bar{\omega}_b (N_x - 1)(N_y - \frac{1}{2}) + \bar{\omega}_s (N_x - 1).\end{aligned}\quad (2-11)$$

We write the surface contribution as

$$\bar{E}_s = \bar{\gamma}_s \bar{A}_s = \bar{\gamma}_s (N_x - 1),$$

where $\gamma_s = \bar{\gamma}_s \omega_0 / r_0^2$ is surface energy density, $A_s = \bar{A}_s r_0^2$ is the surface area. As $\bar{E}_s = \bar{E} - \bar{E}_b$ we can write

$$\bar{\gamma}_s = \left(\bar{\omega}_s - \frac{1}{2} \bar{\omega}_b \right).\quad (2-12)$$

Equations (2-7) and (2-10) then give

$$\bar{\gamma}_s = 1 - \frac{9}{4} \epsilon_{11}^2 - \frac{81}{4} \epsilon_{22}^2 - 27 \gamma_{12}^2 - \frac{27}{2} \epsilon_{11} \epsilon_{22}.\quad (2-13)$$

At a free surface, the stresses normal to the surface are zero so $\sigma_{22} = \sigma_{12} = 0$. For a surface cell

$$\bar{\sigma}_{ij} = \frac{\partial(\bar{\omega}_b + \bar{\omega}_s)}{\partial \epsilon_{ij}}$$

which yields $\epsilon_{22} = -\nu \epsilon_{11}$ and $\gamma_{12} = 0$ with $\nu = \frac{1}{3}$, consistent with linear elastic theory.

The consequence of this is that (2-13) simply yields $\bar{\gamma}_s = 1$ for the L-J potential model, i.e. it is independent of surface strain. The significance of this is investigated in the next subsection.

(b) Surface stress

Surface stress is related to surface energy. It arises due to the fact that atoms relaxed in a surface plane have a different natural lattice spacing than those relaxed in the bulk. This is because they have a different coordination number. For the bulk and surface to be commensurate the surface atoms must be strained (or stressed) to adopt the bulk lattice spacing. This is illustrated in Figure 2.9.

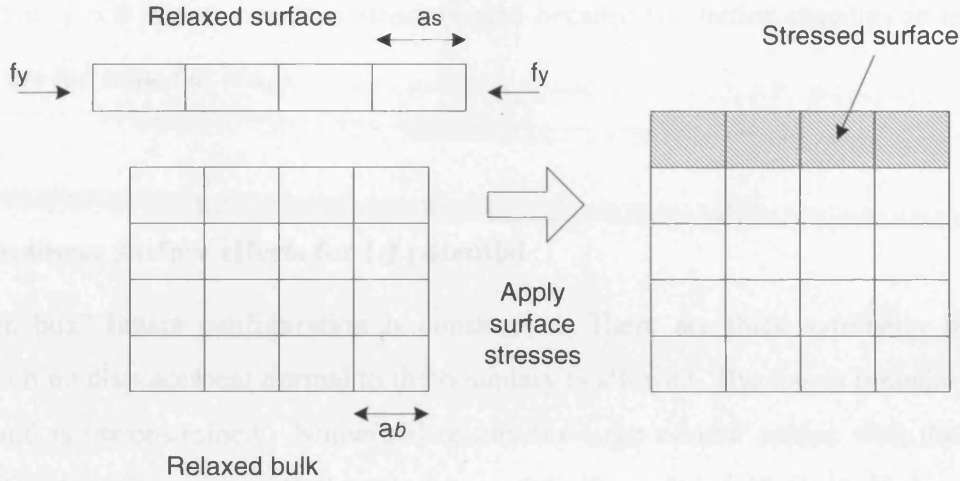


Figure 2.9 : For the bulk and surface to be commensurate the surface atoms must be strained (or stressed) to adopt the bulk lattice spacing.

If the surface atomic spacing, a_s , is greater than the bulk atomic spacing, a_b , then the surface stress is negative (compressive). Similarly, if $a_s < a_b$, the surface stress is positive (tensile). The stress in the surface monolayer is given by

$$\bar{\sigma}_{11}^s = \frac{\partial(\bar{\omega}_b + \bar{\omega}_s)}{\partial \epsilon_{11}}, \quad (2-14)$$

subject to the following conditions for a traction free surface,

$$\bar{\sigma}_{22}^s = \frac{\partial(\bar{\omega}_b + \bar{\omega}_s)}{\partial \epsilon_{22}} = 0 \quad \text{and} \quad \bar{\tau}_{12}^s = \frac{\partial(\bar{\omega}_b + \bar{\omega}_s)}{\partial \gamma_{12}} = 0.$$

However, the surface stress, f , is the component of the stress in the surface due to the surface properties only. It does not include the bulk stress due to an applied strain. Hence, using (2-12),

$$\bar{f} = \bar{\sigma}_{11}^s - \frac{3}{2} \bar{\sigma}_{11} = \frac{\partial \bar{\gamma}_s}{\partial \epsilon_{11}}. \quad (2-15)$$

This is the usual definition for surface stress in a solid. The factor of $\frac{3}{2}$ arises because a surface cell has a 50% higher stiffness than a bulk cell. This is because the surface horizontal bond is not shared with an adjacent cell (i.e. it counts as one bond not half a bond). Consequently the stress is 50% higher for a given strain. For the LJ potential, equation (2-13)

implies that $f = 0$, i.e. the surface stress is zero because the lattice spacings in the surface and bulk are the same ($a_s = a_b$).

2.3.2 Non-linear surface effects for LJ potential

An “open box” lattice configuration is constructed. There are three symmetry boundaries upon which no displacement normal to the boundary is allowed. The fourth boundary is a free surface and is unconstrained. Numerical results for large normal strains with the full non-linear LJ potential are compared with the analytical result of (2-6) in Figure 2.10. As expected, the analytical results show no dependence on the sign of the strain. The surface energy contribution is not a function of strain in this case, so the open box configuration is similar to that for the closed box, the only difference being the addition of a (constant) excess surface energy in the open box configuration.

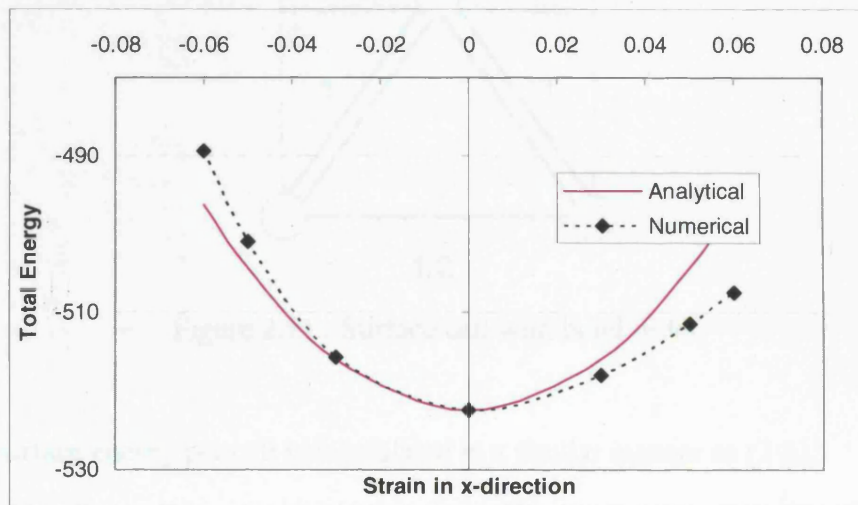


Figure 2.10 : Comparison between numerical and analytical solutions for the total potential energy of a LJ lattice with a free surface.

2.4 Surface properties for LJ+BO interatomic potential

In this section, the properties of surface energy and surface stress are derived for the LJ+BO potential. The method is identical to that followed in the previous section.

2.4.1 Analytical solution

Figure 2.11 illustrates the bonding in a surface cell with bond order. A bond represented by 3 lines is stronger than one with 2 lines etc. A bond represented by 1 line is equivalent to a normal L-J bond. From (2-5) we can therefore write the surface energy per cell for the LJ+BO potential as

$$\begin{aligned}\tilde{\omega}_s &= \sum_{j=1}^4 \beta_j \left[\left(\frac{1}{\bar{r}_j} \right)^{12} - (b_{j1} + b_{j2}) \left(\frac{1}{\bar{r}_j} \right)^6 \right] \\ &= \sum_{j=1}^4 \beta_j \left[\frac{1}{(1 + \rho_j)^6} - \frac{b_{j1} + b_{j2}}{(1 + \rho_j)^3} \right]\end{aligned}\quad (2-16)$$

where $\beta_1 = 1/2$ with $b_{11} + b_{12} = 2$, $\beta_2 = \beta_3 = 1$ with $b_{21} + b_{22} = b_{31} + b_{32} = 2.184$, and $\beta_4 = 1$ with $b_{41} + b_{42} = 2.368$.

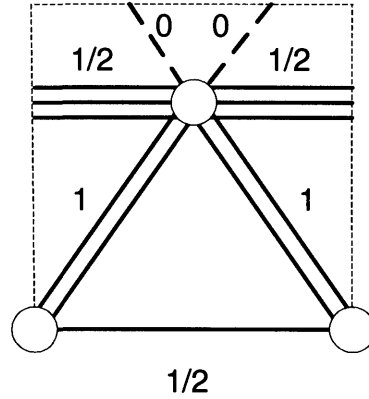


Figure 2.11 : Surface cell with bond order.

The excess surface energy per cell is formulated in a similar manner as (2-6),

$$\begin{aligned}\bar{\omega}_s &= \sum_{j=1}^4 \beta_j \left[(1 - b_{j1} - b_{j2}) - (6 - 3b_{j1} - 3b_{j2})\rho_j + (21 - 6b_{j1} - 6b_{j2})\rho_j^2 \right] - \bar{\omega}_b \\ &= 10.00\varepsilon_{11}^2 - 4.14\varepsilon_{22}^2 - 4.42\gamma_{12}^2 - 3.31\varepsilon_{11}\varepsilon_{22} + 2.76\varepsilon_{11} + 1.66\varepsilon_{22} - 1.24,\end{aligned}\quad (2-17)$$

where $\bar{\omega}_b$ is given by (2-7). At the free surface we again have $\bar{\sigma}_{22}^s = \bar{\tau}_{12}^s = 0$. This implies that $\gamma_{12} = 0$ and from

$$\bar{\sigma}_{22}^s = \frac{\partial(\bar{\omega}_b + \bar{\omega}_s)}{\partial \varepsilon_{22}} = 72.7\varepsilon_{22} + 23.7\varepsilon_{11} + 1.66 = 0$$

we have

$$\epsilon_{22}^s = -0.0228 - 0.326\epsilon_{11}.$$

This implies that there is a small contraction in the thickness of the surface monolayer even in the absence of applied strain. This is because of the increased strength of the surface bonds normal to the surface. Equation (2-12) still applies so the surface energy density can be expressed as

$$\bar{\gamma}_s = -7.4\epsilon_{11}^2 + 2.2\epsilon_{11} + 0.21. \quad (2-18)$$

This expression for the surface energy for the LJ+BO potential is compared with the expression derived from the LJ potential in Figure 2.12. It is clear that the surface energy for the LJ+BO potential is significantly less than that for the LJ potential (for a flat surface). The LJ+BO surface energy is zero at a strain of -7.6%. This occurs because the excess energy of the LJ+BO surface cells increases less rapidly with compressive strain than the energy of the bulk cells.

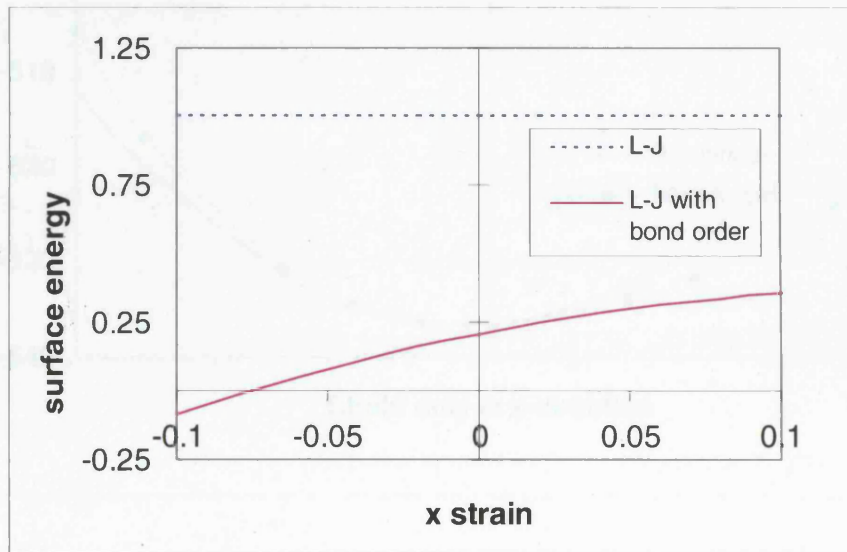


Figure 2.12 : Surface energy per unit cell for the LJ and LJ+BO potentials.

Using (2-15), equation (2-18) implies that the surface stress is

$$\bar{f} = 2.2 - 14.8\epsilon_{11}. \quad (2-19)$$

From (2-15), the actual stress in the surface is $\bar{\sigma}_{11}^s = \frac{1}{2}\bar{\sigma}_{11} - \bar{f} = 93.3\epsilon_{11} + 2.2$. This is zero when $\epsilon_{11} = -0.026$ which means that the equilibrium lattice spacing on the surface is

$0.974 r_0$. The strain dependence is usually ignored in which case the approximate surface stress would be $\bar{f} \approx 2.2$.

2.4.2 Non-linear surface effects for the LJ+BO potential

A comparison between the analytical expression for the total energy of the “open box” sample derived in the previous sub-section and a numerical solution is shown in Figure 2.13. Both predict that the total energy is minimised at a non-zero (negative) strain. This is because the number of surface cells (19) is not negligible compared to the number of bulk cells (19×9.5), i.e. it is roughly 10% surface. The non-linear effects are consequently significant above 1% strain and below -3% strain. The non-linear softening in tension and stiffening in compression is similar to the previous results.

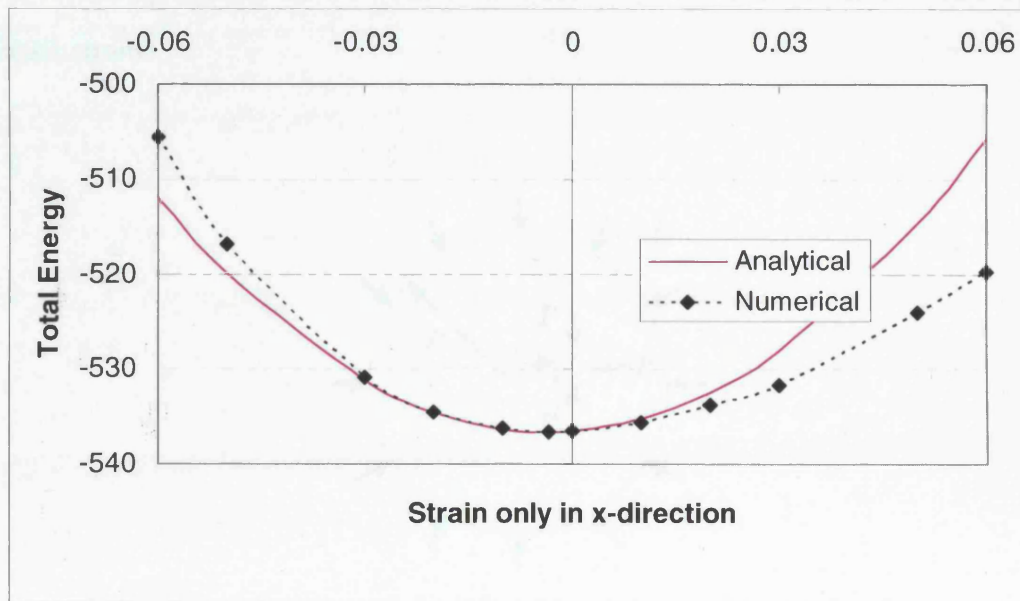


Figure 2.13 : Total potential energy of the “open box” sample for the LJ+BO potential as a function of extensional strain.

2.5 Relaxation of a circular atomic cluster

In the previous section, the properties of a flat, unstepped surface have been investigated and analytical expressions have been derived. In this section, the more complicated morphology of a curved surface will be investigated, in which surface steps are expected to play a role.

The stress state induced by surface effects in a small circular atomic cluster is analysed from this perspective.

2.5.1 Analytical solution

A circular disk is investigated under plane stress conditions. The total energy of the disk is the sum of the bulk, E_b and surface, E_s , contributions. A homogeneous surface is expected to exert a uniform hydrostatic pressure, $-P$, on the bulk as shown in Figure 2.14. The strain energy in the bulk (assuming linear elasticity) can then be expressed as

$$\begin{aligned} E_b &= \frac{1}{2}(\sigma_r \epsilon_r + \sigma_\theta \epsilon_\theta) \cdot \pi R^2 \\ &= \frac{(1-\nu)}{E} P^2 \pi R^2 = \frac{E}{(1-\nu)} \epsilon_0^2 \pi R^2, \end{aligned} \quad (2-20)$$

where E is Young's modulus, ν is Poisson's ratio, R is the radius of the disk and ϵ_0 is the hydrostatic strain.

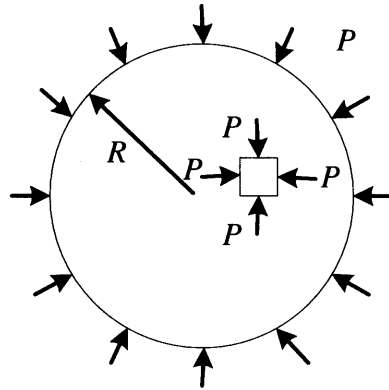


Figure 2.14 : The surface is assumed to exert a uniform pressure on the bulk.

The total surface energy is the integral of the surface energy density over the total surface area

$$E_s = \int_0^{2\pi} \gamma_s(\epsilon_s, \theta) R d\theta, \quad (2-21)$$

where $\gamma_s(\epsilon_s, \theta)$ is the surface energy which is assumed to be a function of the surface strain, ϵ_s , and the surface orientation, θ . The surface strain is the hoop strain at the surface

which is equivalent to the hydrostatic strain in the bulk, i.e. $\varepsilon_s = \varepsilon_0$. As a first approximation, we ignore the orientational dependence of the surface energy (due to surface steps) and minimize the total energy to determine the value of the hydrostatic strain. We have therefore

$$\frac{\partial(E_b + E_s)}{\partial\varepsilon_0} = 2\frac{E}{(1-\nu)}\varepsilon_0\pi R^2 + \frac{\partial\gamma_s}{\partial\varepsilon_0}2\pi R = 0,$$

which, given the definition of surface stress from (2-15), leads to

$$\varepsilon_0 = -\frac{(1-\nu)}{E} \frac{f_0}{\left(R + \frac{(1-\nu)\Delta f}{E}\right)} \quad \text{or} \quad PR = \frac{f_0}{\left(1 + \frac{(1-\nu)\Delta f}{ER}\right)}. \quad (2-22)$$

where we have assumed the surface stress is a linear function of strain, $f = f_0 + \Delta f\varepsilon_0$, in accordance with (2-19). For the LJ potential, we found that $f_0 = 0$ so the hydrostatic pressure is zero. This is not surprising as the surface bonds have the same equilibrium length as the bulk bonds so the surface is commensurate with the bulk in the absence of strain. For the LJ+BO potential we expect from (2-19) that $f_0 = 2.2$ and $\frac{(1-\nu)}{E}\Delta f = -0.14$ in dimensionless form (for a flat surface). An interesting observation about the predicted stress/strain state in the cluster is that a length scale, $l = -\frac{(1-\nu)}{E}\Delta f = 0.14r_0$, has been introduced simply by consideration of continuum quantities. The relative size of the surface monolayer volume has not been included. This predicts that the effective hydrostatic force on the cluster, $f = PR$, is not a constant as normally assumed, but will depend on the cluster size. These analytical flat surface predictions for curved surface behaviour are compared with numerical curved surface calculations in the next sub-section.

2.5.2 Numerical method

An atomic approximation to a circular disk is made by keeping all the atoms in a regular triangular lattice with centres within a radius R of the central coordinate, as shown in Figure 2.15. Each atom is assigned a variable horizontal and vertical position, except for the central atom (which is fixed in both directions) and one off-centre atom (which is fixed so that it can only move in a radial direction) to prevent rigid body translation or rotation of the disk.

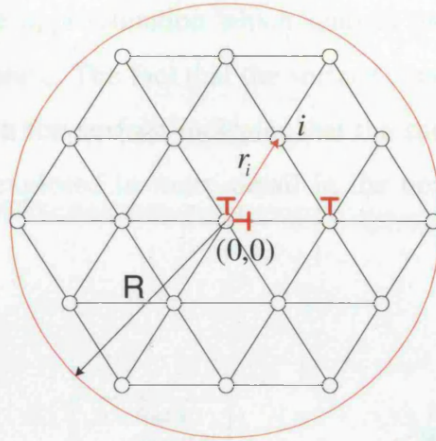


Figure 2.15 : Numerical construction of the circular atomic cluster.

The total energy of the disk can then be formulated in terms of the variable atomic positions from the sum of all the interatomic potentials. This non-linear function can then be minimised using a conjugate gradient solver to find the atomic positions for the lowest energy configuration. Dimensionless units are used throughout. The LJ+BO potential is used (as no displacements are induced for the LJ potential).

A simulation result for a disk of radius $\bar{R} = 43.3$ is shown in Figure 2.16. The radial displacements of all the atoms, u , are plotted as a function of their radial distance from the centre of the disk, r . For a hydrostatic strain field we know that $u = r\epsilon_0$, so, from subsection 2.5.1, we expect the slope of the curve to be constant and equal to ϵ_0 . This is approximately true in Figure 2.16. The scatter in the data is due to the surface steps (or orientational dependence of the surface energy) which we have neglected in the analytical model.

Simulations for a range of disk radii were performed and the results are shown in Figure 2.17 with the predictions of continuum theory (2-22). One can immediately see that the size effect predicted in (2-22) is only significant for very small disks ($R < 10$) but that the trend it predicts does concur with that seen in the numerical simulations. There is a significant difference which is not too surprising as a homogenised continuum theory is not expected to be very representative at these small scales. The PR value for the smallest disk ($R=4$) is largest. This is because this small cluster is hexagonal (see Figure 2.15 as an example) and the corner atoms have a low coordination number of three so their three bonds are very strong and induce a strong contraction in the surface. As the size of the clusters increases, the PR value gradually asymptotes towards a constant value, as expected. This is below the value of 2.2 predicted by the analytical result, but again, this is not entirely surprising as this was

developed from a flat surface approximation which ignores the effect of surface steps, step interactions and surface curvature. The fact that the surface contraction for the curved surface is less than that expected for a flat surface indicates that the surface steps lower the effective surface stress. This will be explored in more detail in the next chapter in which atomistic surface steps are considered.

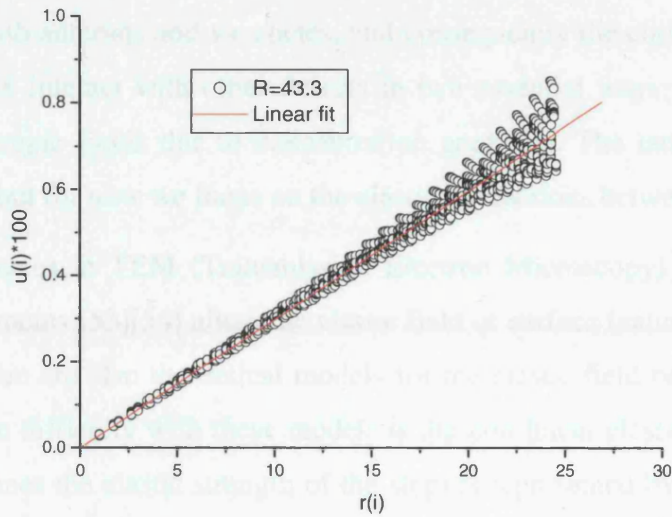


Figure 2.16 : Radial atomic displacements in a circular disk of radius 43.3 as a function of radial distance from the centre for the LJ+BO potential.

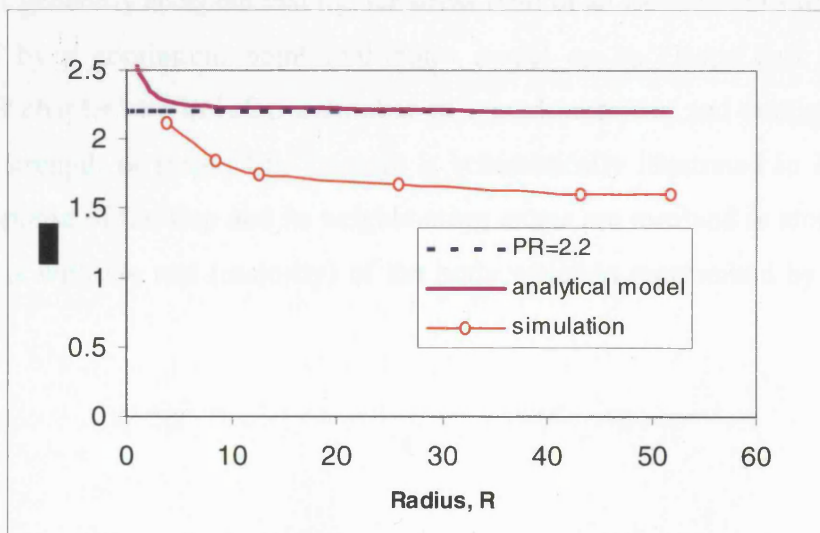


Figure 2.17 : Comparison of PR as a function of cluster radius from analytic model, (2-22), and numerical simulation.

3.0 ANALYSIS OF A SURFACE STEP

The surface of an epitaxial thin film typically consists of multiple terraces and steps. The analysis of an isolated surface step is important to understand the interaction of steps with other steps, steps with adatoms and vacancies, and consequently the entire growth process of thin films. Steps can interact with other defects in two essential ways: via their long-range elastic fields or entropic fields due to concentration gradients. The latter will be discussed again in Chapter 4, but for now we focus on the elastic interactions between steps.

Recent advances in TEM (Transmission Electron Microscopy) and FIM (Field Ion Microscope) experiments [53][54] allow the elastic field of surface features to be investigated experimentally. There are also theoretical models for the elastic field based on linear elastic theory [21][22]. The difficulty with these models is the non-linear elastic region surrounding the step (which defines the elastic strength of the step) is represented by constants which are not related to the atomistic interatomic potential. It is the aim of this section to relate the strength of the step elastic field to the interatomic potentials. This could be achieved using an atomistic model of the type used in last chapter. In practise this is difficult due to the large number of atoms required due to their long range elastic interactions with the (remote) boundary. It is generally accepted that the far stress field of an isolated 2D surface step is well approximated by a continuum point multipoles model on an elastic half plane [19][20]. Hence, in this chapter, we develop a number of mixed atomistic and continuum models to calculate the strength of steps. This concept is schematically illustrated in Figure 3.1. The non-linear response of the step and its neighbouring atoms are resolved in atomic detail. This region interacts with the rest (majority) of the body which is represented by a linear elastic model.

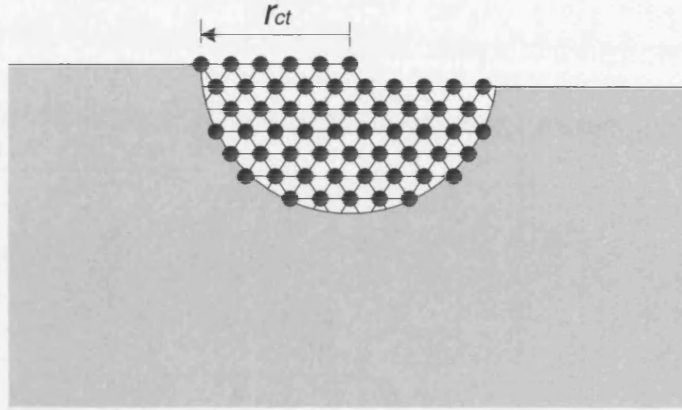


Figure 3.1 : An isolated surface step. The region around the step ($r < r_{ct}$) is resolved in atomistic detail and interacts with the rest of the body which is represented by continuum linear elasticity.

3.1 Continuum force dipole model

This section introduces the continuum point multipole theory which will be used to represent the elastic far field of the surface step outside of the atomistic region (i.e. for $r > r_{ct}$, where r_{ct} is a critical radius, see Figure 3.1). In the theory of elasticity, an arbitrary force distribution on an elastic half-space can be exactly described by a distribution of elastic multipoles.

$$F_{mi} = \int_{-\infty}^{\infty} f_i(x) x^m dx \quad (3-1)$$

where F_{0i} is the point force (monopole) in the i th direction, F_{1i} is the point dipole, F_{2i} is the quadrupole (and in general F_{mi} is the 2^m dipole), $i=x$ or z , and $f_x(x)$ and $f_z(x)$ are the components of the distribution of step-induced force. In the absence of epitaxial surface strains there is no net surface force so F_0 is zero. In general only the lowest order multipoles are important in determining the far-field of a surface step [21]. Hence we only consider the contribution of force dipoles $d_x = F_{1x}$ and $d_z = F_{1z}$, shown in Figure 3.2, where

$$d_x = \int_L f_x(x) x dx \quad \text{and} \quad d_z = \int_L f_z(x) x dx. \quad (3-2)$$

The z -dipole is commonly approximated as $d_z = \gamma_s a$, where γ_s is the (constant) surface energy density and $a \approx r_0$ is the step height. The resulting stress field, expressed in polar coordinates [73], is

$$\sigma_r = \frac{2d_x \cos 2\theta + 2d_z \sin 2\theta}{\pi r^2}, \quad (3-3)$$

$$\sigma_\theta = 0, \quad (3-4)$$

$$\tau_{r\theta} = \frac{d_x \sin 2\theta - 2d_z \cos^2 \theta}{\pi r^2}. \quad (3-5)$$

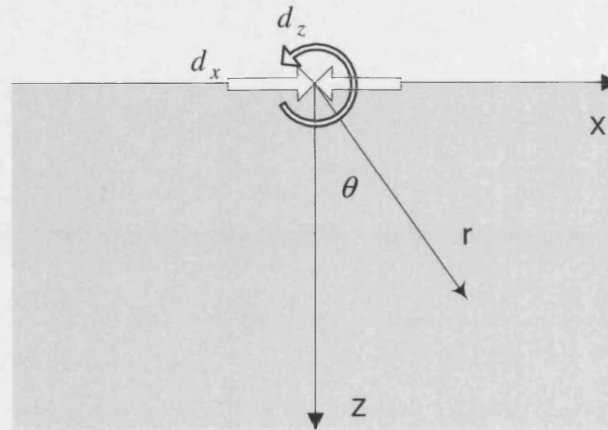


Figure 3.2 : An long range elastic field of an isolated step is approximately represented by point dipoles d_x and d_z .

3.2 A mixed atomistic and continuum force dipole model

The purpose of this section is to obtain the numerical value of the two point dipole strengths, d_x and d_z , (given a step geometry and interatomic potential model) by coupling an atomistic model with and the continuum force dipole model of the previous section.

3.2.1 The Model

Lattice Statics (LS) calculations will be employed to determine the equilibrium deformed field within the atomistic region (see Figure 3.1). Outside of the atomistic region, the elastic deformation field will be approximated by the continuum point dipole model. The bridge between the atomistic and continuum models are the displacements on the interface between the two regions. The displacements on the boundary of the LS simulation will be defined by

the displacements predicted by the force dipole field, i.e. the displacements of the boundary atoms, $u_i^b(d_x, d_z)$, are only functions of the point dipole strengths, d_x and d_z . The total potential energy of body can therefore be written as

$$\begin{aligned} E_{tot} &= E_a(u_{xi}, u_{zi}, u_{xi}^b, u_{zi}^b) + E_c(d_x, d_z) \\ &= E_a(u_{xi}, u_{zi}, d_x, d_z) + E_c(d_x, d_z) \end{aligned} \quad (3-6)$$

where suffices a and c denote the atomistic and continuum regions respectively, u_{xi} and u_{zi} are the x and z displacements of the i th atom, and u_{xi}^b and u_{zi}^b are the displacements of boundary atoms. The formulation of the boundary displacements is presented in Appendix B. In the following, $E_a(u_{xi}, u_{zi}, d_x, d_z)$ and $E_c(d_x, d_z)$ will be simply written as E_a and E_c respectively.

In the atomistic region, the total potential energy is based upon the LJ+BO potential (see Chapter 2) and can be written as

$$E_a = \sum_i \sum_{j>i} \omega_0 \left[\left(\frac{r_0}{r_{ij}} \right)^{12} - (b_i + b_j) \left(\frac{r_0}{r_{ij}} \right)^6 \right], \quad (3-7)$$

where the summation is over all atoms i and r_{ij} is the distance between atoms i and j .

In the continuum region, one can write

$$E_c = E_{c0} + \Delta E_c \quad (3-8)$$

where E_{c0} is the (constant) potential energy of the undeformed body (which plays no role in determining the deformed field) and ΔE_c is the change in the potential energy of the continuum region due to the deformation. For a linear elastic body we know that

$$\Delta E_c = \frac{1}{2} \int_{\Omega} \sigma_{ij} \epsilon_{ij} dV,$$

where Ω is the volume of the region. For plane stress conditions and polar coordinates this is

$$\Delta E_c = \frac{1}{2} \int_{-\frac{\pi}{2}}^{\frac{\pi}{2}} \int_{-R}^{\infty} (\sigma_r \epsilon_r + \sigma_{\theta} \epsilon_{\theta} + 2\tau_{r\theta} \epsilon_{r\theta}) r dr d\theta. \quad (3-9)$$

Using (3-3) to (3-5) with the normal constitutive equations for linear elasticity yields

$$\Delta E_c = \frac{1}{4E\pi R^2} \left[(3 + \nu) d_x^2 + (5 + 3\nu) d_z^2 \right], \quad (3-10)$$

where E and ν are material Young's modulus and Poisson ratio respectively, R is the cut-off radius. A minimum energy solution for $(u_{xi}, u_{zi}, d_x, d_z)$ can now be obtained numerically using an appropriate numerical solver. However, for consistency with the atomic model, the continuum model must take into account the interaction between the step and the surface stress field. This is addressed in the following subsection.

3.2.2 Surface stress in the continuum dipole model

As mentioned by Kukta and Bhattacharya [22], Shilkrot and Srolovitz [74], and Srolovitz and Hirth [75], the stress field around a step on an unstrained surface arises due to a discontinuity in the surface stress. We have already seen in Chapter 2 that the LJ potential will not induce a stress field in a surface as it is a zero surface stress potential. Hence the LJ+BO potential is employed. A surface stress will be induced in the surface monolayer of the atomistic region. An equivalent surface stress must therefore also be added into the continuum region for consistency.

We assume that a stress component σ_s exists in a layer of thickness b on the surface, as depicted in Figure 3.3. The surface stress field can therefore be written as

$$\sigma_x = \begin{cases} \sigma_s & \text{for } 0 \leq z \leq b \\ 0 & \text{for } z > b \end{cases}, \quad (3-11)$$

$$\sigma_z = 0. \quad (3-12)$$

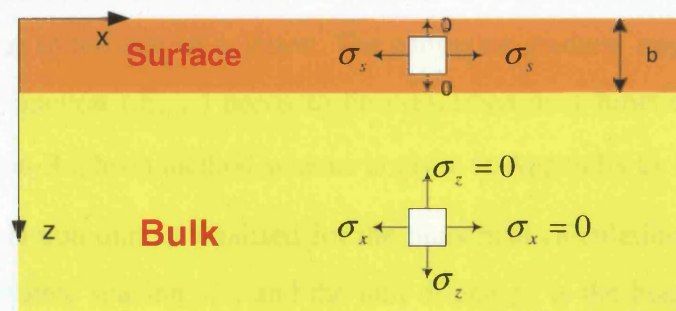


Figure 3.3 : Continuum surface stress model induces a stress into an atomic scale surface layer of thickness, b .

Assuming $b \ll R$, superposition yields the combined surface stress state due to the dipole stresses (for $\theta = \pm\pi/2$) and surface stress

$$\sigma_x = -\frac{2d_x}{\pi x^2} + \sigma_s, \quad (3-13)$$

$$\sigma_z = \tau_{xz} = 0 \quad (3-14)$$

for $z < b$. The change in energy of the continuum region due to this surface layer is

$$\Delta E_c^s = 2 \int_R^\infty \frac{b}{2E} \left(-\frac{2d_x}{\pi x^2} + \sigma_s \right)^2 dx - 2 \int_R^\infty \frac{b}{2E} \left(-\frac{2d_x}{\pi x^2} \right)^2 dx. \quad (3-15)$$

With (3-10), the total elastic energy in the continuum region is therefore

$$\Delta E_c = \frac{1}{4E\pi R^2} \left[(3+\nu)d_x^2 + (5+3\nu)d_z^2 \right] - \frac{4d_x b \sigma_s}{\pi E R} + \frac{b \sigma_s^2 (\infty - R)}{E}, \quad (3-16)$$

where the last term is an infinite constant (due to an infinite surface) which can be neglected in the minimization process. This expression replaces (3-10) in the total energy formulation, where we have $f = b\sigma_s$ from (2-15).

3.2.3 Numerical results for mixed atomistic-dipole model

Two numerical methods are used to get an accurate solution to the energy minimisation problem defined by (3-6), (3-7) and (3-16). The fully non-linear conjugate gradient method is used to obtain a crude first approximation to the minimum energy configuration. This initial guess is then utilised in a Newton-Raphson method to solve a succession of global linear problems to converge to the correct solution. The conjugate gradient implementation is trivial as only the object function (E_{TOT}) needs to be prescribed as a function of the degrees-of-freedom. The Newton-Raphson method scheme is given in Appendix G.

The system is non-dimensionalised for the numerical calculations. The unit of length is the equilibrium atomic spacing r_0 , and the unit of energy is the bond strength, ω_0 . Other

non-dimensional parameters are therefore $\bar{E} = \frac{E r_0^3}{\omega_0} = 72$ and $\nu = \frac{1}{3}$ (from Chapter 2),

$$\bar{d}_x = \frac{d_x r_0}{\omega_0} \text{ etc.}$$

The results for the calculation of \bar{d}_x and \bar{d}_z are shown in Figure 3.4. The results are consistent with the force dipole continuum approximation, in the sense that the values converge to a reasonably constant value as the size of the atomistic simulation increases in radius. If the force dipole model was wrong one would expect to see a distinct size effect. It is interesting to see that the linear elastic dipole approximation is valid for an atomistic simulation with radius $\bar{R} > 3$. This demonstrates that the non-linearity at the core of the surface step is very localised. The average dipole values are $\bar{d}_x = 3.93$ and $\bar{d}_z = 2.14$. The x -dipole is larger than the z -dipole (by a factor of roughly two) which is consistent with other theoretical and experimental findings [21]. The slight variability in the dipole values coincides with the geometrical disparity between the discrete atomistic and semi-circular continuum step regions.

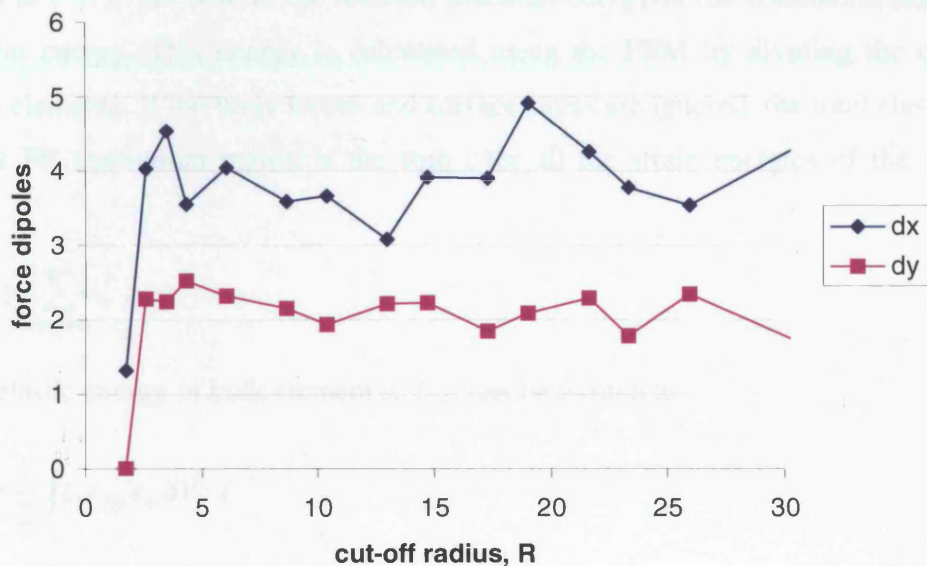


Figure 3.4 : Calculated force dipoles, \bar{d}_x and \bar{d}_z , for an isolated surface step for different size atomistic simulations, \bar{R} .

3.3 Combined atomistic and finite element models

In the previous section, the far-field of an isolated surface step was demonstrated to be adequately represented by point force dipole approximation. This technique is effective for steps on an infinite elastic half-plane. One of the deficiencies in this model was the lack of precise geometric compatibility between the discrete atomistic region and the semi-circular continuum region. In addition, the elastic half-space was of a uniform height, whereas the

height should differ by the step height on either side of the step. It is of general interest to resolve these issues and to see if this method can be extended to a more general technique where the form of the far-field is not known apriori. For instance, for more complex defect structures or steps interacting in more constrained (non-infinite) geometries. In this subsection, we will employ the Finite Element Method (FEM) to represent the linear elastic far-field.

3.3.1 Using the Finite Element Method (FEM) in the continuum region

A general linear elastic far-field from a defect can be accurately represented by the FEM if the elastic strains are small. The problem is similar to before, in the sense that the total potential energy needs to be formulated and the lowest energy configuration found in terms of the positional degrees-of-freedom. The potential energy of the atomistic region has already been determined in (3-7). As before, the relevant potential energy in the continuum region is the elastic strain energy. This energy is calculated using the FEM by dividing the continuum region into elements. If the body forces and surface stress are ignored, the total elastic energy in the bulk FE continuum region is the sum over all the strain energies of the individual elements

$$U_{FE}^b = \sum_{elements} U_e^b, \quad (3-17)$$

where the elastic energy of bulk element e , U_e^b , can be written as

$$U_e^b = \frac{1}{2} \int_{V_e} \epsilon_{ij} c_{ijkl} \epsilon_{kl} dV, \quad (3-18)$$

where ϵ_{ij} and c_{ijkl} are the strain and material stiffness tensors respectively, V_e is the elemental volume (or area in 2D). The elemental energies are assembled into the global elastic energy so as to obtain the total elastic energy. A detailed derivation of the elemental elastic strain energy is presented in Appendix C, but the general form is quite standard and can be written as

$$U_e^b = \frac{1}{2} [u^e]^T [k^e] [u^e], \quad (3-19)$$

where $[k^e]$ is the elemental stiffness matrix, and $[u^e]$ is a matrix containing the (unknown) displacement degrees-of-freedom of the elements nodes.

Triangular elements are used with six nodes and an unstructured triangular mesh was generated using a free 2D Delaunay triangulation routine called ‘Triangle’ [78]. A typical triangular mesh is shown in Figure 3.5. Near the atomistic region, the size of the elements is constrained to the atomic scale to retain high resolution in that highly strained area and to be compatible with the atomistic region. The FE nodes at the atomistic/continuum interface are chosen to coincide with the positions of atoms on this boundary. Far from the atomistic region, the sizes of the elements can be enlarged to decrease the total number of degrees of freedom and minimize the computational cost.

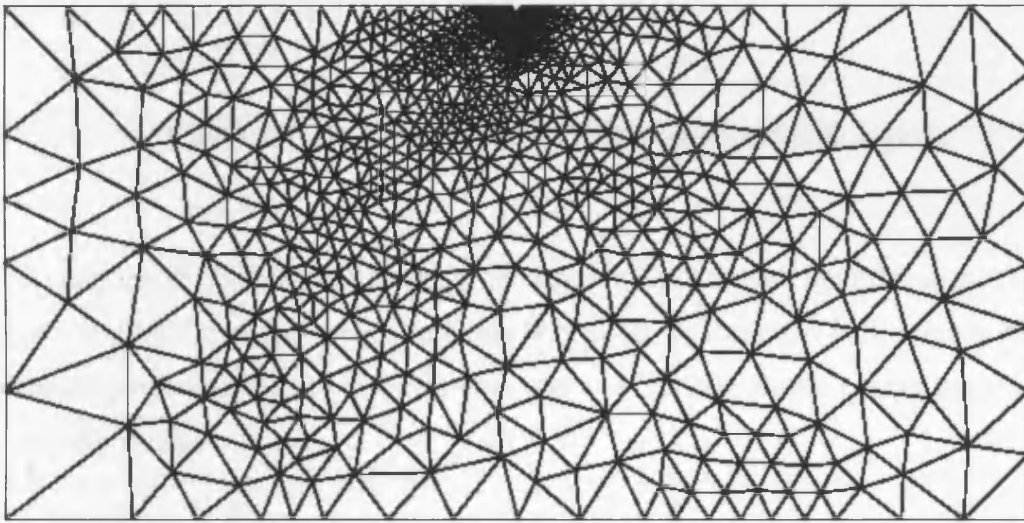


Figure 3.5 : Triangular FE mesh of continuum region. The small atomistic region is omitted but occupies the top-centre semi-circular region.

3.3.2 Surface transformation strain

When atomistic and continuum models are coupled together, it is important for the continuum model to be consistent with the atomistic model. As we have already seen in section 3.1, one consequence of this is that the surface stress generated by the LJ+BO potential in the atomistic region must also be represented in the continuum region. This is achieved by introducing a surface transformation strain, ϵ^T , into the surface monolayer of the FE model. As seen in Chapter 2, this is a mismatch strain

$$\epsilon^T = \frac{a_s - a_b}{a_b}, \quad (3-20)$$

due to a different equilibrium lattice spacing for the surface, a_s , and bulk, a_b , atoms. This strain is negative for the LJ+BO potential (see Chapter 2).

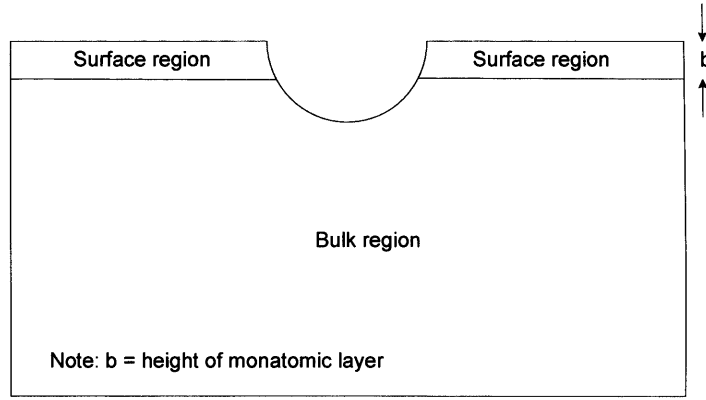


Figure 3.6 : FE region is divided into surface and bulk regions.

To take this difference between bulk and surface into account, the FE region is divided into surface and bulk regions. We assume that both of the surface and bulk regions have the same material properties and are coherent with one another. The elastic energy in the surface region can be written as

$$U_{FE}^s = \sum_{\text{surface element}} U_e^s, \quad (3-21)$$

where the elastic energy of surface elements is given by

$$\begin{aligned} U_{FE}^s &= \frac{1}{2} \int_{V_e} (\epsilon_{ij} - \epsilon_{ij}^T) c_{ijkl} (\epsilon_{kl} - \epsilon_{kl}^T) dV \\ &= \frac{1}{2} [u^e]^T [k^e] [u^e] - [u^e]^T [R^e] + U_0 \end{aligned}$$

where $\epsilon_{ij}^T (= [\mathcal{E}^T])$ is the surface transformation strain tensor (matrix), $[k^e]$ is the same as before, $[R^e] = \int_{V_e} [\mathcal{E}^T]^T [C^e] [B^e] dV$ is the elemental force matrix, and U_0 is a constant. The

surface transformation strain can be written as

$$[\mathcal{E}^T] = \begin{bmatrix} \epsilon_x^T \\ \epsilon_y^T \\ \gamma_{xy}^T \end{bmatrix} = \begin{bmatrix} \epsilon^s \\ 0 \\ 0 \end{bmatrix},$$

where ε^s is the desired surface strain.

One can assemble the whole elemental matrices in both surface and bulk regions to find the total elastic energy as

$$\begin{aligned} U_{FE} &= U_{FE}^b + U_{FE}^s \\ &= \frac{1}{2} [\mathbf{u}_{FE}]^T [\mathbf{K}_{FE}] [\mathbf{u}_{FE}] - [\mathbf{u}_{FE}]^T [\mathbf{R}_{FE}] + \text{constant}, \end{aligned} \quad (3-22)$$

where $[\mathbf{K}_{FE}]$, $[\mathbf{R}_{FE}]$ and $[\mathbf{u}_{FE}]$ are the global stiffness, force and nodal displacement matrices respectively. An iterative scheme for converging to a minimal global energy configuration is described in the next section.

3.3.3 Numerical implementation

The aim is to minimize the total combined coupled energy of the atomistic (3-7) and FE (3-22) regions

$$E_{tot} = E_a([\mathbf{u}_{LS}]) + \frac{1}{2} [\mathbf{u}_{FE}]^T [\mathbf{K}_{FE}] [\mathbf{u}_{FE}] - [\mathbf{u}_{FE}]^T [\mathbf{R}_{FE}], \quad (3-23)$$

where the atomistic potential energy, $E_a([\mathbf{u}_{LS}])$, is a non-linear function of the displacements in the atomistic (Lattice Statics) region, $[\mathbf{u}_{LS}] = [\mathbf{u}_a | \mathbf{u}_{ac}]$, which includes the atomistic/continuum boundary displacements $[\mathbf{u}_{ac}]$ as well as the other atomistic displacements $[\mathbf{u}_a]$. The continuum potential energy is a quadratic function of the nodal displacements in the FE region, $[\mathbf{u}_{FE}] = [\mathbf{u}_c | \mathbf{u}_{ac}]$, which includes the atomistic/continuum boundary displacements and the other continuum displacements, $[\mathbf{u}_c]$.

The numerical strategy is similar to the one used in the mixed atomistic-dipole model of section 3.2. An initial guess at the minimum energy configuration is obtained using a non-linear, conjugate gradient (CG) solver. A global, linear Newton-Raphson (NR) method is then used to converge to an optimal solution. The CG method is simple as only the above objective function needs to be prescribed.

For the NR method, the non-linear potential is expanded to second order about the current guess for the LS displacements, $[\mathbf{u}_{LS}^0]$, and written as a quadratic approximation, compatible with the FE functional form

$$\begin{aligned}
 E_a([u_{LS}]) &= E_a([u_{LS}^0]) + \left. \frac{\partial E_a}{\partial [u_{LS}]} \right|_{[u_{LS}] = [u_{LS}^0]} [u_{LS}] + \frac{1}{2} [u_{LS}]^T \frac{\partial^2 E_a}{\partial [u_{LS}] \partial [u_{LS}]} [u_{LS}] \\
 &= \frac{1}{2} [u_{LS}]^T [K_{LS}] [u_{LS}] - [u_{LS}]^T [R_{LS}] + \text{constant}
 \end{aligned} \tag{3-24}$$

The total energy of (3-23) can therefore be assembled into the form

$$E_{TOT} = \frac{1}{2} [u]^T [K] [u] - [u]^T [R] + \text{constant} . \tag{3-25}$$

where all the atomistic/nodal degrees-of-freedom are contained in $[u] = [u_{LS} \mid u_{FE}]$. An improved estimate at the lowest energy configuration can therefore be obtained from the minimum energy condition

$$[K][u] = [R], \tag{3-26}$$

and the process repeated until convergence is obtained.

3.3.4 Results and discussion

The radius of the atomistic region is 10 atomic spacings in the following non-dimensional calculation. The FE region is 100x50 spacings. Firstly, the inclusion of the surface transformation strain is tested to ensure that the atomistic and continuum regions are compatible in the absence of a step or any defects. The analysis of Chapter 2 predicts that $\epsilon^s \approx -0.026$. The horizontal displacement of a surface atom on the boundary between the atomistic and FE regions is plotted in Figure 3.7. If the atomistic and FE regions are consistent then the displacement should be zero by symmetry. The displacement reaches a zero value for ϵ^s between -0.026 and -0.03 . This is consistent with the above prediction and demonstrates that the surface transformation strain is effective in reproducing surface stress conditions compatible with those found in the atomistic simulation.

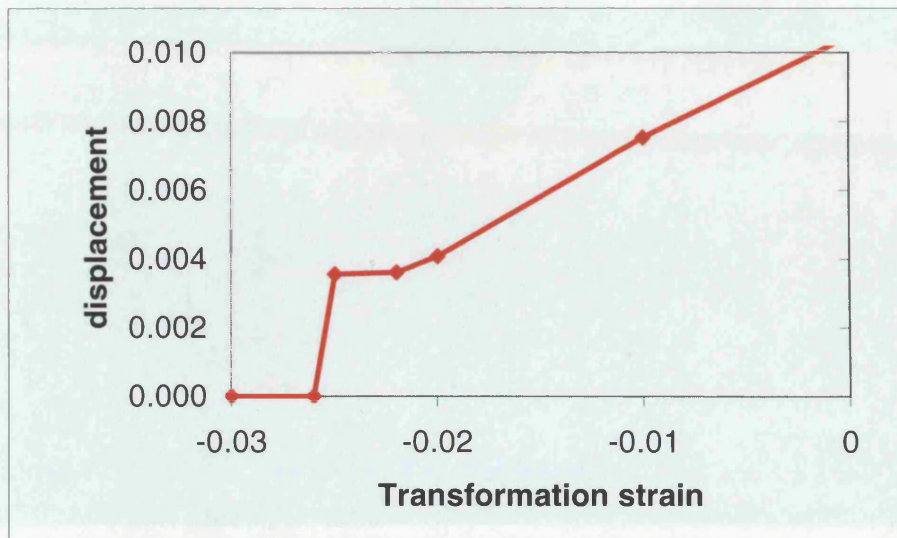


Figure 3.7 : In the absence of a step or any other defect, the horizontal displacement of a surface node on the atomistic/FE boundary should be zero when the surface transformation strain in the continuum region correctly balances the surface stress in the atomistic region.

This occurs at a strain of -2.6%.

The minimum energy configuration is now determined in the presence of an isolated surface step for the LJ+BO potential. The displacement field in the FE region calculated using the mixed LS and FE model is shown in Figure 3.8. The displacement components on the atomistic/continuum interface are shown in Figure 3.9 for both the atomistic/force dipole model of section 3.2 and the atomistic/FE model developed in this section. The results are very similar which reinforces the confidence in the predictions of both models. The nodes at both the lower and higher terrace surfaces move away from the step in x -direction as expected for a positive \bar{d}_x force dipole. In the y -direction, the nodes on the higher terrace surface move down and the nodes on the lower terrace surface move up, again consistent with a positive (anticlockwise) \bar{d}_z force dipole. This is consistent with the experimental observations [21].

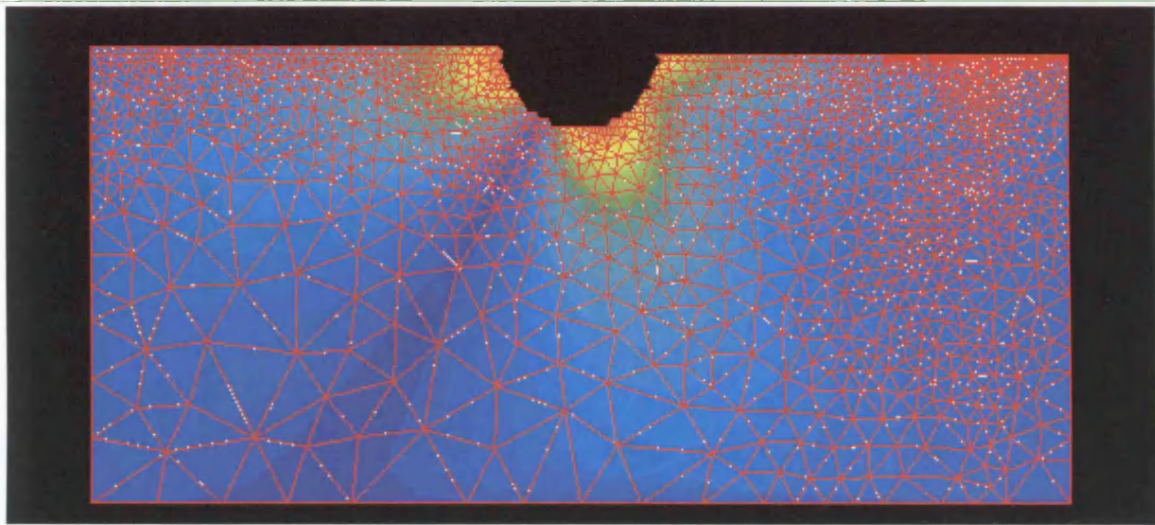


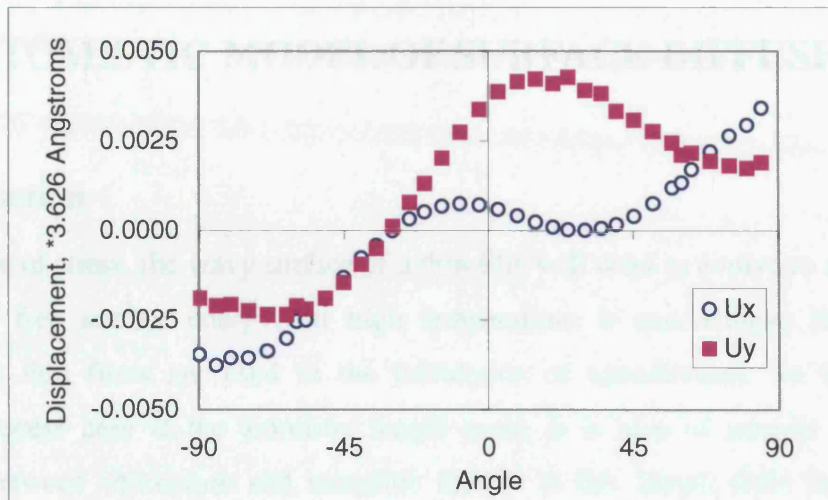
Figure 3.8 : Coloured contours show the displacement field in the FE continuum region with the FE mesh. The surface and bulk regions are easily seen.



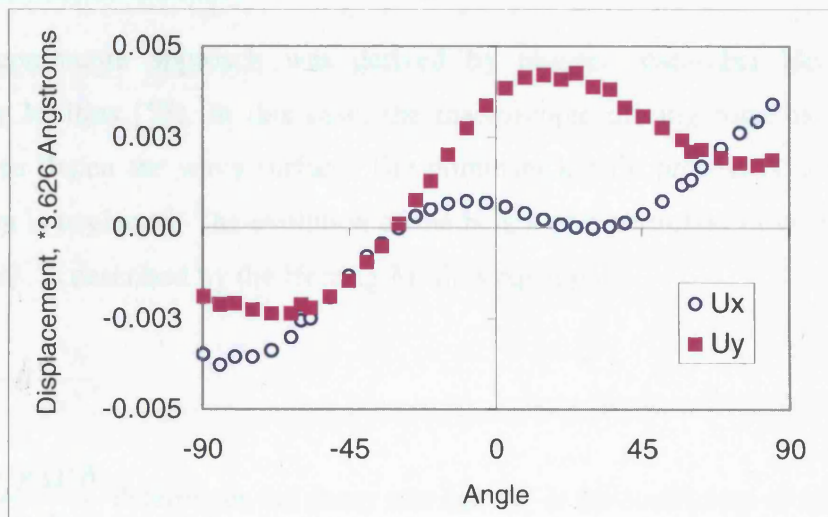
Figure 3.9 : Comparison of displacements of boundary nodes at the quarter-point of the surface step (a) using finite elements (section 3.2) and (b) FE continuum region.

3.5 Discussion

Just before [1] and the Finite Element Method (FEM) are coupled together to analyze the stress distribution field of an isotropic surface step. To complement the effect of the surface (a) the elastic region in the continuum FE region, a surface thin-film constraint is added into the surface layer in the continuum region to retain consistency with the bulk region. Numerical results demonstrate the validity of this approach.



(a)



(b)

Figure 3.9 : Displacement components of boundary nodes at the atomistic/continuum interface for (a) point dipole continuum (section 3.2) and (b) FE continuum (section 3.3).

3.3.5 Summary

Lattice Statics (LS) and the Finite Element Method (FEM) are coupled together to analyze the elastic displacement field of an isolated surface step. To complement the effect of the relaxation (in the atomistic region) on the continuum FE region, a surface transformation strain is added into the surface layer in the continuum region to retain consistency with the atomistic region. Numerical results demonstrate the validity of this approach.

4.0 AN ATOMISTIC MODEL OF SURFACE DIFFUSION

4.1 Introduction

In the absence of stress, the wavy surface of a thin film will want to evolve to a flat surface to minimize its free surface energy. At high temperatures it can achieve this via surface diffusion. As thin films are used in the fabrication of nanodevices, we investigate this relaxation process here at the atomistic length scale. It is also of interest to explore the correlation between continuum and atomistic models at this length scale (on the order of nanometres). Generally, there are two approaches to investigating the decay of a perturbed surface:

(a) Continuum models

The continuum approach was derived by pioneer researcher Herring and then developed by Mullins [55]. In this case, the macroscopic driving force is surface energy which tends to flatten the wavy surface. The dominant kinetic process is surface diffusion. Bulk diffusion is neglected. The evolution of the height of a perturbed (low curvature) 1+1D surface, $h(x,t)$, is described by the Herring-Mullins equation

$$\frac{\partial h}{\partial t} = -B \frac{\partial^4 h}{\partial x^4}, \quad (4-1)$$

where $B = \frac{D_s \gamma_s \Omega^2 \delta}{k_B T}$ determines the decay rate and D_s is the coefficient of surface diffusion, γ_s is the surface energy density, Ω is the atomic volume, δ is the density of adatoms on the surface, k_B is Boltzmann constant and T is absolute temperature. This equation predicts that the amplitude of a sinusoidal surface will decay as an exponential function of time as

$$A = A_0 \exp(-t/\tau), \quad (4-2)$$

where A_0 is the initial amplitude of the sinusoidal wave, $\tau = \frac{k_B T}{D_s \gamma_s \Omega^2 \delta} \left(\frac{\lambda}{2\pi} \right)^4$ is the characteristic decay time and λ is the wavelength of the sinusoid surface. Details are given in Appendix E. These equations are valid at macroscopic length scales above the roughening

temperature (see section 1.1.3). Below the roughening transition temperature, the process of surface diffusion is complicated because the individual surface steps can be the critical feature in determining the relaxation rate. In this case, the surface energy is highly anisotropic with facets forming at singular cusps. This regime is difficult to model using conventional continuum models. In recent years, step flow models have been developed to describe discrete microscopic kinetics of the surface [55]. We will investigate the application of these models to this problem over a range of temperatures in Chapter 5.0.

(b) Atomistic models

Another way to investigate surface relaxation is by resolving all the atoms individually (see section 1.2.1). Molecular Dynamics (MD) is a commonly used atomistic method but it is limited to very small time scales and cannot reach the time scales of diffusive events. Kinetic Monte Carlo (KMC) simulations are better in this regard as they have a flexible time scale which can be extended to cover the real process of thin film evolution. In the last few years, an off-lattice KMC model [71][72] has been developed which uses real interatomic potentials so that it can correctly represent the underlying physics of strain-induced film growth. This model will be used here and is explained more fully in the next section.

4.2 An off-lattice KMC model for surface diffusion

The KMC algorithm will initially be described in its normal context: the on-lattice KMC model. This will then be extended to the more powerful off-lattice KMC model in the subsequent subsection.

4.2.1 The on-lattice KMC model

The KMC algorithm is different from the standard Monte Carlo (MC) algorithm in that it relates simulation time to real time. The KMC algorithm therefore needs to know all the rates of all possible events in which an atom jumps from one site to another one before determining which event might happen. Harmonic Transition State Theory (HTST) [83] predicts that the rate of an event i can be written as

$$R_i = \nu_0 e^{-\frac{E_i}{k_B T}} \quad (4-3)$$

where ν_0 is the atomic vibration frequency for all atoms (typically $10^{10} s^{-1}$), E_i is the activation energy for the event (or energy barrier between two states, i.e. sites), k_B is

Boltzmann's constant and T is absolute temperature. All possible events are tabulated with their associated rates. Given the sum of all the rates, $R = \sum_{i=1}^N R_i$, the probability for an event i is R_i / R . An event i is chosen and performed according to a uniformly distributed random number between 0 and R . The time increment between the changes of configuration is given according to a Poisson distribution $P(\tau) = R e^{-R\tau}$ such that

$$\tau = -\frac{\ln \rho}{R}, \quad (4-4)$$

where ρ is a uniformly distributed random number between 0 and 1.

This process is now described for a simple solid-on-solid (SOS) model. The surface profile is defined by the height of each column of atoms, as shown in Figure 4.1. The columns are indexed by position, $h_1, \dots, h_{i-1}, h_i, h_{i+1}, \dots, h_n$. The activation energy of an event is defined by the number of lateral neighbours that an atom has, i.e. $E_i = nE_h$ where E_h is half the (negative) bond energy and n is the number of lateral neighbours. Because there is always a bond below the atom, only lateral bonds are important. For an adatom (atom with no lateral neighbours) $E_i = 0$, for an atom on a step edge (one lateral neighbour) $E_i = E_h$, and for an atom in the surface (two lateral neighbours) $E_i = 2E_h$. A wavy surface tends to reduce its surface energy. Hence surface atoms will stick to step edges and fill in holes (low energy sites) so as to flatten the surface. The SOS model is known as an on-lattice model as the atoms can only occupy pre-defined positions. On-lattice KMC models ignore the effect of elastic distortion due to defects (such as surface steps) on the activation energy. This is especially important in heteroepitaxially strained structures.

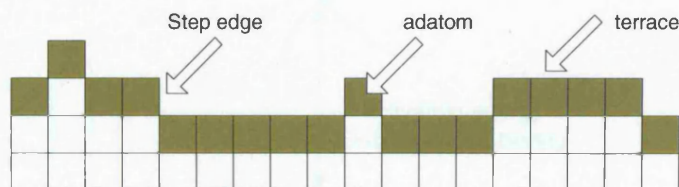


Figure 4.1 : SOS model of an atomic surface.

4.2.2 The off-lattice KMC model

Unlike the on-lattice KMC method, the off-lattice KMC method allows atoms to occupy any position in space as in a real atomic lattice. The interactions between atoms are defined by the interatomic potentials. Hence the elastic surface and kinetic properties of an off-lattice KMC model are completely defined by the interatomic potential. The Lennard-Jones (LJ) interatomic potential (with and without bond order) was introduced in Chapter 2.0 and was used to derive its associated elastic and surface properties. We utilize this potential again in this section to explore the corresponding surface kinetic properties associated with this potential. The equilibrium 2D lattice structure is therefore triangular with each atom having six nearest neighbours.

The appropriate rate for a diffusive event is still modelled using equation (4-3) but the activation energy is not pre-determined. As a system moves from one state (binding site) to another, its potential energy changes from one local energy minima to another, as illustrated in Figure 4.2 for a 1+1 dimensional surface. The transition energy peaks at the saddle point. The activation energy is defined to be the difference between the saddle-point energy and the initial binding site energy

$$E_i = E_{\text{saddle}} - E_{\text{binding}} \quad (4-5)$$

The saddle-point energy can be calculated from the current lattice configuration using a minimum energy path method. A frozen crystal [81][82] approximation is used to speed up the calculation of the activation energy. This means that all the atoms except the hopping atom are fixed during the transition process.

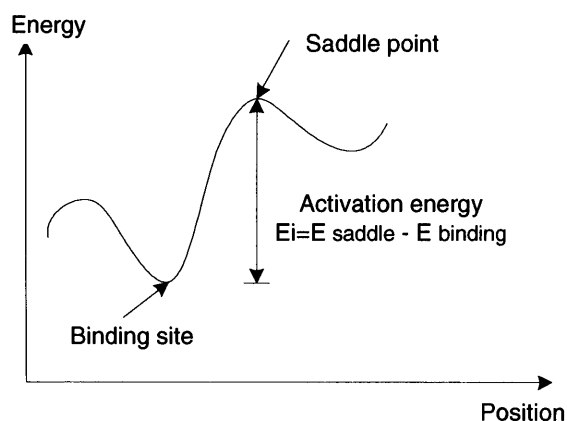


Figure 4.2 : Activation energy in 2D.

Another significant difference between on-lattice and off-lattice KMC is the complexity of determining the list of events. The events are pre-defined for a rigid (on-lattice) surface model but this is not the case for a flexible (off-lattice) model. Some rules for choosing events must be defined. These rules depend on the positions of atomic nearest neighbours (see Figure 4.3). For simplicity we label atomic six neighbours R (for right neighbour), RU (for right-upper), RD (for right-down), L (for left), LU (for left-upper) and LD (for left-down neighbour). To ensure that an atom is always in a stable position, it is assumed that an atom must always have RD and LD neighbours and that an atom can only hop a distance less than two atomic spacings. Consequently, the following steps are used in the off-lattice KMC simulation to determine the list of events :

1. Identify all movable surface atoms. A movable atom can be identified in terms of the situation of its nearest neighbours (see Figure 4.3). An atom is taken to be movable if both the RU and LU positions are empty, i.e. it has no neighbouring atoms immediately above it. A secondary criteria that a movable atom must fulfil is that its nearest R or L neighbour is also movable or vacant, otherwise there is not a neighbouring vacant site available for the movable atom to move into.
2. A hopping event for a movable atom is only possible in the direction of a nearby vacant receptor site. There are six receptor sites for a movable atom. These are shown in Figure 4.4 and fall into the following three categories :
 - a1/a2 sites – the atom in R/L position is also a movable atom and also has a R/L neighbour respectively.
 - b1/b2 sites – there is no R/L atom but the RD/LD atom has a R/L atom respectively.
 - c1/c2 sites –there is no R/L atom and RD/LD atom has no R/L atom respectively.

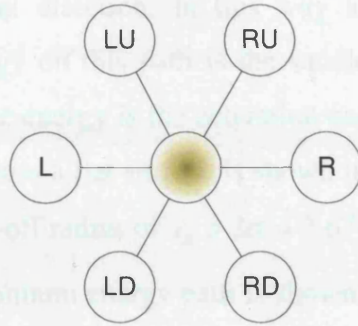


Figure 4.3 : Definition of an atom neighbouring sites : right (R), right-upper (RU), right-down (RD), left (L), left-upper (LU) and left-down (LD).

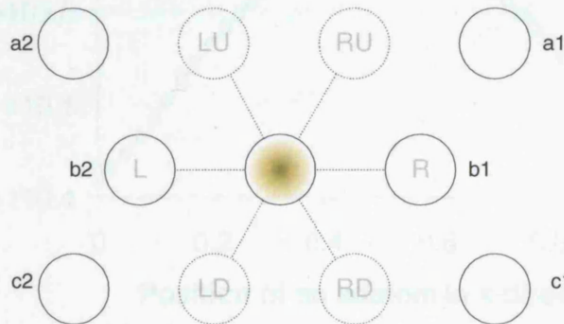


Figure 4.4 : There are six possible receptor sites (a1, a2, b1, b2, c1 and c2) for a movable atom to hop into if vacant.

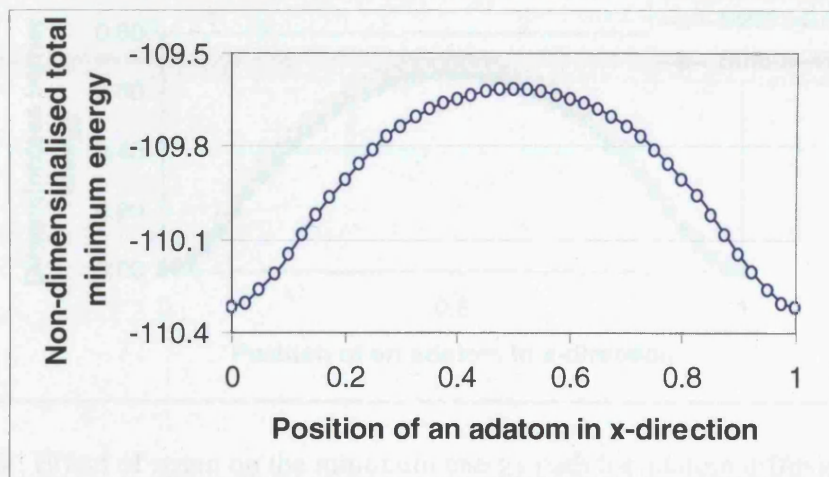
4.3 Calculating the activation energies

The activation energies calculated in the off-lattice KMC simulation are determined from the instantaneous crystallographic arrangement. However, the magnitude of these energies is explored in this section for various diffusive events of particular importance.

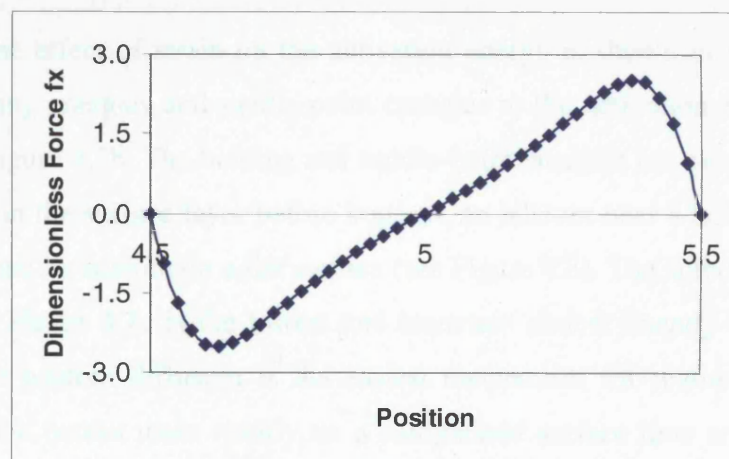
4.3.1 Adatom diffusion on an unstrained flat surface

For a 1+1 dimensional surface, the minimum energy path method [81][82] is employed to calculate the saddle-point energy and bind-site energy for various transition events. In this method, an atom is moved horizontally across the surface of a frozen lattice to a new bind site

in a sequence of steps of $a/40$, where a is the atomic spacing. After each step the atom is allowed to relax in the vertical direction. In this way a minimum energy path can be calculated. The maximum energy on this path is the saddle-point energy. The saddle-point energy minus the initial bind-site energy is the activation energy (4-5). The minimum energy path for an adatom diffusing across a flat surface is shown in Figure 4.5a. The LJ interatomic potential is employed with a cut-off radius of $r_{ij} > 3\sigma \approx 2.67r_0$. The horizontal force acting on the adatom as it follows the minimum energy path is shown in Figure 4.5b. The force is zero at the bind-sites and the saddle-point. This means that they are extremum points. It is useful to note that if we choose the same material parameters as those used by Biehl and Much [71] we get the same activation barrier of $E_i \approx 0.57eV$.



(a)



(b)

Figure 4.5 : (a) The minimum energy path for an adatom hopping between two sites on an unstrained flat surface. (b) The horizontal force on the adatom during the transition.

4.3.2 Diffusion on a strained flat surface

Heteroepitaxial thin films can be highly strained. It is therefore necessary to study the relationship between activation energy and strain. There is a mismatch strain of $\epsilon_x = -4\%$ for the typical semiconductor system of Ge on Si. Figure 4.6 shows that the activation energy for adatom diffusion with the LJ potential will reduce from 0.7 eV for zero strain to 0.66 eV for a strain of -4%. This means that adatom diffusion is easier on a compressed lattice than an unstrained lattice.

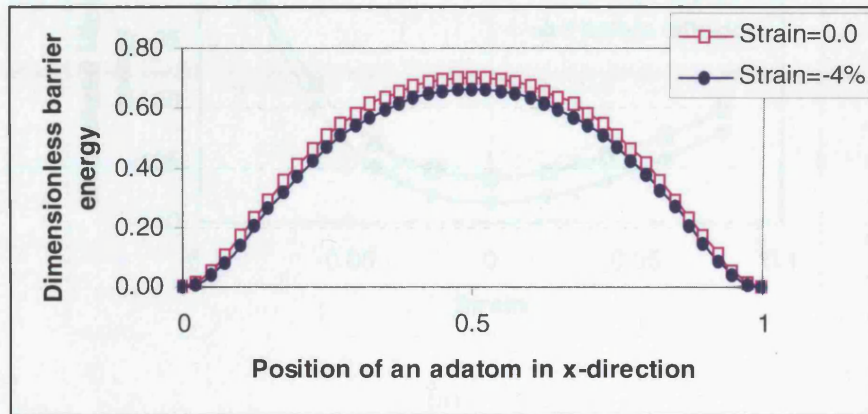
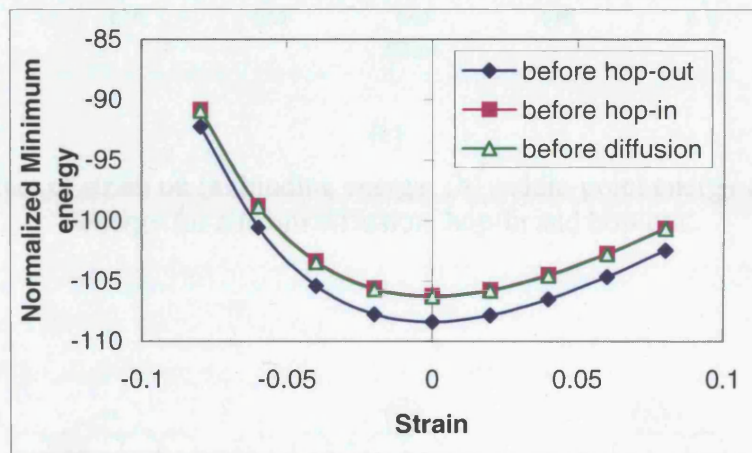


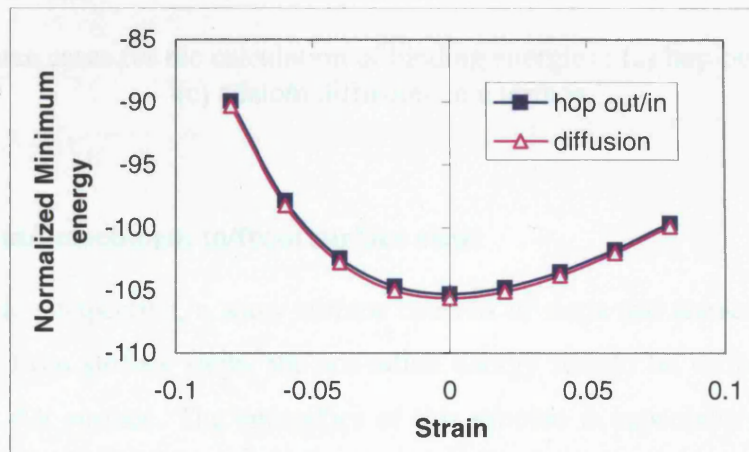
Figure 4.6 : Effect of strain on the minimum energy path for adatom diffusion on a flat surface.

More detail about the effect of strain on the activation energy is shown in Figure 4.7. The contribution of binding energies and saddle-point energies to the activation energy is shown in Figure 4.7a and Figure 4.7b. The binding and saddle-point energies are calculated for three cases here: an atom in the surface layer before hop-out, an adatom near a hole in the surface layer before hop-in and an adatom on a flat surface (see Figure 4.8). The activation energy for adatom diffusion in Figure 4.7c is the lowest and increases almost linearly with increasing tensile strain. Hence adatom diffusion is the easiest mechanism for rearrangement of the surface material and it occurs more readily on a compressed surface than an extended one. This is interesting as linear continuum theory predicts that the sign of the strain does not influence the evolution of heteroepitaxial systems, although experimentally this has been observed to have an effect [4]. The activation energy for an adatom hopping into a hole in the surface is slightly higher but obeys a similar relationship. Hop-in has a higher saddle-point

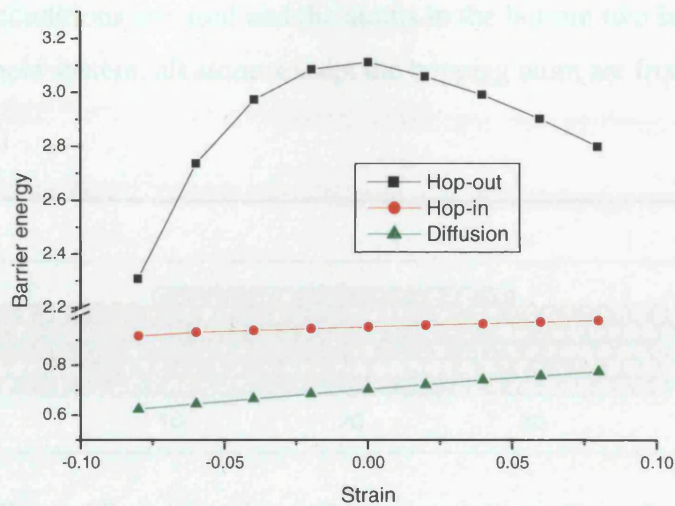
energy than adatom diffusion because the atom that would occupy the vacant hole site is not there to help pull the adatom through its transition. The highest activation energy in Figure 4.7c is for an atom hopping out of the surface. This is significantly higher than for the other mechanisms and hence will be a relatively infrequent event. It is high because the atom has a very low binding energy when embedded in the surface. The hop-out activation energy is an approximately quadratic function of strain, i.e. either tensile or compressive strain aids hopping out of the surface. This is because the moving atom has two lateral neighbours in this case.



(a)



(b)



(c)

Figure 4.7 : Effect of strain on (a) binding energy, (b) saddle-point energy and (c) activation energy for adatom diffusion, hop-in and hop-out.

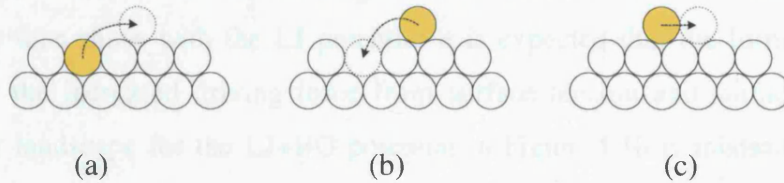


Figure 4.8 : Three cases for the calculation of binding energies : (a) hop-out, (b) hop-in and (c) adatom diffusion on a terrace.

4.3.3. Attachment/detachment to/from surface steps

From an atomistic perspective, a wavy surface consists of steps and terraces. When adatoms attach or detach from surface steps, the activation energy should be different from that for diffusion over a flat surface. The energetics of this process is especially critical below the roughening transition temperature. To investigate this we construct an island of atomic height on a flat surface, as shown in Figure 4.9. A representative atom is then dragged over the island to find its minimum energy path. The energy landscape obtained in this manner is shown in Figure 4.10 for the LJ potential and LJ+BO potentials. In the case of LJ +BO, the crystal needs to be relaxed (to minimize its total potential energy) as this interatomic model induces a surface stress which is discontinuous due to the steps in the surface (see Chapter 3).

Periodic boundary conditions are used and the atoms in the bottom two layers are fixed. After relaxation of the whole system, all atoms except the hopping atom are frozen.

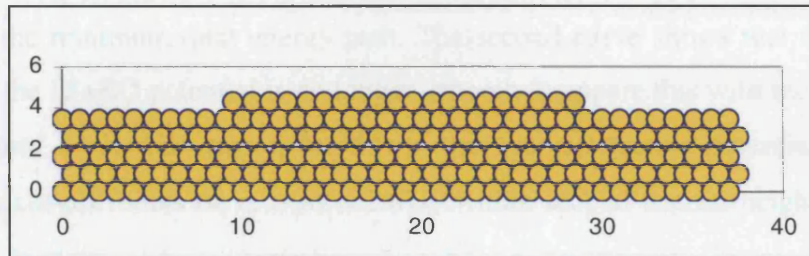


Figure 4.9 : Initial island of atomic height on the surface.

The adatom energy landscape for the LJ and LJ+BO potentials shown in Figure 4.10 was obtained by moving an adatom over the surface. Here adatom energy refers to the potential energy of the representative adatom calculated from its nearest- neighbour and second nearest-neighbour bonds. One can find in this instance that the diffusion barrier for LJ+BO is bigger than that for LJ. Although surface atoms with the LJ+BO potential have stronger bonds than those with the LJ potential it is expected that the former will be more mobile due to the increased driving force from surface tension and surface stress. So the adatom energy landscape for the LJ+BO potential in Figure 4.10 is misleading as the bond energy of the atoms neighbouring the moving adatom also changes as their coordination number (and hence bond order) changes.

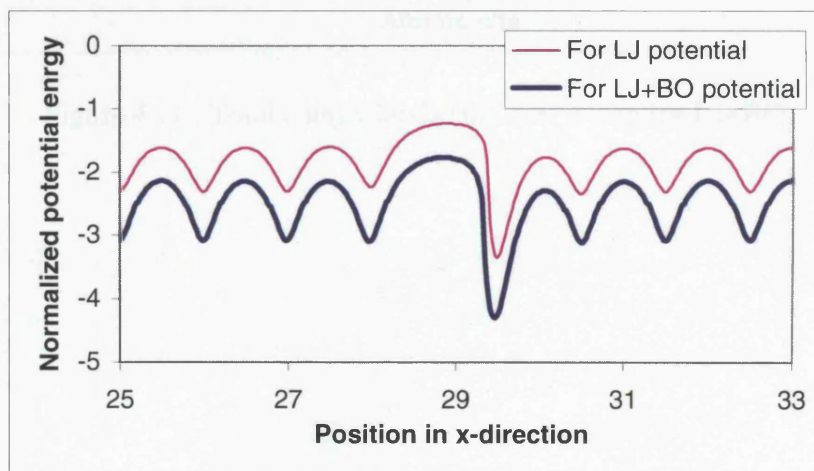


Figure 4.10 : Energy landscape over a surface step for LJ and LJ+BO potentials.

Figure 4.11 shows the change in the total energy of all the atoms except the adatom and also the change in the total energy of all atoms including the adatom. As expected, the first curve is not constant during adatom movement because the bond order of the atoms surrounding the representative adatom varies as well as that of the representative adatom as it moves along the minimum total energy path. The second curve shows that the total energy landscape for the LJ+BO potential is no longer smooth (compare this with the adatom energy curves in Figure 4.10). The reason for this is that the interatomic potential calculation is restricted to a cut-off radius of $r_{ij} > 3\sigma \approx 2.67r_0$ within second nearest-neighbour range and that the bond strengths undergo a discrete change as the coordination number of the adatom changes. However this does not affect the value of the activation energy. The correct energy landscape including the change in energy of all the atoms is shown for both potentials in Figure 4.12.

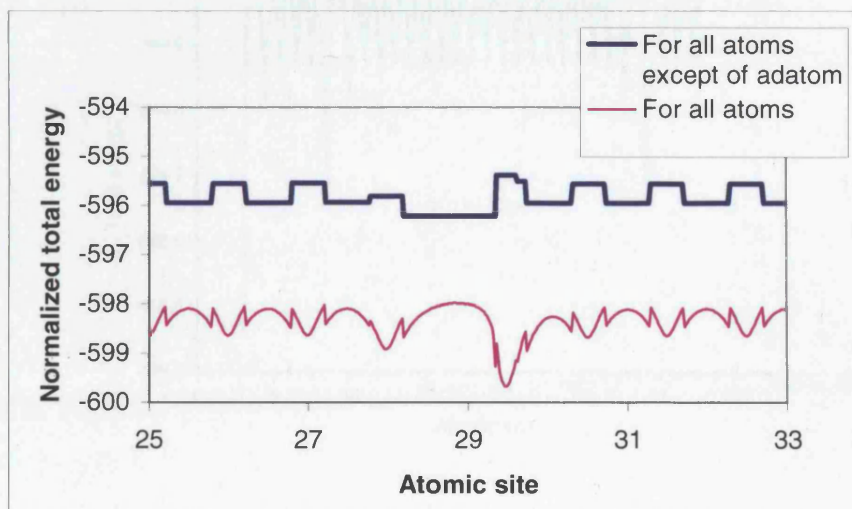
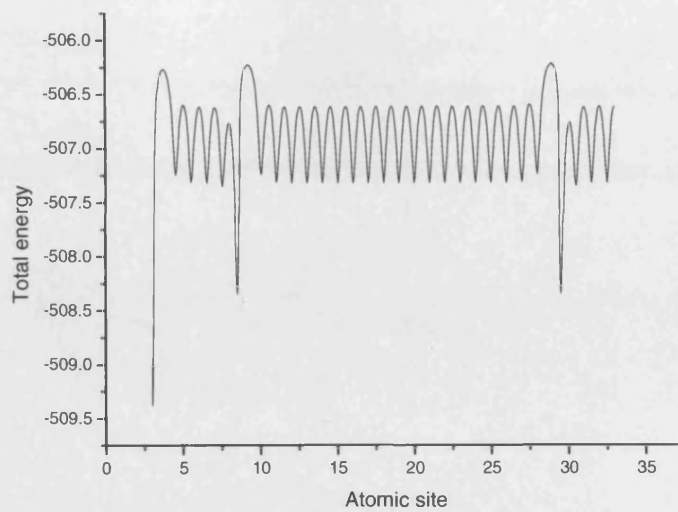
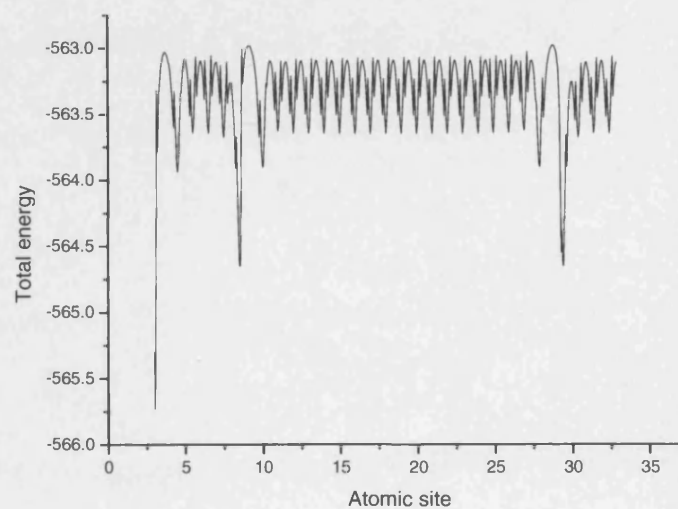


Figure 4.11 : Total energy landscape over a step for LJ+BO.



(a)

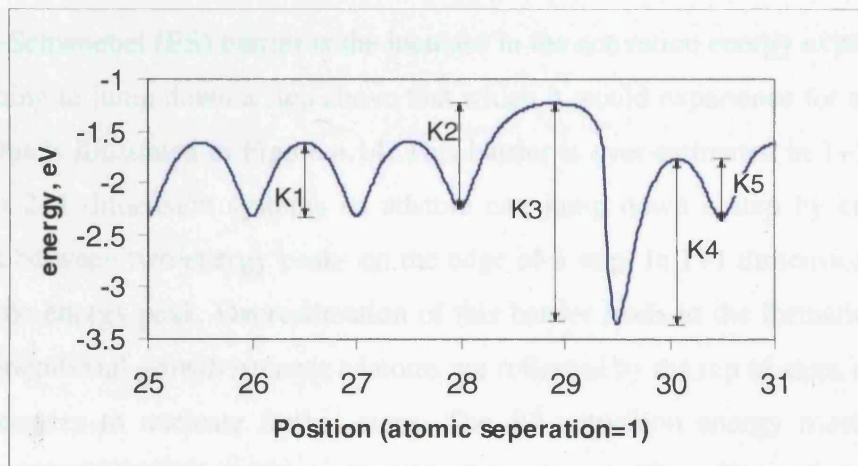
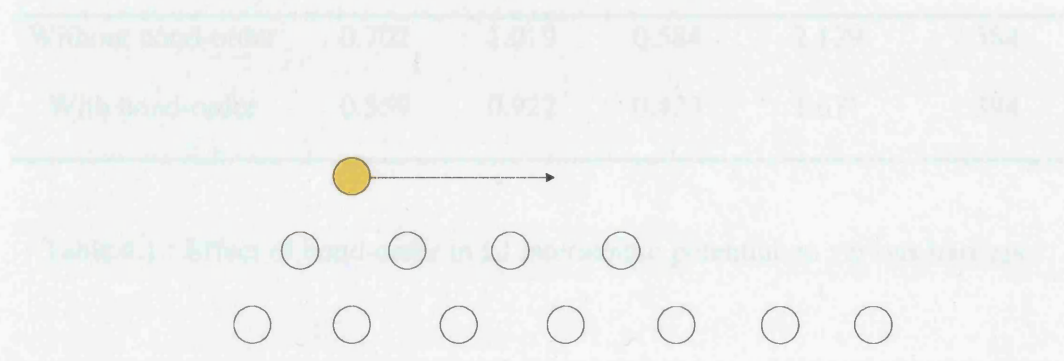


(b)

Figure 4.12 : Total energy landscape of representative atom dragged over the island for (a) LJ and (b) LJ+BO potentials

The schematic energy landscape in Figure 4.13 demonstrates that there are a few energy barriers which dominate the global diffusion process. The activation energies for the five associated events are labelled $K1$ through to $K5$ as shown in Figure 4.13a. Here $K1$ is the adatom diffusion barrier or the activation energy for terrace diffusion. The barriers for attaching to a step from the upper terrace and from the step terrace are $K2$ and $K5$ respectively. $K2$ includes the Ehrlich-Schwoebel barrier. This will be discussed in more detail in the next subsection. The barriers for detaching from a step to the upper terrace and

the step terrace are $K3$ and $K4$ respectively. The results from Figure 4.12 are listed in Table 4.1. When bond-order is considered in the LJ potential model, the surface diffusion barrier $K1$ is $0.56U_0$ smaller than the barrier without bond-order where U_0 is the unit of energy in the LJ potential. This is consistent with previous results : adatoms will diffuse easier with bond-order than without due to the tensile surface strain associated with the bond-order potential.



(a)



(b)

Figure 4.13 : Five key events for surface diffusion. (a) Schematic of the energy landscape for an adatom dragged over a surface step showing energy barrier for associated events. (b) $K2$ and $K5$ are barriers for attaching to a step from the terrace above and the step terrace respectively; $K3$ and $K4$ are barriers for detaching from a step to the upper terrace and to the step terrace respectively; $K1$ is the barrier for adatom diffusion on a terrace.

LJ potential	Barriers (unit: U_o)				
	Diffusion	Attaching step			Detaching step
	K1	K2	K5	K3	K4
Without bond-order	0.702	1.019	0.584	2.129	1.584
With bond-order	0.559	0.922	0.423	1.671	1.394

Table 4.1 : Effect of bond-order in LJ interatomic potential on various barriers.

4.3.4 The Ehrlich-Schwoebel barrier

The Ehrlich-Schwoebel (ES) barrier is the increase in the activation energy experienced by an adatom wishing to jump down a step above that which it would experience for normal terrace diffusion. This is illustrated in Figure 4.14. This barrier is over-estimated in 1+1 dimensional systems. In 2+1 dimension systems an adatom can jump down a step by crossing at the saddle-point between two energy peaks on the edge of a step. In 1+1 dimensions the adatom must cross the energy peak. Overestimation of this barrier leads to the formation of mounds even in homoepitaxial growth because adatoms are reflected by the top of steps and remain on the upper terraces to nucleate further steps. The $K2$ activation energy must therefore be manually corrected to avoid this unphysical phenomenon. The affect of the size of the correction will be investigated in the numerical simulations of the next section.

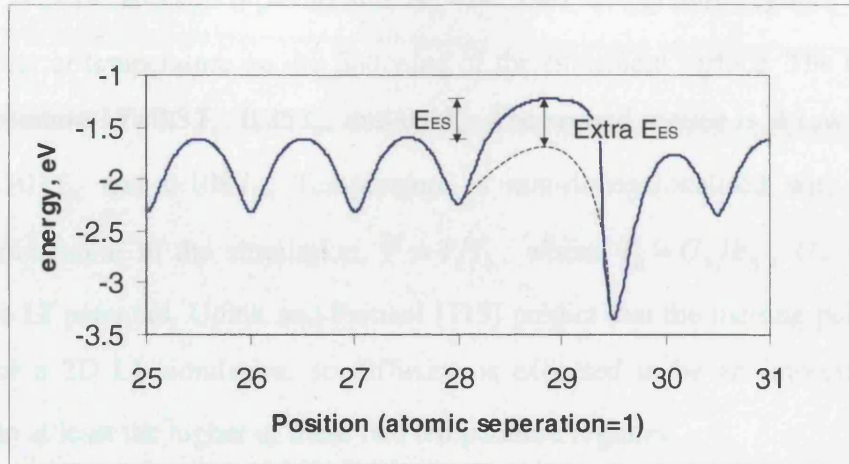


Figure 4.14 : Energy landscape over a step showing the Ehrlich-Schwoebel barrier for an adatom descending a step. The upper terrace is up to position 28.5, the lower terrace is position 29 onwards.

4.4 Decay of an unstrained sinusoidal surface

4.4.1 Off-lattice KMC simulations

In this section the evolution of an unstrained surface is modelled. The surface is initiated with a sinusoidal surface profile. The Herring-Mullins equation (4-1) predicts that the surface profile will evolve as a sinusoid and that the amplitude will decay exponentially with time (4-2). The amplitude of the sinusoid is monitored during the evolution and is determined from the discrete Fourier series for a sinusoid of wavelength λ as

$$A = \frac{2}{\lambda} \sum_{i=1}^N h_i \sin\left(\frac{2\pi}{\lambda} x_i\right) \Delta x. \quad (4-6)$$

The initial configuration of the simulation has an amplitude of $A = \frac{1}{3} N_y \Delta y$, with mean height $h_0 = \left(\frac{2}{3} N_y - 1\right) \Delta y$ and wavelength $\lambda = N_x \Delta x$, where N_x is the number of atoms in a monolayer, N_y is the number of layers, Δx is the atomic spacing and Δy is the distance between layers.

We take two sizes of sample to investigate the effect of the distance between steps: (1) $N_x=61$ and $N_y=14$; and (2) $N_x=150$ and $N_y=14$. Two temperature regimes are chosen to show the effect of temperature on the flattening of the sinusoidal surface. The first regime is at high temperature : $T=0.3T_0$, $0.35T_0$, and $0.4T_0$. The second regime is at low temperature : $T=0.1T_0$, $0.103T_0$ and $0.108T_0$. Temperature is non-dimensionalised with respect to a reference temperature in the simulation, $\bar{T} = T/T_0$, where $T_0 = U_0/k_B$, U_0 is the unit of energy in the LJ potential. Udink and Frenkel [113] predict that the melting point is at about $0.5T_0 \sim T_0$ for a 2D LJ simulation, so diffusion is expected to be an important relaxation mechanism in at least the higher of these two temperature regimes.

Note that KMC is a statistical simulation method. Simulations with the same initial starting conditions will give slightly different results. Ideally macroscopic parameters, such as diffusion coefficients, should be obtained from averaging over many such simulations. However, for the problems under investigation here, very little statistical scatter is observed in the diffusion data, so most results are obtained from only one or two simulations.

Simulation procedure

The off-lattice KMC simulation is conducted as follows:

- (1) Define initial configuration and enforce the periodic boundary conditions.
- (2) Identify all movable atoms.
- (3) Determine all events and their hopping intervals, i.e. the start site and end site.
- (4) Relax the lattice (i.e. minimize the energy):
 - Relax the lattice locally (within $R < 3\sigma_s \approx 2.67r_0$ around the latest event) after every event.
 - Only relax the lattice globally after every 10 events as this is computationally expensive.
- (5) Calculate the activation energies and the subsequent rate for all possible events.
- (6) Choose an event according to its probability and implement it.
- (7) Return to step (2) and repeat process until evolution period has been completed.

Eliminating the Ehrlich-Schwoebel barrier

As discussed in section 4.3.4, the Ehrlich-Schwoebel (ES) barrier should be eliminated for an event where an adatom attaches to a step edge from the terrace above. However, once the ES barrier is removed, simulations of the flattening of a sinusoidal surface still show that the surface tends to form mounds instead of a flat surface. The reason is that, after the elimination of the ES barrier, an adatom has the same probability to jump across the terrace as it does to jump down and attach to the step edge. This enhances the adatoms chances to remain on the upper terrace and join together with other adatoms and form mounds. Hence the ES barrier is still overestimated in the 1+1 dimensional case. Thus we eliminate an extra ES barrier (see Figure 4.14), say 1.2 times the ES barrier calculated in 1+1 dimensions. This increases the probability that an adatom will jump down from a terrace to attach to a step. When the off-lattice KMC simulation is performed again with this extra ES barrier elimination, the sinusoidal surface flattens. How large should the extra ES barrier elimination be and does it affect the evolution of the surface significantly? From Table 4.1, the ES barrier is K2-K1 which is $0.32U_0$ for the LJ potential and $0.36U_0$ for the LJ+BO potential. Two different values for the extra ES barrier were used, $0.45U_0$ and $0.65U_0$. Simulation results for the LJ+BO potential, shown in Figure 4.15, demonstrate that the evolution is only weakly dependent on the extra ES barrier height, i.e. attachment to a step from the upper terrace is no longer a rate-limiting process as expected.

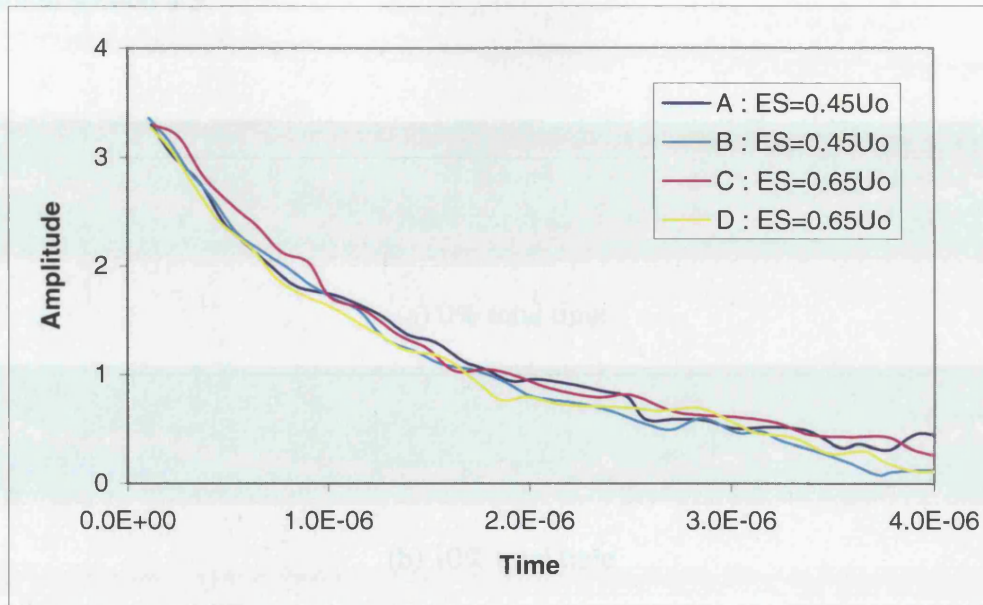


Figure 4.15 : The amplitude of sinusoidal profiles of wavelength $\bar{\lambda} = 61$ decay exponentially at a temperature of $\bar{T} = 0.3$ for the LJ+BO potential. Two curves (A & B) are produced by eliminating an extra Ehrlich-Schwoebel (ES) energy of $0.45 U_o$, the other two (C & D) by eliminating an extra ES energy $0.65 U_o$. This shows that eliminating an extra Ehrlich-Schwoebel energy to enhance diffusion of adatoms down steps does not affect off-lattice KMC simulations of the flattening of a sine wave above a certain value.

4.4.2 Flattening of a long wavelength sinusoid ($N_x = 150$)

(a) High temperature regime ($\bar{T} = 0.3-0.45$)

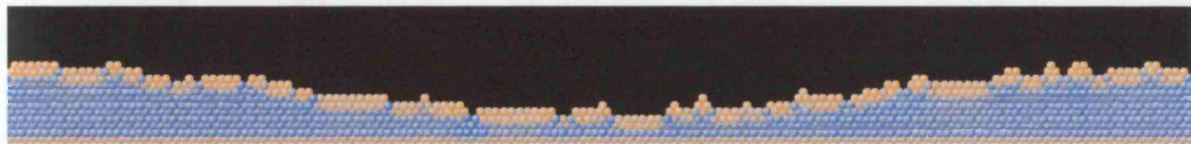
Here $N_x = 150$ and the distance between neighbouring steps in the initial morphology is about four atomic spacings. An example of the flattening of a sinusoidal surface at $\bar{T} = 0.45$ is shown in Figure 4.16. These results are for the LJ+BO potential and snapshots are taken at 0%, 10%, 20%, 40%, 70% and 100% of the total evolution time. At this high temperature the surface is rough but it retains a sinusoidal profile on average over time.

The decay of the natural log of the amplitude of a sinusoidal surface with time is shown in Figure 4.17 at three different high temperatures for the LJ and LJ+BO potentials. All the results are consistent with the exponential decay (4-2) predicted by Herring-Mullins

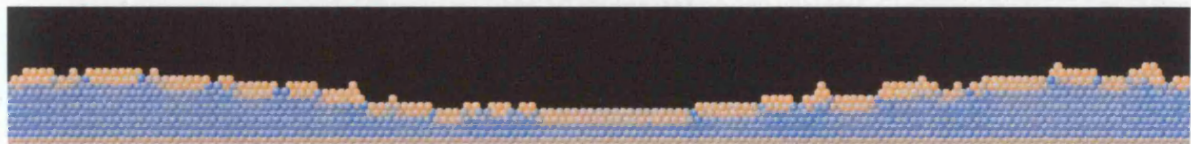
continuum theory (4-1). The LJ+BO potential case decays faster than the LJ case. This is discussed in section 4.5.



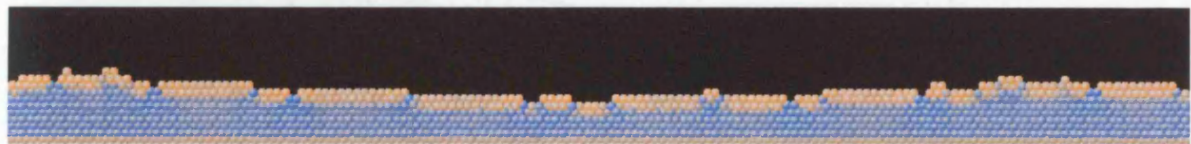
(a) 0% total time



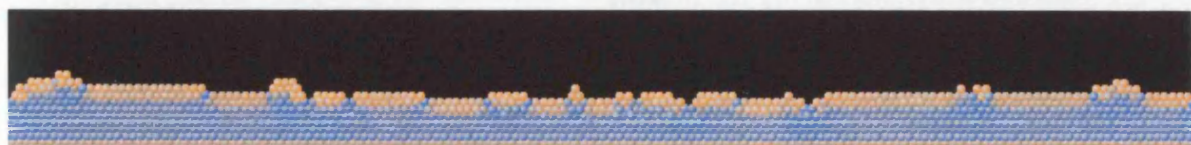
(b) 10% total time



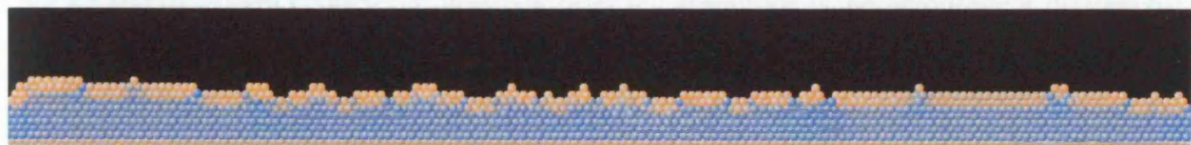
(c) 20% total time



(d) 40% total time

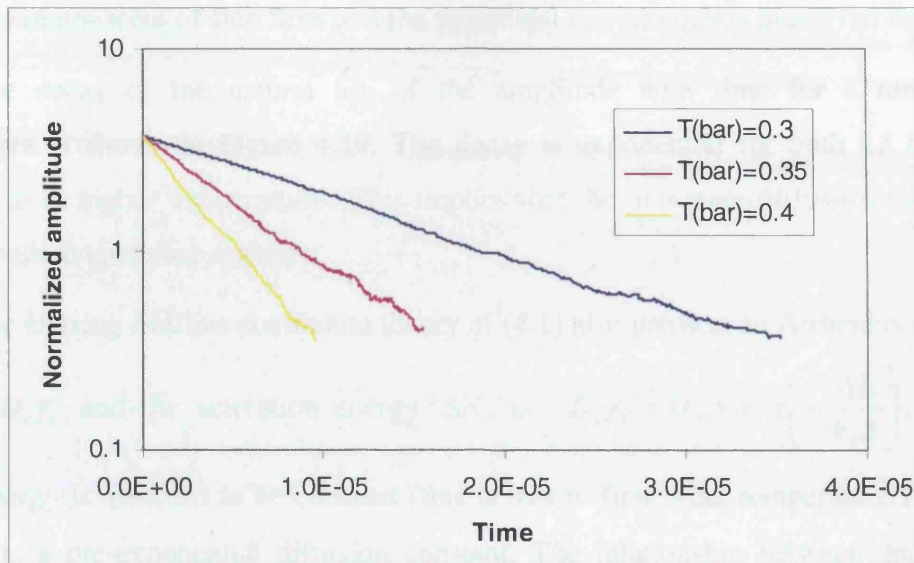


(e) 70% total time

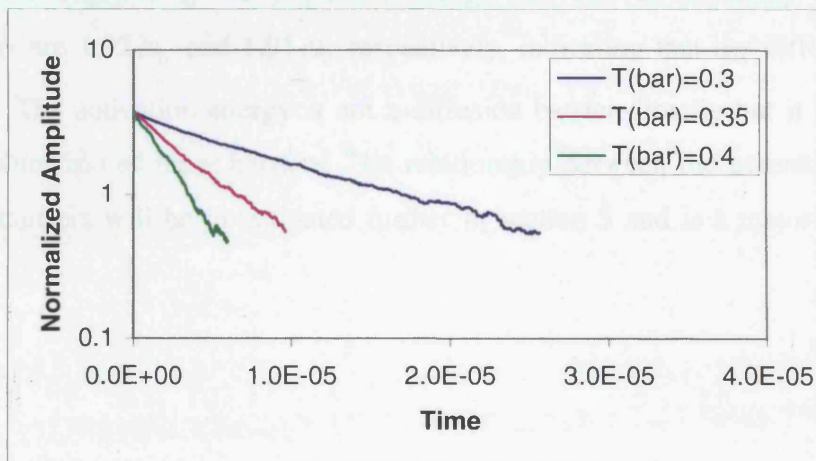


(f) 100% total time

Figure 4.16 : Flattening of a sinusoidal surface at high temperature ($T = 0.45T_0$) for large inter-step spacing ($N_x=150$) with BO at (a) 0%, (b) 10%, (c) 20%, (d) 40%, (e) 70% and (f) 100% of the total evolution time 37×10^{-6} . (Red indicates high strain and blue low strain.)



(a) LJ potential



(b) LJ+BO potential

Figure 4.17 : Amplitude (at the logarithmic scale) vs time plot showing the exponential decay of the amplitude of the sinusoidal surface at high temperatures and large inter-step spacing (a) for LJ and (b) LJ+BO potentials, where normalized amplitude is the amplitude A divided by the atomic spacing a .

(b) Low temperature regime ($\bar{T} = 0.1-0.108$)

An example of low temperature evolution for this wavelength ($N_x=150$) at $\bar{T} = 0.103$ for the LJ+BO potential is shown in Figure 4.18. Snapshots of the evolution are taken at the time 0%, 10%, 20%, 40%, 70% and 100% of the total evolution time. The surface is much smoother

than seen for the similar case at high temperatures (see Figure 4.16). The surface evolution is much more reminiscent of step flow and the sinusoidal morphology is preserved throughout.

The decay of the natural log of the amplitude with time for a range of low temperatures is shown in Figure 4.19. The decay is exponential for both LJ and LJ+BO potentials as at higher temperatures. This implies that the dominant diffusion process is the same for both temperature regimes.

The Herring-Mullins continuum theory of (4.1) also predicts an Arrhenius relationship between $D_s \gamma_s$ and the activation energy ΔE , i.e. $D_s \gamma_s = D_{s0} \gamma_s \exp\left(-\frac{\Delta E}{k_B T}\right)$, where the surface energy is assumed to be constant (this is true to first order temperature fluctuations) and D_{s0} is a pre-exponential diffusion constant. The relationship between $\ln(D_s \gamma_s)$ and inverse temperature for the results from Figure 4.17 and Figure 4.19 are shown in Figure 4.20. The slope is the negative of the activation energy. The activation energy for the LJ and LJ+BO models are $1.92 \omega_0$ and $1.91 \omega_0$ respectively, indicating that the difference between them is small. The activation energy is not a diffusion barrier directly but it is defined by a weighted combination of these barriers. The relationship between the activation energy and the diffusion barriers will be investigated further in section 5 and is a major motivation for this work.

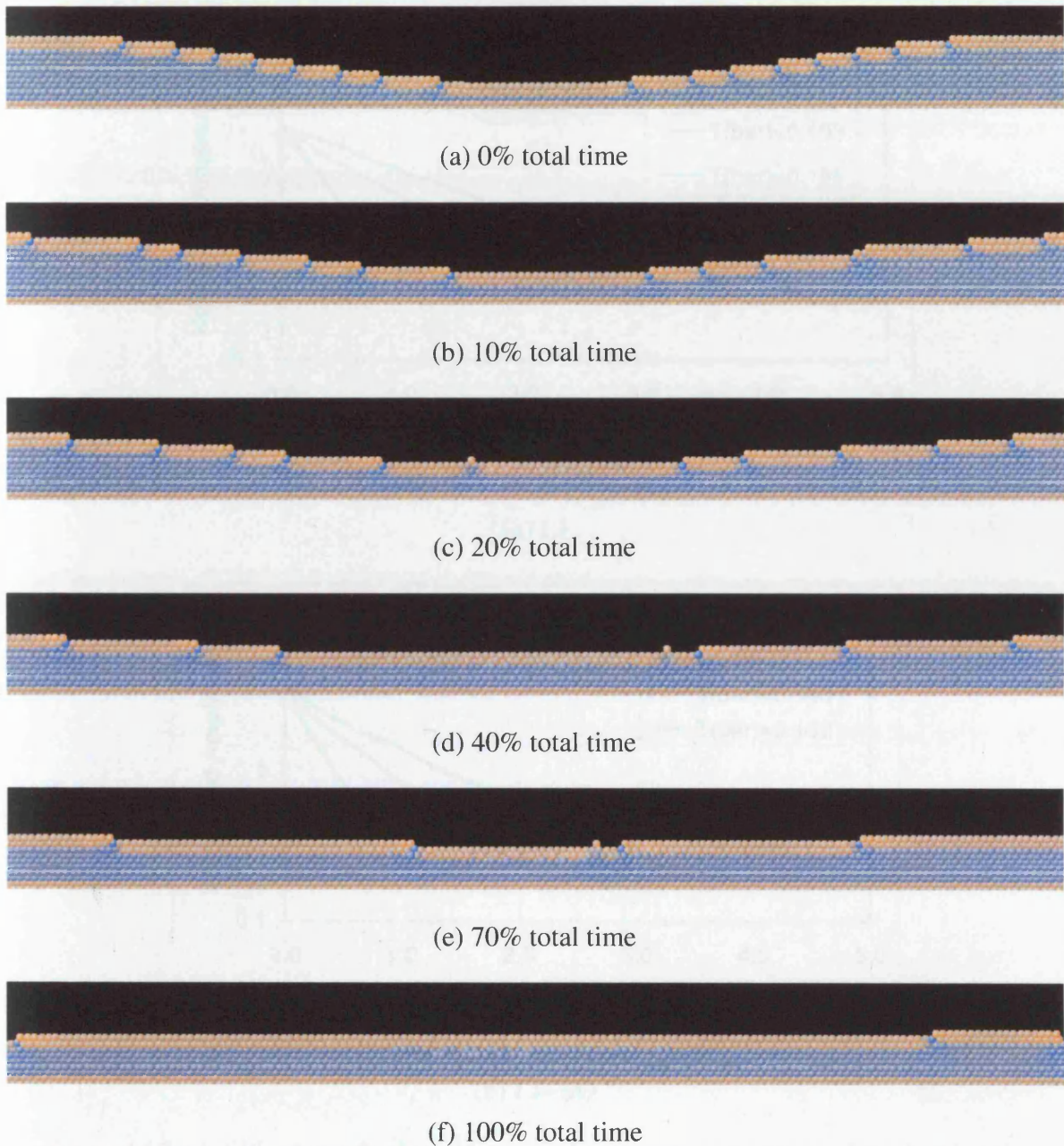
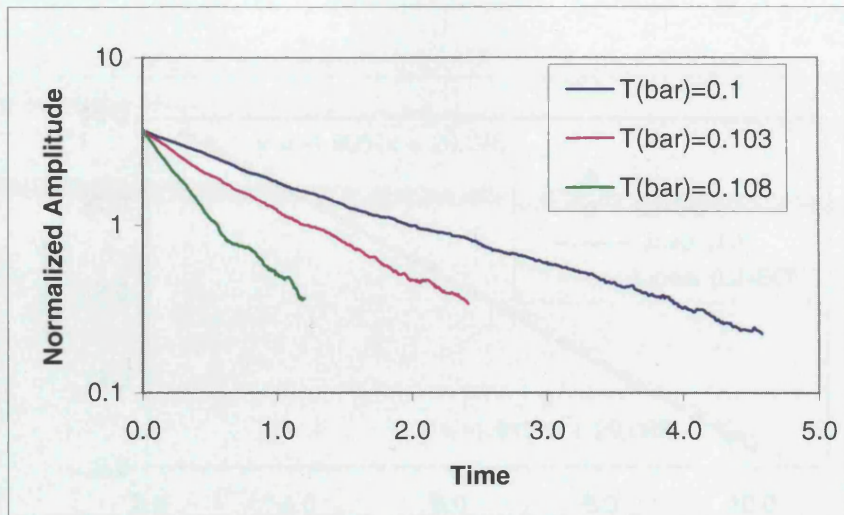
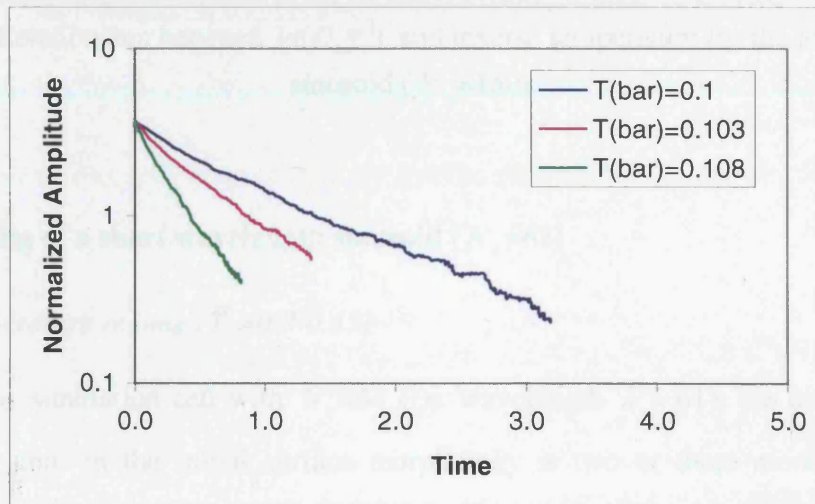


Figure 4.18 : Flattening of a sinusoidal surface at low temperature ($\bar{T} = 0.103$) for large inter-step spacing ($N_x=150$) with BO at (a) 0%, (b) 10%, (c) 20%, (d) 40%, (e) 70% and (f) 100% of the total evolution time.



(a) LJ



(b) LJ+BO

Figure 4.19 : Amplitude (at the logarithmic scale coordinates) vs time plots showing the exponential decay of the sinusoidal surface at low temperatures and large inter-step spacing (a) for LJ and (b) LJ+BO potentials.

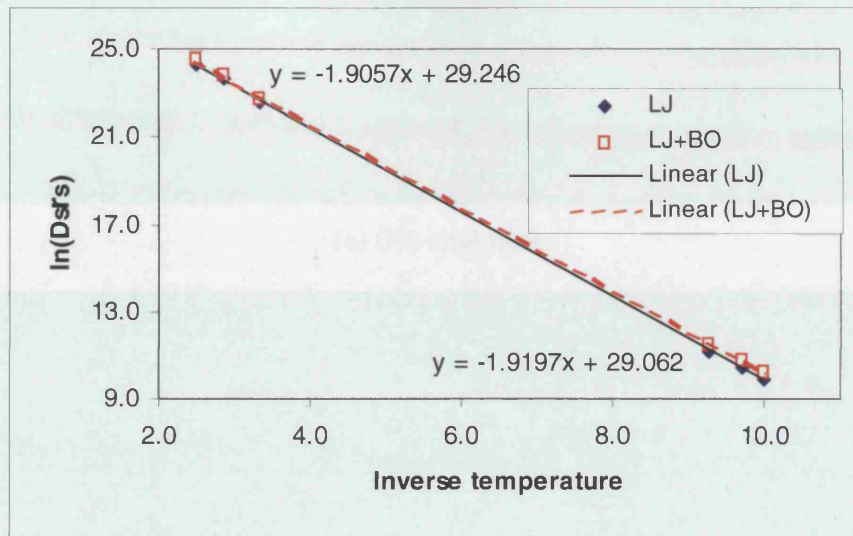


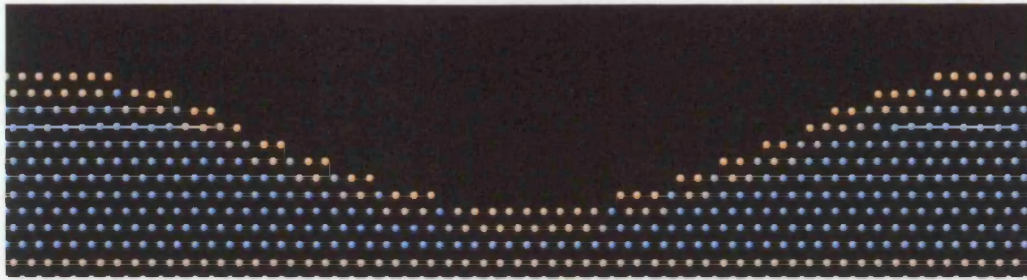
Figure 4.20 : Relationship between $\ln(D_s \gamma_s)$ and inverse temperature for the long wavelength sinusoid ($N_x=150$).

4.4.3 Flattening of a short wavelength sinusoid ($N_x=61$)

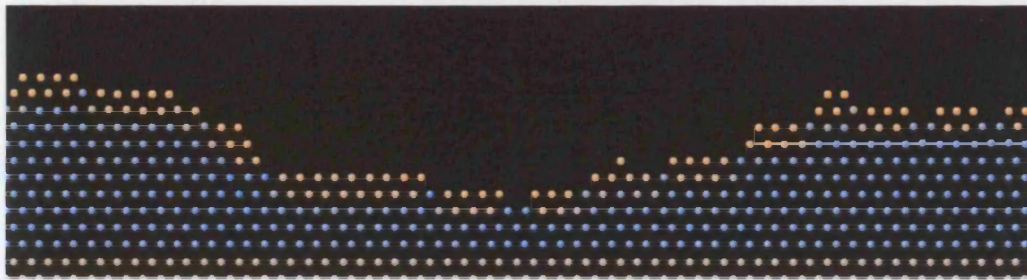
(a) High temperature regime ($\bar{T}=0.3-0.45$)

For the narrow simulation cell with $N_x=61$ (i.e. wavelength $\bar{\lambda} = 61$), the distance between neighbouring steps in the initial surface morphology is two or three atomic spacings. A typical example of the flattening of a sinusoidal surface at a high temperature of $\bar{T}=0.45$ is shown in Figure 4.21. The LJ+BO potential is used and the snapshots are taken at 0%, 10%, 40% and 100% of the total evolution time. As expected, the surface profile is rough at this high temperature but it retains a sinusoidal profile on average over time.

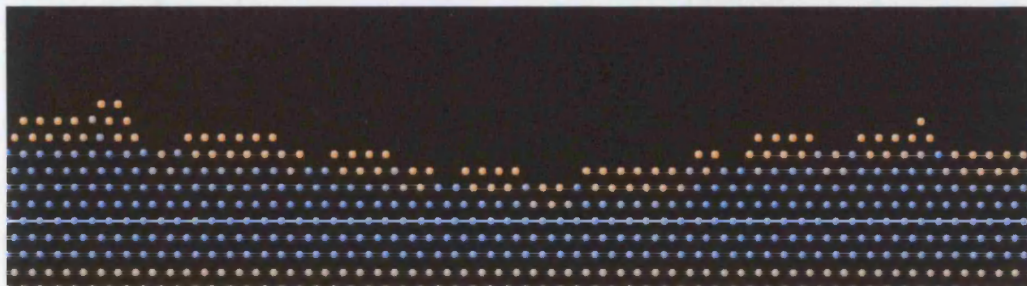
The decay of the amplitude of the sinusoidal surface over time for cases with and without bond-order is shown in Figure 4.22 (a) and (b) at three different high temperatures. The lower the temperature, the slower the decay of the wavy surface as expected. Figure 4.22 shows that the decay of the amplitude at the logarithmic scale is linear for these temperatures which indicates exponential decay, in agreement with the Herring-Mullins continuum theory of (4-2).



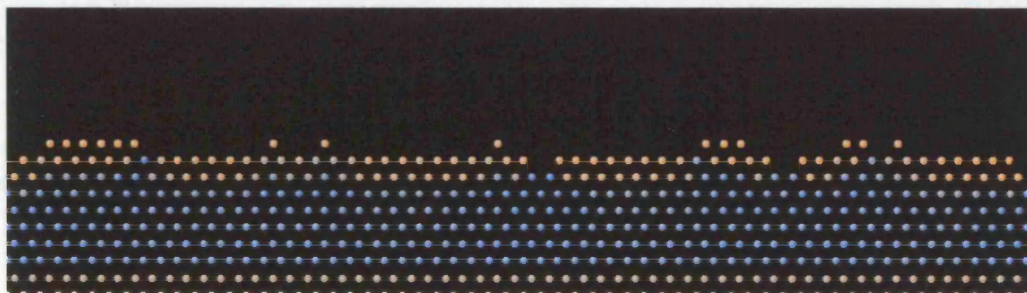
(a) 0% total time



(b) 10% total time

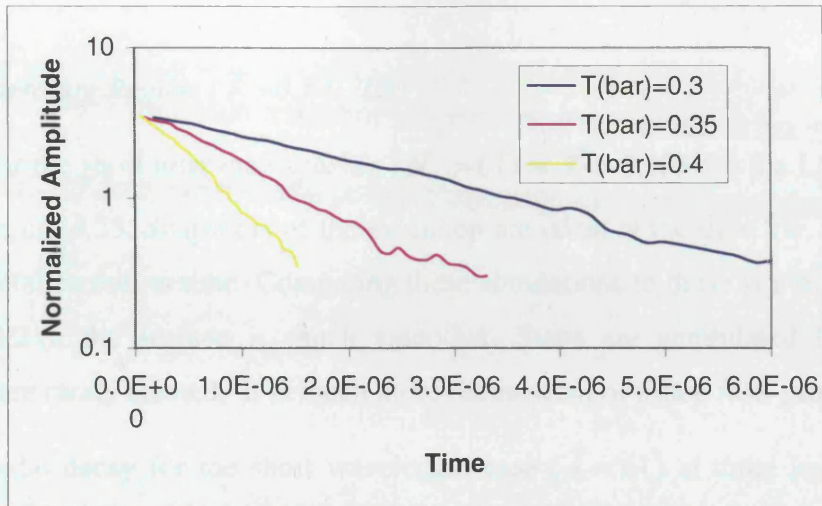


(c) 40% total time

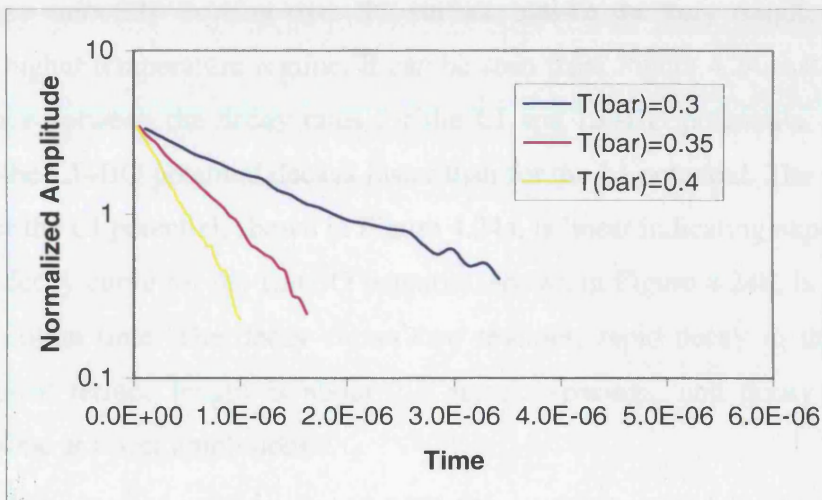


(d) 100% total time

Figure 4.21 : Flattening of a sinusoidal surface at high temperature ($T = 0.45T_0$) for short inter-step spacing ($N_x=61$) with BO at (a) 0%, (b) 10%, (c) 40% and (d) 100% of the total evolution time 3×10^{-6} . (Red indicates high strain and blue indicates low strain. The colour scheme is the same as Figure 4.16. The only different is the size of the visualised atoms).



(a) LJ potential



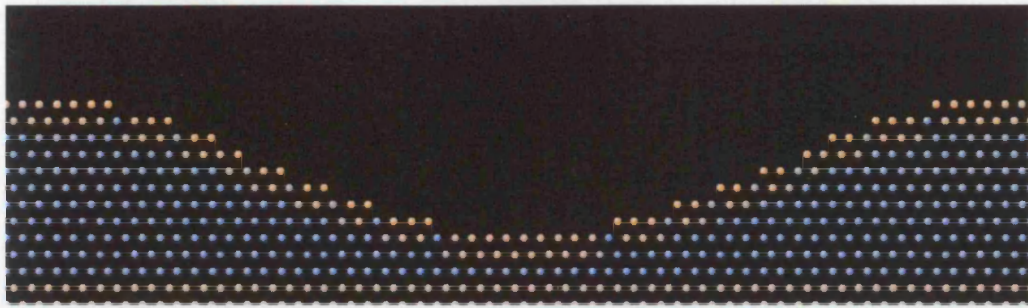
(b) LJ+BO potential

Figure 4.22 : Amplitude at logarithmic scale vs time plot showing the exponential decay of the amplitude of the sinusoidal surface at high temperatures and small inter-step spacing (a) for LJ and (b) LJ+BO potentials

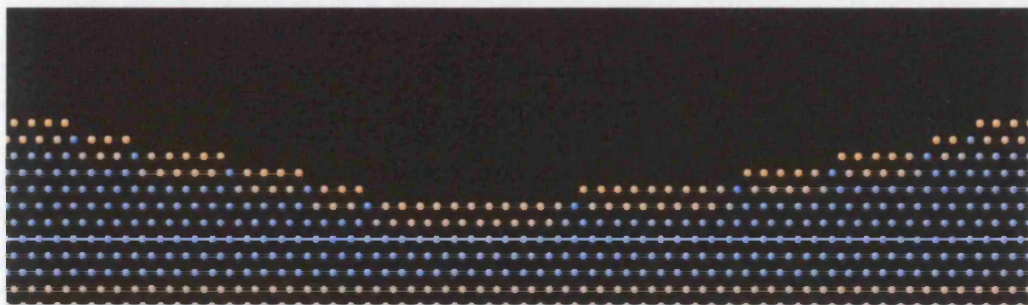
(b) Low Temperature Regime ($\bar{T} = 0.1-0.108$)

An example for the short inter-step spacing ($N_x = 61$) at $\bar{T} = 0.103$ for the LJ+BO potential is shown in Figure 4.23. Snapshots of the evolution are taken at the time 0%, 20%, 40% and 100% of the total evolution time. Comparing these simulations to those at a high temperature (see Figure 4.21), the surface is much smoother. Steps are annihilated by the surface flattening but are rarely created. It is much more reminiscent of a step flow process.

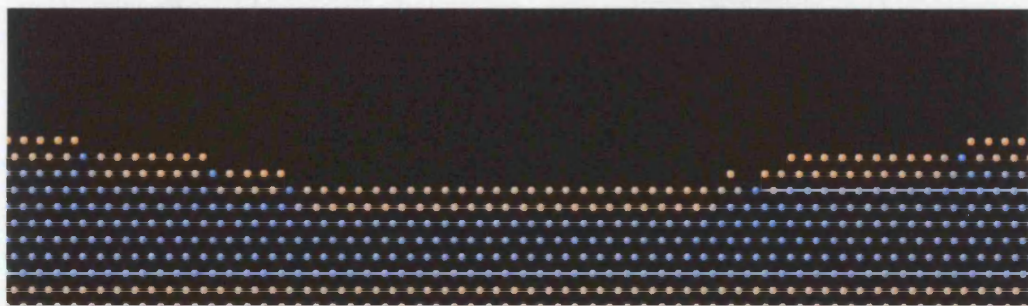
Sinusoidal decay for the short wavelength case ($\bar{\lambda} = 61$) at three low temperatures ($\bar{T} = 0.1, 0.103$ and 0.108) are investigated by off-lattice KMC simulation in Figure 4.24 for both the LJ and LJ+BO potentials. This low temperature evolution can be envisaged as a process of steps smoothly flowing over the surface, unlike the very rough, highly chaotic motion in the higher temperature regime. It can be seen from Figure 4.24 that there is now a larger difference between the decay rates for the LJ and LJ+BO potentials. As before, the amplitude for the LJ+BO potential decays faster than for the LJ potential. The log(amplitude) vs time plot for the LJ potential, shown in Figure 4.24a, is linear indicating exponential decay. However, the decay curve for the LJ+BO potential, shown in Figure 4.24b, is not linear over the whole evolution time. The decay shows two regimes: rapid decay in the initial stage, where the typical terrace length is about 2-3 atomic spacings, and decay with a longer characteristic time at lower amplitudes.



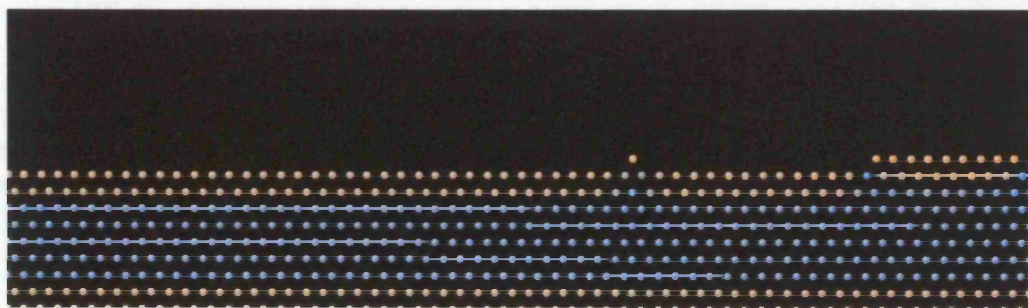
(a) 0% total time



(b) 20% total time

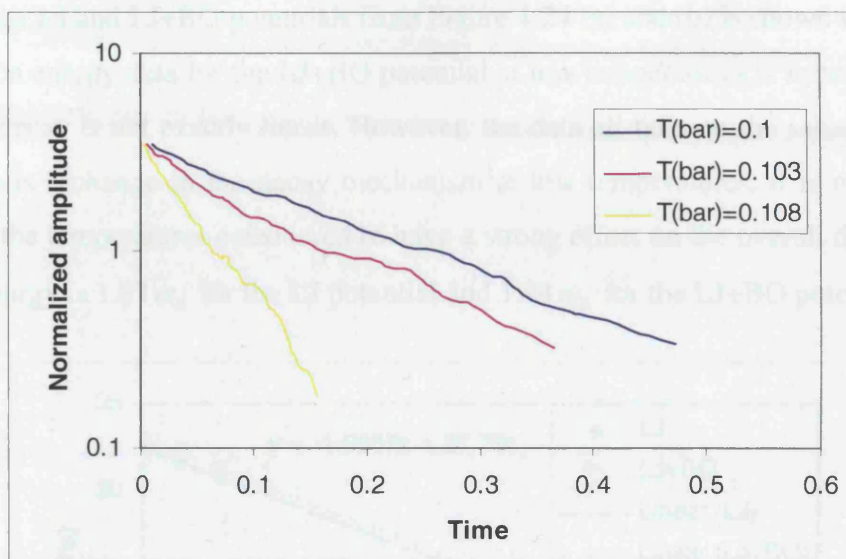


(c) 40% total time

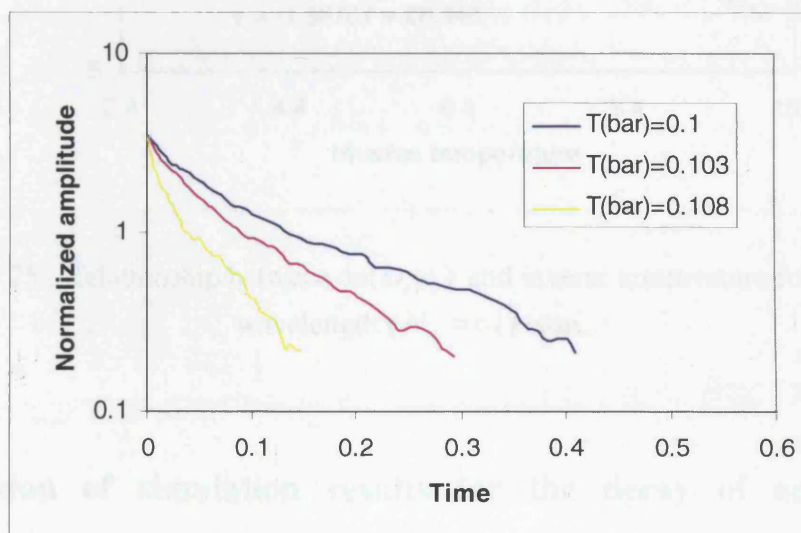


(d) 100% total time

Figure 4.23 : Flattening of a sinusoidal surface at low temperature ($\bar{T} = 0.103$) for small inter-step spacing ($N_x = 61$) with BO at (a) 0%, (b) 20%, (c) 40% and (f) 100% of the total evolution time.



(a) LJ potential



(b) LJ+BO potential.

Figure 4.24 : $\log(\text{Amplitude})$ vs time plots showing the decay of the sinusoidal surface at low temperatures and small inter-step spacing is (a) exponential for the LJ potential but (b) not so clearly exponential for the LJ+BO potential.

The relationship between $\ln(D_s \gamma_s)$ and inverse temperature for small inter-step spacing for the LJ and LJ+BO potentials from Figure 4.24 (a) and (b) is shown in Figure 4.25. The activation energy data for the LJ+BO potential at low temperatures is approximate as the logarithmic decay is not exactly linear. However, the data all falls on the same line showing that, if there is a change in the decay mechanism at low temperatures, it is not sufficiently dominant at the temperatures considered to have a strong effect on the overall decay rate. The activation energy is $1.87 \omega_0$ for the LJ potential and $1.94 \omega_0$ for the LJ+BO potential.

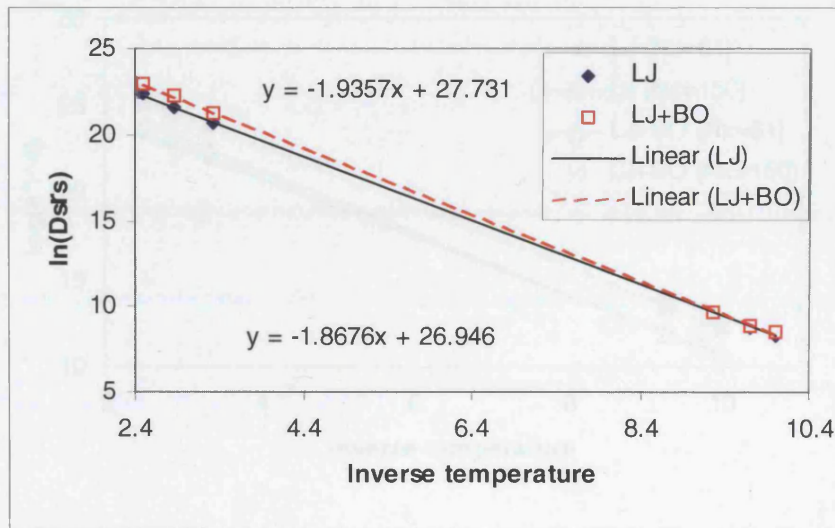


Figure 4.25 : Relationship between $\ln(D_s \gamma_s)$ and inverse temperature for the short wavelength ($N_x = 61$) case.

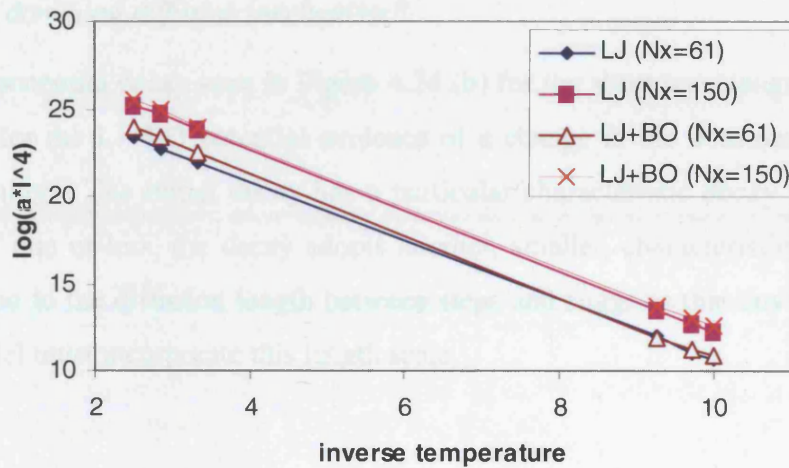
4.5 Discussion of simulation results for the decay of an unstrained sinusoidal surface

The simulation results of section 4.3 and 4.4 pose a number of questions. These questions will be addressed in the context of the step flow model of Chapter 5.

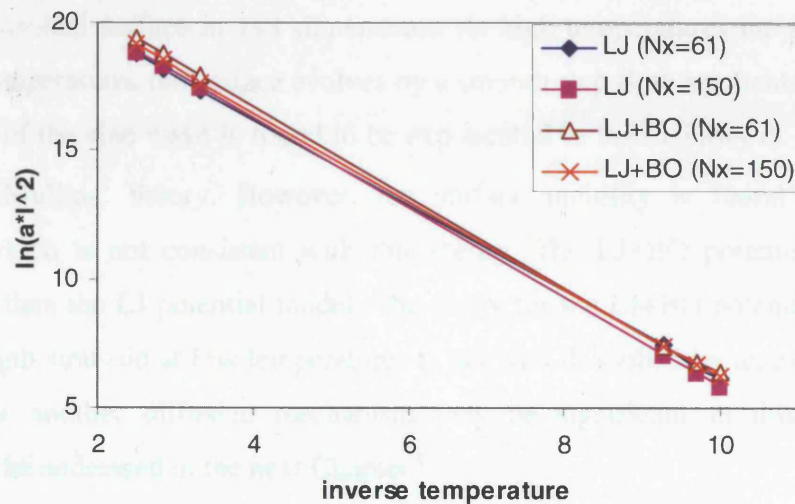
(a) Wavelength dependence

A sinusoidal surface obeying Herring-Mullins theory (4-2) will decay as a sinusoid and the amplitude will decay exponentially with a characteristic rate $\alpha = D_s \gamma_s (2\pi/\lambda)^4$ (A full derivation is given in Appendix E). This rate is the (negative) slope of the log(amplitude) vs time plots. This expression can be tested as it predicts that the mobility parameter, $D_s \gamma_s = \alpha(\lambda/2\pi)^4$, is only a function of temperature and independent of the sample

wavelength. Plotting $\alpha(\lambda/2\pi)^4$ against inverse temperature in Figure 4.26a for the two wavelengths considered shows that the mobility predictions do not coincide and hence suggests that the simulation results cannot be explained by Herring-Mullins theory. By contrast, a plot of $\alpha(\lambda/2\pi)^2$ against inverse temperature in Figure 4.26b demonstrates that the decay rate has a λ^{-2} dependence rather than a λ^{-4} dependence.



(a)



(b)

Figure 4.26 : Weighted characteristic decay rates as a function of inverse temperature for the LJ and LJ+BO potentials should give a wavelength independent mobility such that all points fall onto the same line. (a) $\alpha(\lambda/2\pi)^4$ shows that the decay rate does not have a λ^{-4} dependence and (b) $\alpha(\lambda/2\pi)^2$ shows that the decay rate does have a λ^{-2} dependence.

(b) Effect of bond order

In all cases, the LJ+BO potential simulations decay slightly faster than the LJ potential simulations. This could simply be because the dominant diffusion barriers are smaller for the LJ+BO potential. Another factor is the surface stress that accompanies the LJ+BO potential. This will cause an elastic deformation of the body and will generate a long range elastic interaction between steps. This could be significant in accelerating the decay or it may be negligible.

(c) Change in dominant diffusion mechanism?

Is the non-exponential decay seen in Figure 4.24 (b) for the short wavelength sinusoid at low temperatures for the LJ+BO potential evidence of a change in the dominant mechanism for surface flattening? The initial decay has a particular characteristic decay rate, but at small amplitudes of one or less, the decay adopts another, smaller, characteristic decay rate. This must be related to the diffusion length between steps and suggests that any pertinent surface diffusion model must incorporate this length scale.

4.6 Summary

Off-lattice KMC simulations have been employed to investigate the relaxation of an unstrained sinusoidal surface in 1+1 dimensions. At high temperatures the surface is rough, but at lower temperatures the surface evolves by a smooth step flow mechanism. The decay of the amplitude of the sine wave is found to be exponential in the majority of cases, consistent with Herring-Mullins' theory. However, the surface mobility is found to have a λ^{-2} dependence which is not consistent with this theory. The LJ+BO potential model decays slightly faster than the LJ potential model. The decay for the LJ+BO potential model for the short wavelength sinusoid at low temperatures is not well described by an exponential curve, indicating that another diffusion mechanism may be significant in this regime. These questions will be addressed in the next Chapter.

5.0 STEP FLOW MODELS OF SURFACE DIFFUSION

In the previous chapter, the flattening of an unstrained sinusoidal surface was investigated via off-lattice KMC simulations. At high temperatures and/or large wavelengths the decay of the amplitude was found to be exponential, as predicted by Herring-Mullins theory. The activation energy for the surface mobility is expected to be related to the energy barriers for the five basic diffusional processes. A macroscopic step flow model is investigated here in an attempt to relate the rates of these elemental processes to the overall macroscopic diffusion rate. In addition, it was found in chapter 4.0 that at low temperatures and small wavelengths the decay was not exponential. It is expected that the attachment/detachment kinetics at the steps becomes more important under these conditions. The underlying reason for this is investigated from the basis of the extended step flow models outlined in this section.

5.1 Basic step flow model for symmetric steps

From an atomistic point of view, a surface consists of a system of terraces bounded by steps as shown in Figure 5.1. Based on the dynamics of steps from the Burton-Cabrera-Frank (BCF) theory[26], a basic step flow model [55][56] has been developed to capture the motion of individual steps so as to investigate the evolution of the crystal surface. The basic model for symmetric steps is elaborated here and then extended to asymmetric steps in section 5.3. The symmetric step assumption means that a step interacts with its upper and lower terraces in an identical way.

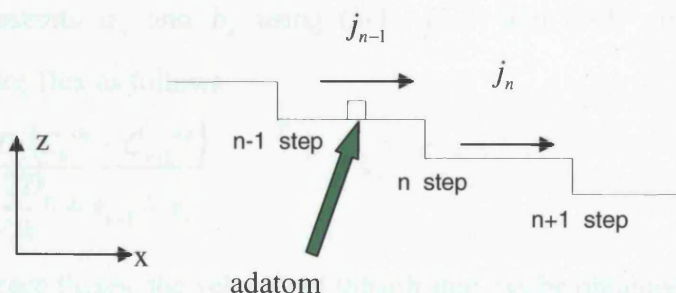


Figure 5.1 : Surface consists of multiple terraces and steps. Δx is the terrace length.

The n th terrace is between the n th and $(n+1)$ th steps. The atomic flux over the n th terrace due to the adatom concentration gradient is

$$J_n(x) = -D_s \nabla C_n(x) \quad (5-1)$$

where D_s is the adatom diffusion coefficient and $C_n(x)$ is the adatom concentration field on the n th terrace. Generally the time scale of step motion is much larger than that of surface diffusion. The adatom concentration field always reaches a steady state before the steps move. Thus the adatom concentration field $C_n(x)$ can be written as

$$C_n(x) = a_n + b_n x, \quad (5-2)$$

where a_n and b_n are constants, and x is the position on the terrace. The end steps of the n th terrace are at positions x_n and x_{n+1} so $x_n \leq x \leq x_{n+1}$. The step edge flux is determined by the attachment-detachment rate k as follows

$$\begin{aligned} J_n(x_n) &= -k [C_n(x_n) - C_n^{eq}] \\ J_n(x_{n+1}) &= k [C_n(x_{n+1}) - C_{n+1}^{eq}] \end{aligned} \quad (5-3)$$

where x_n is the position of the n th step and C_n^{eq} is the equilibrium adatom concentration at x_n , which depends on the step chemical potential μ_n as

$$C_n^{eq} = \tilde{C}^{eq} \exp\left(\frac{\mu_n}{k_B T}\right) \approx \tilde{C}^{eq} \left(1 + \frac{\mu_n}{k_B T}\right), \quad (5-4)$$

where \tilde{C}^{eq} is the equilibrium concentration of a non-interacting step, k_B is the Boltzmann constant and T is the absolute temperature. The chemical potential of a thermodynamic system is the amount by which the energy of the system would change if an addition particle were introduced without a change in the entropy and volume of the system. Here μ_n refers to the change in the energy due to addition of one atom to the face of step n . Eliminating the unknown constants a_n and b_n using (5-1), (5-2) and (5-3) yields an expression for the constant terrace flux as follows

$$J_n = \frac{D_s (C_n^{eq} - C_{n+1}^{eq})}{\frac{2D_s}{k} + x_{n+1} - x_n}. \quad (5-5)$$

Given the terrace fluxes, the velocity of the n th step can be obtained in terms of mass conservation such that

$$\frac{dx_n}{dt} = s_n \Omega (J_n - J_{n-1}) \quad (5-6)$$

where Ω is the atomic volume (area) of the solid and $s_n = \pm 1$ is the sign of the step. A step is said to have sign +1 if the upper terrace is to the right of the step and -1 if it is to the left of the step.

5.1.1 Diffusion Limited versus Attachment-Detachment Limited Growth

There are two extremes in the kinetics of this type of surface evolution model: diffusion limited (DL) growth and attachment-detachment limited (ADL) growth. The process which dominates depends on the relative magnitude of the terrace length Δx (see Figure 5.1) and the characteristic length D_s / k .

DL growth occurs if $2D_s / k \ll \Delta x$. In this case the surface evolution rate is limited by the diffusion of adatoms over the (possibly long) terraces and steps have little influence on the growth [55]. This is the classical picture of surface diffusion and leads to an exponential decay law.

ADL (or non-diffusion limited) growth occurs when $2D_s / k \gg \Delta x$ because diffusion over the terraces is relatively fast (they are short or diffusion is quick) and attachment-detachment to/from steps determines the evolution rate. This type of process is expected to lead to an inverse time decay law [55].

5.2 Macroscopic constants from interatomic potentials

This section relates some of the parameters in the step flow model, such as the adatom diffusion coefficient, D_s , the equilibrium concentration of a noninteracting step, \tilde{C}^{eq} , and the attachment-detachment rate, k , to the step energy profile model of Figure 4.13 in the previous chapter.

5.2.1 Equilibrium concentration of adatoms near a non-interacting step, \tilde{C}^{eq}

The adatom concentration, C^{eq} , is the density of adatoms per surface site, which is the probability that a surface site is occupied by an adatom. The equilibrium adatom density is often written as

$$\tilde{C}^{eq} = \exp\left(\frac{-\Delta E_{ad}}{k_B T}\right), \quad (5-7)$$

where ΔE_{ad} is the additional energy required to produce an adatom from the surface. The easiest mechanism for this is detachment of an atom from a step. Here we determine whether this model is correct and, if so, what the value of this additional energy is.

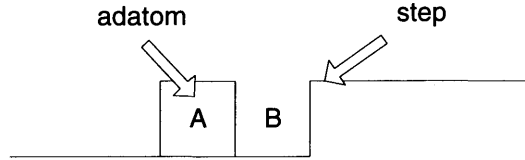


Figure 5.2 : An adatom near a noninteracting step.

At equilibrium, the rate of attachment of adatoms to a step depends on the probability that the site next to the step is occupied (position A in Figure 5.2) and is given by $C^{eq} r_{attach}$, where $r_{attach} = \nu_0 \exp(-k_{attach}/k_B T)$ and k_{attach} is the energy barrier to attachment to a step. Conversely, the rate of detachment of atoms from a step depends on the probability that the site next to the step is unoccupied and is $(1 - C^{eq}) r_{detach}$, where $r_{detach} = \nu_0 \exp(-k_{detach}/k_B T)$ and k_{detach} is the energy barrier to step detachment from a step. The energy barriers, k_{attach} and k_{detach} , can be determined from the interatomic potentials for a specific step configuration.

At equilibrium, the rate of attachment to a step should be equal to the rate of detachment from the step

$$C^{eq} \exp\left(\frac{-k_{attach}}{k_B T}\right) = (1 - C^{eq}) \exp\left(\frac{-k_{detach}}{k_B T}\right).$$

or

$$C^{eq} = \frac{\exp\left(\frac{-k_{detach}}{k_B T}\right)}{\exp\left(\frac{-k_{attach}}{k_B T}\right) + \exp\left(\frac{-k_{detach}}{k_B T}\right)} = \frac{1}{\exp\left(\frac{k_{detach} - k_{attach}}{k_B T}\right) + 1}. \quad (5-8)$$

The detachment energy barrier is normally greater than the attachment barrier. Therefore, at sufficiently low temperatures where $k_{detach} - k_{attach} \gg k_B T$, one can write

$$C^{eq} \approx \exp\left(\frac{-(k_{detach} - k_{attach})}{k_B T}\right).$$

Hence $\Delta E_{ad} = k_{detach} - k_{attach}$ for the symmetric step model.

For an isolated, non-interacting step, the energy barriers for attachment and detachment for the LJ and LJ+BO potentials are shown in Figure 4.12. If we denote these as $\tilde{k}_{\text{attach}}$ and $\tilde{k}_{\text{detach}}$ then the equilibrium adatom concentration around a non-interacting step is

$$\tilde{C}^{eq} = \frac{1}{\exp\left(\frac{\tilde{k}_{\text{detach}} - \tilde{k}_{\text{attach}}}{k_B T}\right) + 1}.$$

The effect of strain on barrier energies has been investigated in Figure 4.7c. It is clear that only the detachment (hop-out) process is strongly affected by strain and that it is independent of the sign of this strain (to first order). Also, the energy barrier decreases with strain. Therefore, if we denote the difference in chemical potential of the n th step above that of an isolated step (due to elastic interactions with other steps) to be μ_n then, to first order we can write the energy barriers as $\tilde{k}_{\text{attach}}$ and $\tilde{k}_{\text{detach}} - \mu_n$. The equilibrium concentration around the n th interacting step is therefore

$$C_n^{eq} = \frac{1}{\exp\left(\frac{\tilde{k}_{\text{detach}} - \tilde{k}_{\text{attach}} - \mu_n}{k_B T}\right) + 1} \approx \tilde{C}^{eq} \exp\left(\frac{\mu_n}{k_B T}\right) \quad (5-9)$$

where the second term is the approximation at low temperatures. This reproduces the regular expression (5-4).

5.2.2 The attachment-detachment rate, k

Step flow occurs under non-equilibrium conditions. In this case, the rate of attachment to a step is not equal to that of detachment from a step. A net flux results such that

$$J_n = C_n r_{\text{attach}} - (1 - C_n) r_{\text{detach}} = C_n (r_{\text{attach}} + r_{\text{detach}}) - r_{\text{detach}}. \quad (5-10)$$

where C_n is the (non-equilibrium) adatom concentration around the n th step. Equation (5-9) can be written as

$$C_n^{eq} (r_{\text{attach}} + r_{\text{detach}}) - r_{\text{detach}} = 0.$$

The flux (5-10) is then

$$J_n = (C_n - C_n^{eq}) (r_{\text{attach}} + r_{\text{detach}}). \quad (5-11)$$

Comparison with (5-3) gives the attachment-detachment rate as

$$\begin{aligned}
 k &= r_{\text{attach}} + r_{\text{detach}} \\
 &= v_0 \left(\exp\left(-\frac{\tilde{k}_{\text{attach}}}{k_B T}\right) + \exp\left(-\frac{(\tilde{k}_{\text{detach}} - \mu_n)}{k_B T}\right) \right) \\
 &= \frac{r_{\text{attach}}}{(1 - C_n^{\text{eq}})}
 \end{aligned} \tag{5-12}$$

using (5.9). In step flow models, k is assumed to be constant, but this indicates that it depends on the chemical potential of the step. However, at low temperatures, the adatom concentration is small and hence $k \approx r_{\text{attach}}$ is a constant.

5.2.3 The terrace diffusion coefficient, D_s

Consider two adjacent surface sites i and $i+1$ on the n th terrace far from a step such that they have the same chemical potential (excluding entropy). The adatom concentration on site i is denoted C_n^i etc. An adatom hopping from site i to site $i+1$ requires site i to be occupied and site $i+1$ to be unoccupied. Hence the hopping rate is given by $r_s C_n^i (1 - C_n^{i+1})$ where the rate for the hopping process is given by $r_s = v_0 \exp\left(-\frac{k_1}{k_B T}\right)$ and k_1 is the diffusion barrier for adatom diffusion on terraces (see Table 4.1). Conversely, an adatom hops from site $i+1$ to site i at a rate given by $r_s C_n^{i+1} (1 - C_n^i)$. The total net flux is therefore

$$\begin{aligned}
 J &= r_s [C_n^i (1 - C_n^{i+1}) - C_n^{i+1} (1 - C_n^i)] \\
 &= r_s (C_n^i - C_n^{i+1}) \\
 &= -D_s \frac{dC_n}{dx}.
 \end{aligned} \tag{5-13}$$

where the last term is in the macroscopic limit. This is identical to the step flow model expression (5-1) in which the adatom terrace diffusion coefficient is given by

$$D_s = a v_0 \exp\left(-\frac{k_1}{k_B T}\right)$$

where a is the atomic separation.

5.3 An asymmetric step flow model

The problem with the symmetric step flow model of Israeli and Kandel, outlined in section 5.1, is that it relies on elastic interaction between steps to drive the evolution by generating a chemical potential difference between steps. As we have seen in Chapter 4, the surface decay rate for the LJ and LJ+BO potentials is quite similar, although the two potentials are very different in some ways. For the LJ+BO potential, the reduced surface lattice spacing does generate an elastic interaction between steps via the surface stress. However, the LJ potential has a uniform lattice spacing and there is no elastic deformation of the body, and hence no elastic interaction between steps. The Israeli and Kandel model predicts that the LJ potential case will not evolve at all, i.e. all the steps have the same chemical potential. This is clearly not the case. In fact, the similarity in decay rates between the LJ and LJ+BO potential models suggests that elastic interaction is not the dominant driving force for step flow. This problem is addressed as follows.

(a) *The model*

Here the symmetric step flow model of section 5.1 is extended to asymmetric steps. In Figure 4.12 and Table 4.1, the attachment and detachment energies are not clearly defined as there are two directions from which an adatom can attach or detach, either to/from the lower terrace or to/from the upper terrace. This model introduces an asymmetry in the step, such that attachment-detachment rate for a step to/from the upper terrace, $k(+1)$, can be different to the attachment-detachment rate for a step to/from the lower terrace, $k(-1)$. Similarly, the equilibrium adatom concentration near a step on the upper terrace, $C_n^{eq}(+1)$, can be different from that on the lower terrace, $C_n^{eq}(-1)$.

The step edge fluxes (5-3) now become dependent on the sign of the steps

$$\begin{aligned} J_n(x_n) &= -k(s_n)[C_n(x_n) - C_n^{eq}(s_n)] \\ J_n(x_{n+1}) &= k(-s_{n+1})[C_n(x_{n+1}) - C_{n+1}^{eq}(-s_{n+1})] \end{aligned}$$

such that, combined with (5-1) and (5-2), the terrace flux of (5-5) is now

$$J_n = \frac{D_s(C_n^{eq}(s_n) - C_{n+1}^{eq}(-s_{n+1}))}{D_s\left(\frac{1}{k(s_n)} + \frac{1}{k(-s_{n+1})}\right) + x_{n+1} - x_n} \quad (5-14)$$

The adatom concentration, $C_n^{eq}(s)$, and attachment-detachment rate, $k(s)$, are defined as before in (5-9) and (5-12) but now the energy barriers used depend on the sign of the argument s such that

$$k_{\text{attach}}(s) = \begin{cases} k_2 & \text{if } s = +1 \\ k_5 & \text{if } s = -1 \end{cases} \quad k_{\text{detach}}(s) = \begin{cases} k_3 & \text{if } s = +1 \\ k_4 & \text{if } s = -1 \end{cases}$$

where the constant k_2 to k_5 are given in Table 4.1 for the LJ and LJ+BO potentials. The adjustment to the ES barrier must be accounted for such that $k_2 \rightarrow k_2 - k_{ES}$ where k_2 is the diffusion barrier for attachment to a step from the upper terrace and k_{ES} is the extra Ehrlich-Schwoebel barrier described in the section 4.4.1 of Chapter 4.

(b) *The step flow parameters*

We write (5-14) as

$$J_n = -\frac{M(s_n, s_{n+1})}{L(s_n, s_{n+1}) + x_{n+1} - x_n} \quad (5-15)$$

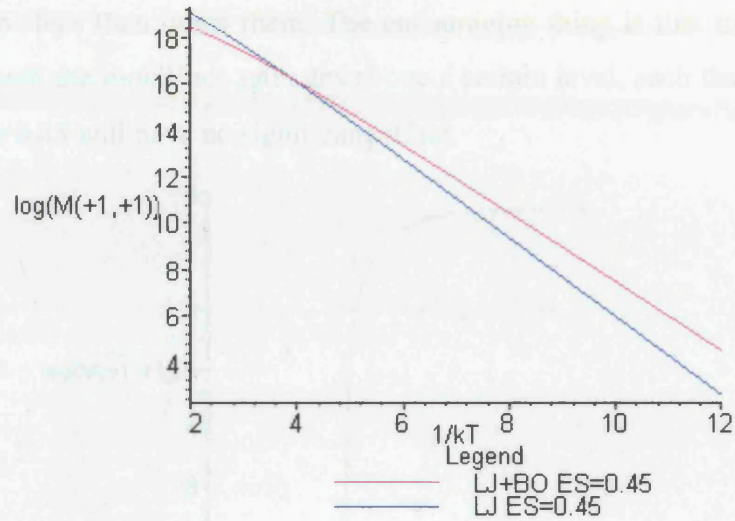
to clearly illustrate that there are two principal temperature-dependent kinetic parameters,

$$M(s_n, s_{n+1}) = D_s (C_{n+1}^{eq}(-s_{n+1}) - C_n^{eq}(s_n)) \quad \text{and} \quad L(s_n, s_{n+1}) = D_s \left(\frac{1}{k(s_n)} + \frac{1}{k(-s_{n+1})} \right),$$

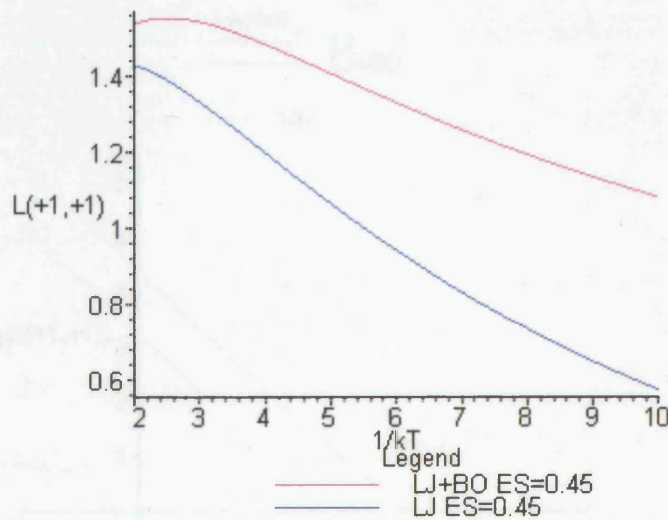
which depend on the nature of the terrace. There are three types of terrace: slope ($s_n = s_{n+1}$), peak (or top) terrace ($s_n = -s_{n+1} = +1$) and trough (or bottom) terrace ($s_n = -s_{n+1} = -1$).

If elastic step interactions are ignored, i.e. $C_n^{eq}(s) = \tilde{C}_n^{eq}(s)$, we see that the flux on the peak and trough terraces is necessarily zero, i.e. $M(+1, -1) = M(-1, +1) = 0$. This renders the characteristic diffusion length for peak and trough terraces, $L(+1, -1)$ and $L(-1, +1)$ ineffective. However, the upper and lower terraces can still evolve without material transport on these terraces. The flux on an downward slope, as shown in Figure 5.5 c, is normally non-zero and is determined by $M(+1, +1)$ and $L(+1, +1)$. The flux on an upward slope is the same but in the opposite direction (as required by symmetry) as $M(-1, -1) = -M(+1, +1)$ and $L(-1, -1) = L(+1, +1)$. These two parameters are plotted in Figure 5.3 for the LJ and LJ+BO potentials, using a (dimensionless) ES correction energy of $k_{ES} = 0.45$ (for the remainder of this chapter we will take $a = \omega_0 = 1$ and non-dimensionalise all times with respect to an attempt frequency of 10^{10} s^{-1}). The first thing to notice is that the overall step mobility, $M(+1, +1)$, is significant which implies that there is a strong asymmetry in the kinetic characteristics of the steps. It increases with temperature as expected, and there is a significant difference between the LJ and LJ+BO potentials (note the log scale) without elastic effects being considered. Secondly, it is interesting to observe that the characteristic diffusion length,

$L(+1,+1)$, increases with temperature (against expectation) and that it is small, typically being less than one or two atomic spacings. We therefore can expect $L(+1,+1) < x_{n+1} - x_n$, which implies, from section 5.2, that diffusion-limited (DL) growth dominates, i.e. diffusion over the terraces is more important than attachment-detachment to/from steps.



(a)



(b)

Figure 5.3 : The characteristic step flow parameters of (5-15) for the LJ and LJ+BO potentials as a function of inverse temperature for an ES adjustment barrier of $k_{ES} = 0.45$: (a) $\ln(M(+1,+1))$ and (b) $L(+1,+1)$.

The effect of the choice of the adjustment to the ES barrier, k_{ES} , is explored in Figure 5.4. The mobility parameter, $M(+1,+1)$, is only positive above a certain value of k_{ES} . One can easily show that the critical conditions for $M(+1,+1) > 0$ is $k_{ES} > k_2 + k_4 - k_3 - k_5$. For the

LJ potential this is -0.11 and for the LJ+BO potential this is about 0.29 . This means that the LJ potential model should exhibit decay even without an adjustment to the ES barrier ($k_{ES} = 0$) but that the LJ+BO potential model will only exhibit decay if $k_{ES} > 0.29$, i.e. for $k_{ES} < 0.29$ a sinusoidal surface profile will grow in amplitude not decay. This is because it is much easier for adatoms to go up steps than down them. The encouraging thing is that the effect of the extra-ES barrier on both the mobilities saturates above a certain level, such that in both cases increasing k_{ES} above 0.45 will have no significant effect.

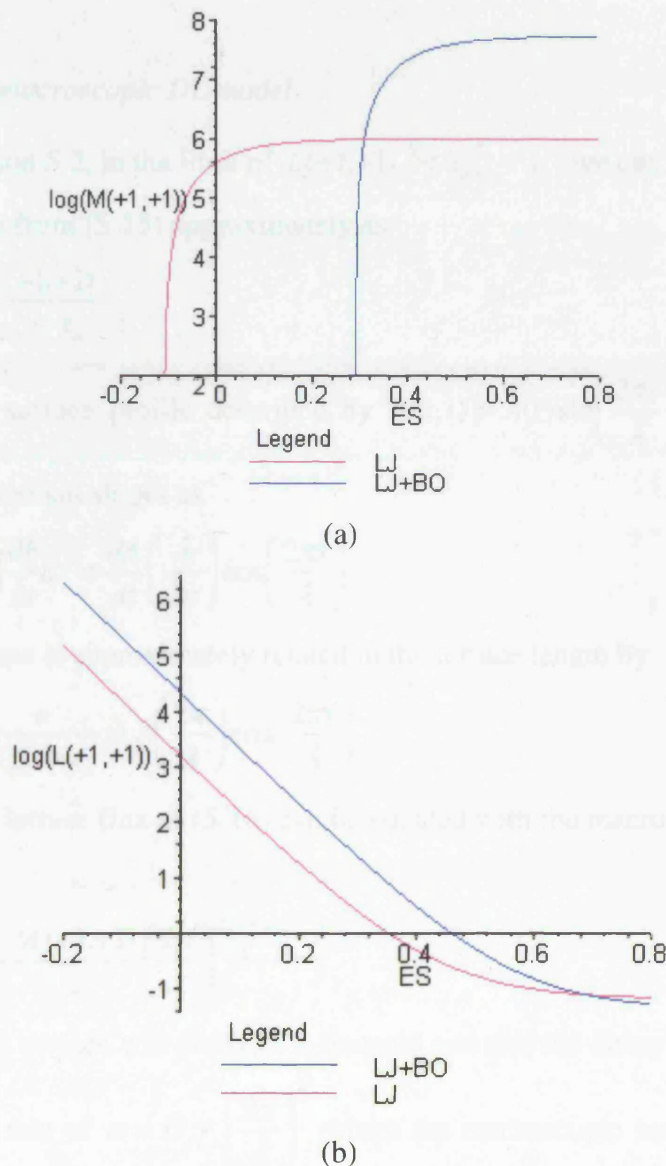


Figure 5.4 : The characteristic step flow parameters of (5-15) for the LJ and LJ+BO potentials as a function of the ES adjustment barrier, k_{ES} , for a temperature of $\bar{T} = 0.1$: (a) $\ln(M(+1,+1))$ and (b) $\ln(L(+1,+1))$.

The diffusion length, $L(+1,+1)$, is also very small for $k_{ES} > 0.45$ so this can also be neglected. However, the diffusion length becomes very large for a low k_{ES} of less than about 0.2. This suggests a cross-over from DL kinetics to ADL kinetics. There is a critical value for k_{ES} above which $L(+1,+1) \rightarrow 0$ as $T \rightarrow 0$ and below which $L(+1,+1) \rightarrow \infty$ as $T \rightarrow 0$. This can easily be shown to be $k_{ES} = k_2 - k_1$ which is 0.317 for the LJ potential and 0.431 for the LJ+BO potential. If the ES barrier is above this value then the kinetics is always DL at low temperatures.

(c) A simple macroscopic DL model

As discussed in section 5.2, in the limit of $L(+1,+1) \ll x_{n+1} - x_n$, we can write the flux on an upward slope terrace from (5-15) approximately as

$$J_n = -\frac{M(+1,+1)}{x_{n+1} - x_n} \quad (5-16)$$

Given a sinusoidal surface profile described by $h(x,t) = A(t) \sin\left(\frac{2\pi x}{\lambda}\right)$, one can write the macroscopic flux for small slopes as

$$J = -\int \frac{\partial h}{\partial t} dx = \frac{dA}{dt} \left(\frac{\lambda}{2\pi}\right) \cos\left(\frac{2\pi x}{\lambda}\right). \quad (5-17)$$

The macroscopic slope is approximately related to the terrace length by

$$\frac{\partial h}{\partial x} = \frac{a}{x_{n+1} - x_n} = A \left(\frac{2\pi}{\lambda}\right) \cos\left(\frac{2\pi x}{\lambda}\right) \quad (5-18)$$

so, using (5-18), the terrace flux of (5-16) can be equated with the macroscopic flux of (5-17) to yield

$$\frac{dA}{dt} = -\frac{M(+1,+1)}{a} \left(\frac{2\pi}{\lambda}\right)^2 A. \quad (5-19)$$

This predicts that the surface will decay as a sinusoid and that the decay is exponential with a characteristic decay rate of $\alpha = D_s \gamma_s \left(\frac{2\pi}{\lambda}\right)^2$ where the macroscopic surface mobility can be equated with the terrace mobility, $D_s \gamma_s = \frac{M(+1,+1)}{a}$. This expression is consistent with the findings from the off-lattice KMC simulations of section 4.5 in that it exhibits a λ^{-2} dependence.

(d) ADL growth

As discussed in section 5.2, in the limit of $L(+1,+1) \gg x_{n+1} - x_n$, we can write the flux on an upward slope terrace from (5-15) approximately as

$$J_n = -\frac{M(+1,+1)}{L(+1,+1)}. \quad (5-20)$$

This means that the flux across each slope terrace is the same (ignoring elastic effects) and is controlled by attachment/detachment to/from steps, i.e. terrace diffusion is very quick. As steps only move due to a flux difference, this means that steps between two slope terraces will not move in pure ADL growth. Only the steps bordering the peak and trough terraces will move, as the flux on the peak and trough terraces is zero. A sinusoidal surface will not decay as a sinusoid. Most of the surface will remain static, whilst the top step moves to remove the top terrace and the bottom step moves at an identical rate in the opposite direction to fill the bottom terrace. Macroscopic material transport is independent of the length of the surface as the flux is constant. Therefore the time to decay will simply depend on the volume of material which needs to be transported, not the distance it needs to be transported. For a given wavelength, this is proportional to the initial amplitude of the surface.

5.4 Elastic interaction from force dipole model

The elastic field around an isolated surface step was investigated in Chapter 3. It was shown that it can be approximated by two force dipoles, d_x and d_z , on an elastic half-plane. Kukta [88] has determined the interaction energy (per unit depth) between two such steps (denoted i and j) as

$$E_{ij} = \frac{C(d_x^2 + s_i s_j d_z^2)}{r_{ij}^2} - \frac{C(s_i - s_j)d_x^2}{\pi} \cdot \frac{h_0}{r_{ij}^3} \left(4 \ln \frac{b}{r_{ij}} + 1 \right), \quad (5-21)$$

where $C = \frac{2(1-\nu^2)}{\pi E}$, $s_k = \pm 1$ defines the orientation of the k th step, $h_0 (\approx a)$ is the step height, b is a structural parameter on the order of step height and $r_{ij} = |x_j - x_i|$ is the distance between the steps. The last term is a higher order correction term for the interaction between steps of opposite sign (as shown in Figure 5.5 a and 5.5b) which is only significant when the steps are close together. For the purposes of this work, this higher order correction term is ignored, for consistency with the Israeli and Kandel symmetric step flow model [55].

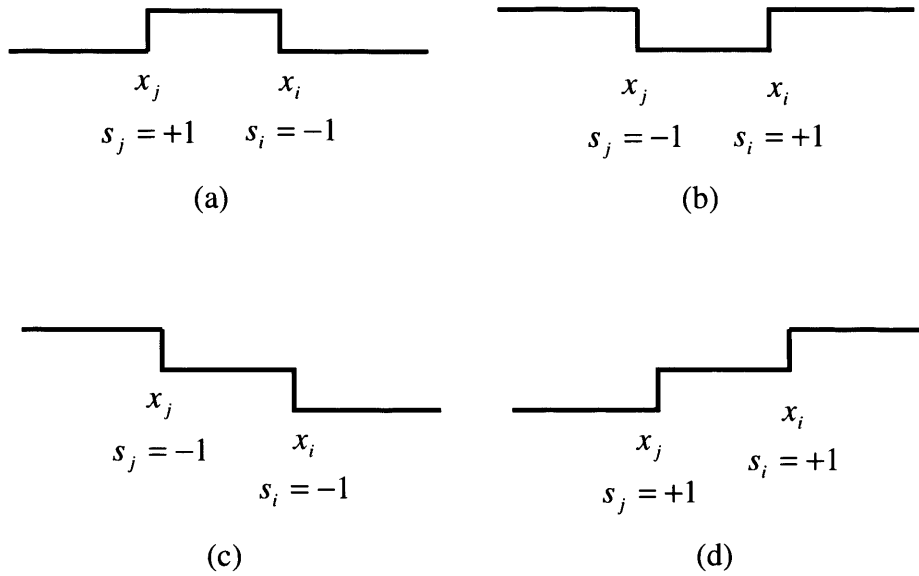


Figure 5.5 : Four different end step configurations for a terrace.

For simplicity, the interaction energy between two similar steps (as shown in Figure 5.5 c and 5.5d) is written as $E_{ij} = \frac{\beta}{2r_{ij}^2}$, where $\beta = 2C(d_x^2 + d_z^2)$. The interaction energy between two

opposite steps (as shown in Figure 5.5 a and 5.5b) is written as $\tilde{E}_{ij} = \frac{\tilde{\beta}}{2r_{ij}^2}$, where $\tilde{\beta} = 2C(d_x^2 - d_z^2)$.

From section 3.2.3, it has been shown that $d_x = 3.93 \frac{\omega_0}{a}$ and $d_z = 2.14 \frac{\omega_0}{a}$ with $C = 0.0079 \frac{a^3}{\omega_0}$ for the LJ+BO potential. Hence $\beta = 0.315\omega_0 a$ and $\tilde{\beta} = 0.171\omega_0 a$. This

implies that similar steps repel each other (the interaction energy is reduced by them moving apart), and that steps of opposite sign also repel each other. This is at odds with conventional models in which steps of opposite sign are usually deemed to attract each other [55]. This helps symmetric step flow models to produce the desired curvature driven decay. However, one typically finds $d_x > d_z$ in material systems [21] which suggests $0 < \tilde{\beta} < \beta$, i.e. steps of opposite sign repel. It also implies that the interaction energy between opposite steps is less significant than that between similar steps.

To investigate sinusoidal decay, the evolution of a sinusoidal waveform is investigated, as shown in Figure 5.6. As the simulation is deterministic, only half a wavelength (containing a peak and a trough) needs to be considered. This consists of a total of N steps. It is assumed that a step only interacts with its two nearest neighbours. The elastic contribution to the chemical potential is therefore

$$\begin{aligned}\mu_1 &= \frac{\partial[-\tilde{E}_{01} + E_{12}]}{\partial x_1} = \frac{\beta}{l_2^3} + \frac{\tilde{\beta}}{l_1^3} \\ \mu_n &= \frac{\partial[E_{(n-1)n} + E_{n(n+1)}]}{\partial x_n} = \frac{\beta}{l_{n+1}^3} - \frac{\beta}{l_n^3}, \quad n = 2, \dots, N-1, \\ \mu_N &= \frac{\partial[E_{(N-1)N} - \tilde{E}_{N(N+1)}]}{\partial x_N} = -\frac{\tilde{\beta}}{l_{N+1}^3} - \frac{\beta}{l_N^3}\end{aligned}\tag{5-22}$$

where $l_n = x_n - x_{n-1}$, $l_1 = 2x_1 + \frac{1}{2}\lambda$ and $l_{N+1} = \frac{1}{2}\lambda - 2x_N$.

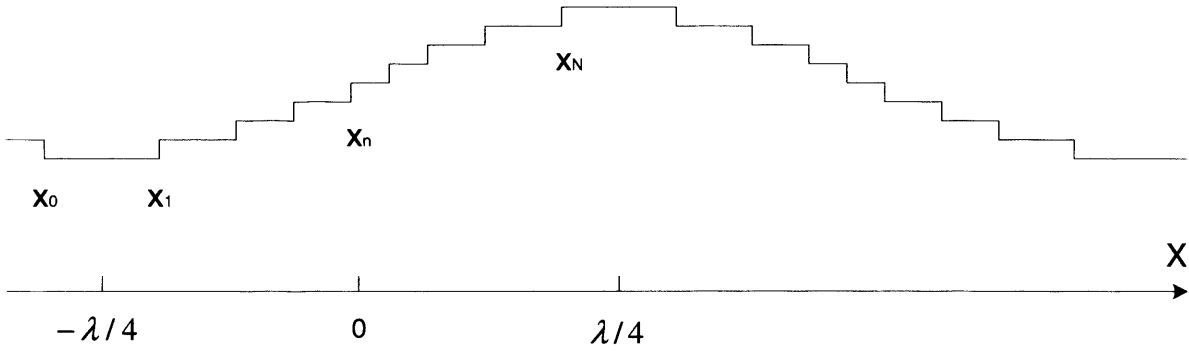


Figure 5.6 : Step labelling for the step flow model of a sinusoidal surface.

5.5 Step flow simulations of the decay of an unstrained sinusoidal surface

The evolution of a surface consisting of discrete surface steps can now be followed using equation (5-6), given the terrace fluxes (5-14) for the asymmetric step flow models, which depend on the step chemical potentials through (5-9) which are given by (5-22). The geometric set-up was described in the previous section. The initial waveform consists of 8 steps generating an approximately sinusoidal profile of amplitude 4. The material constants of section 5.3 are used with an extra-ES barrier of $k_{ES} = 0.45$.

To investigate the decay of the stepped surface, the step density is introduced to describe the profile slope as

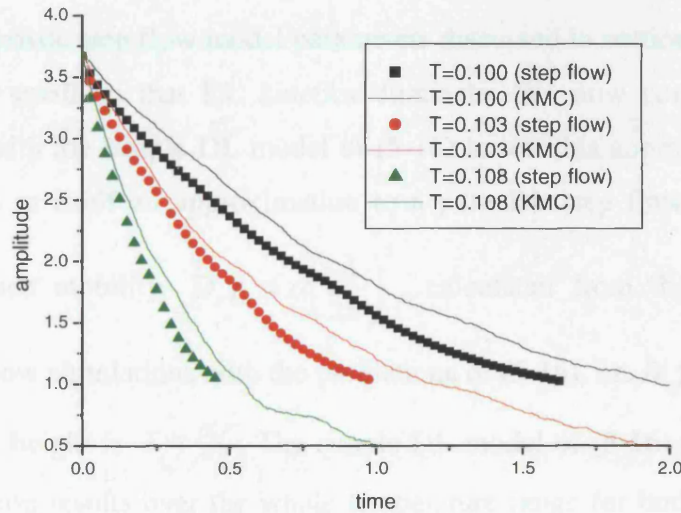
$$D(x, t) = \frac{a}{x_{n+1}(t) - x_n(t)},\tag{5-23}$$

where $x = \frac{x_{n+1} + x_n}{2}$ and a is the height of a step. Israeli and Kandel [55] demonstrate that the decay of the amplitude is approximately

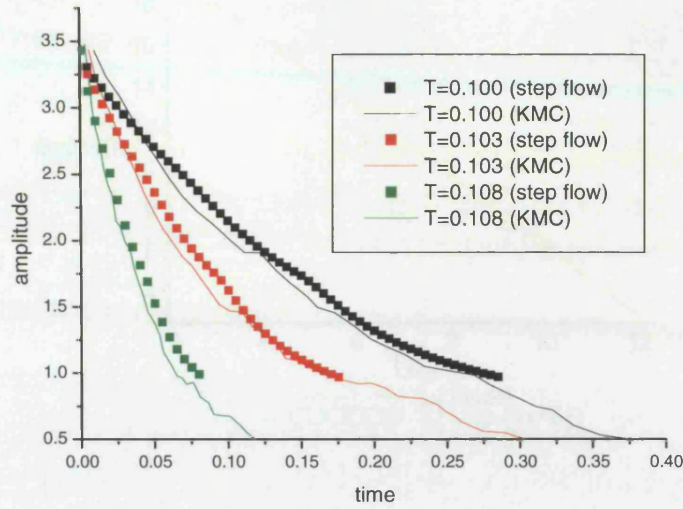
$$A(t) = \max_{\{x\}} D(x, t) \quad (5-24)$$

for DL growth. For strongly ADL growth this is not applicable as the step density only evolves at the peaks and troughs of the surface (see section 5.3d) where the step density is a minimum.

The evolution of the amplitude for the step flow model described is compared in Figure 5.7 with the KMC results of Figure 4.19 and Figure 4.24 for the low temperature regime (where a process consistent with the step flow model is observed). Figure 5.7a shows that the correspondence is very good for long terraces ($N_x=150$), and Figure 5.7b shows that the correspondence is excellent for short terraces ($N_x=61$), which is very encouraging. The step flow model results are not shown for an amplitude less than one as there are only two steps in the system at this point and the amplitude cannot be well approximated.



(a)



(b)

Figure 5.7 : A comparison between the results of the step flow model and off-lattice KMC results for the decay of the amplitude of a sinusoidal surface for the LJ potential and low temperatures and (a) $N_x=150$ and (b) $N_x=61$.

The characteristic step flow model parameters discussed in section 5.3 suggest that the diffusion length is small so that DL kinetics dominate. We now compare the step flow simulation results with the simple DL model of (5-16) to test this approximation (bearing in mind that (5-16) is in itself an approximation to a pure DL step flow model). Figure 5.8 compares the surface mobility, $D_s \gamma_s = \alpha \left(\frac{\lambda}{2\pi} \right)^2$, calculated from the exponential decay curves of the step flow simulations with the predictions of (5-16), i.e. $D_s \gamma_s = \frac{2}{\sqrt{3}} M(+1,+1)$ as the normalised step height is $\bar{a} = \sqrt{3}/2$. The simple DL model of (5-16) is accurate to within 10% of the simulation results over the whole temperature range for both the LJ and LJ+BO potentials and hence is an adequate approximation of step flow under the conditions considered.

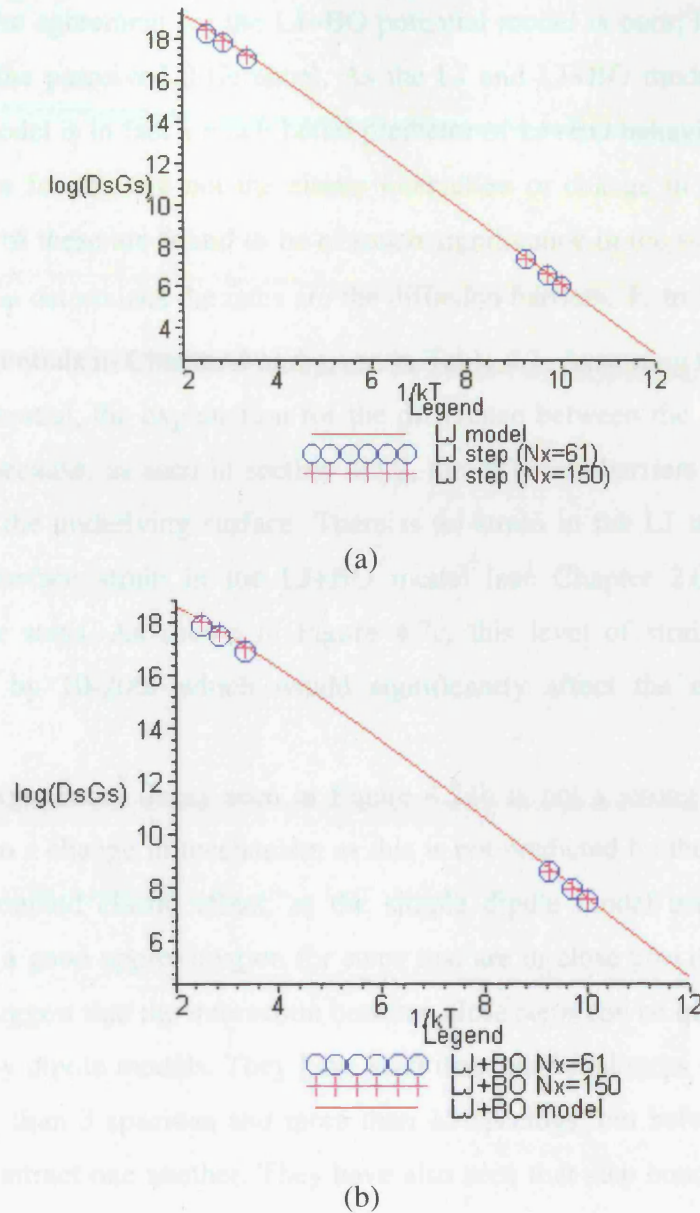
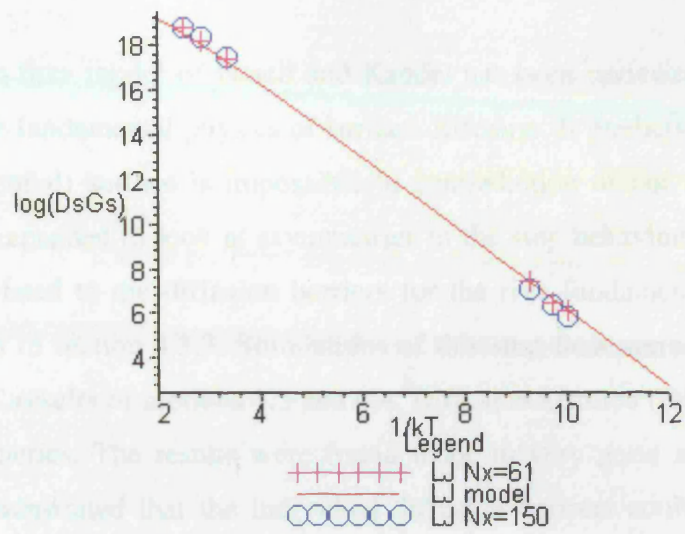


Figure 5.8 : A comparison of the surface mobility, $D_s \gamma_s$, as a function of inverse temperature calculated from step flow simulations and the simple DL model of (5-16) for (a) LJ and (b) LJ+BO potential.

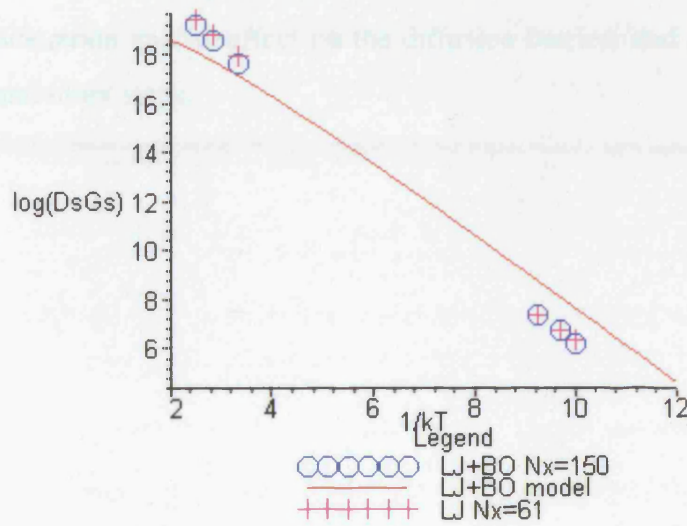
The similar comparison is now made between the off-lattice KMC results for the surface mobility, calculated using $D_s \gamma_s = \alpha \left(\frac{\lambda}{2\pi} \right)^2$, and the simple DL model, calculated from $D_s \gamma_s = \frac{2}{\sqrt{3}} M(+1,+1)$. The results in Figure 5.9 show that the correspondence is very good for the LJ potential over the whole temperature range. This is somewhat surprising as the evolution at high temperatures is rough and does not resemble step flow. The low importance of steps in the representative DL model probably accounts for the good

correspondence. The agreement for the LJ+BO potential model is poor, however (note that a log scale reduces the perceived difference). As the LJ and LJ+BO models are only slightly different, the LJ model is in fact a much better predictor of LJ+BO behaviour than the LJ+BO model. The reasons for this are not the elastic interaction or change in mechanism to ADL growth, as neither of these are found to be of much significance in the step flow simulations. The main factor that determines the rates are the diffusion barriers, k_1 to k_5 , determined from the interatomic potentials in Chapter 4 and given in Table 4.1. Assuming that these are correct for the LJ+BO potential, the explanation for the difference between the KMC and step flow models could be because, as seen in section 4.3.2, the diffusion barriers can be modified by the strain state of the underlying surface. There is no strain in the LJ model, but there is a variation in the surface strain in the LJ+BO model (see Chapter 2.0) due to the close proximity of other steps. As shown in Figure 4.7c, this level of strain could modify the diffusion barriers by 10-20% which would significantly affect the macroscopic surface mobility.

The non-exponential decay seen in Figure 4.24b is not a strong effect and hence is probably not due to a change in mechanism as this is not predicted by the step flow model. It may be an unaccounted elastic effect, as the simple dipole model used in the step flow simulations is not a good approximation for steps that are in close proximity to one another. Kukta et al. [88] suggest that the interaction between close steps can be quite complex and not well-represented by dipole models. They have seen that individual steps can repel each other at separations less than 3 spacings and more than 15 spacings, but between at intermediate spacings they can attract one another. They have also seen that step bunches can behave in a collective manner which is different to that of individual steps.



(a)



(b)

Figure 5.9 : A comparison of the surface mobility, $D_s \gamma_s$, as a function of inverse temperature calculated from the off-lattice KMC simulations of section 4.4 and the simple DL model of (5-20) for (a) LJ and (b) LJ+BO potential.

5.6 Summary

The symmetric step flow model of Israeli and Kandel has been reviewed and is found to be lacking some of the fundamental physics of surface diffusion. It predicts that flattening of an unstrained (LJ potential) surface is impossible in contradiction of our findings. The model was consequently expanded to look at asymmetries in the step behaviour. The parameters in this model were related to the diffusion barriers for the five fundamental surface diffusion processes identified in section 4.3.3. Simulations of this step flow were then compared with the off-lattice KMC results of sections 4.3 and 4.4. Diffusion Limited (DL) growth was found to dominate the kinetics. The results were found to be in very good agreement for the LJ potential. This demonstrated that the individual diffusion barriers could be assembled in a non-trivial way to correctly predict the macroscopic surface mobility. The results were not in good agreement for the LJ+BO potential. This is assumed to be due to the additional complexity of surface strain and its effect on the diffusion barriers and interactions between steps and adatoms and other steps.

6.0 Diffusion on strained surfaces

6.1 Morphological change

As introduced in section 1.1.4, heteroepitaxial semiconductor thin films are the main materials for fabricating microelectronic and optoelectronic devices. The possibility of creating self-organised nanostructures through this route has been of great interest [101]. This requires control of the strain-induced morphological change in these systems. This roughening of a strained surface has been widely investigated using the Azaro-Tiller-Grinfeld (ATG) instability theory [1][2]. This shows that the initially flat surface of a strained film is unstable for an isotropic surface energy. Reduction in the elastic stored energy of the thin film drives the roughening towards the shortest possible wavelength. Meanwhile surface energy wishes to flatten the perturbed surface and drive the system to the longest possible wavelength. This competition between the elastic stored energy and surface energy favours the formation of a particular roughening wavelength, as shown in Figure 6.1. As the surface continues to roughen (beyond a small perturbation) cusp-like valleys form with a singular stress concentration near the cusp tip [4]. Such high stress concentrations provide preferential locations for the nucleation of dislocations, another strain energy reduction mechanism.

In this chapter, the stability of a strained surface is first investigated using a novel small perturbation continuum theory for anisotropic surfaces. In the subsequent section, off-lattice KMC simulations are performed to investigate the roughening of a strained surface for various strains. The results of these predictions are then compared with the continuum theory. Finally, off-lattice KMC simulations are then used to investigate the roughening of surfaces in the non-linear large perturbation regime.

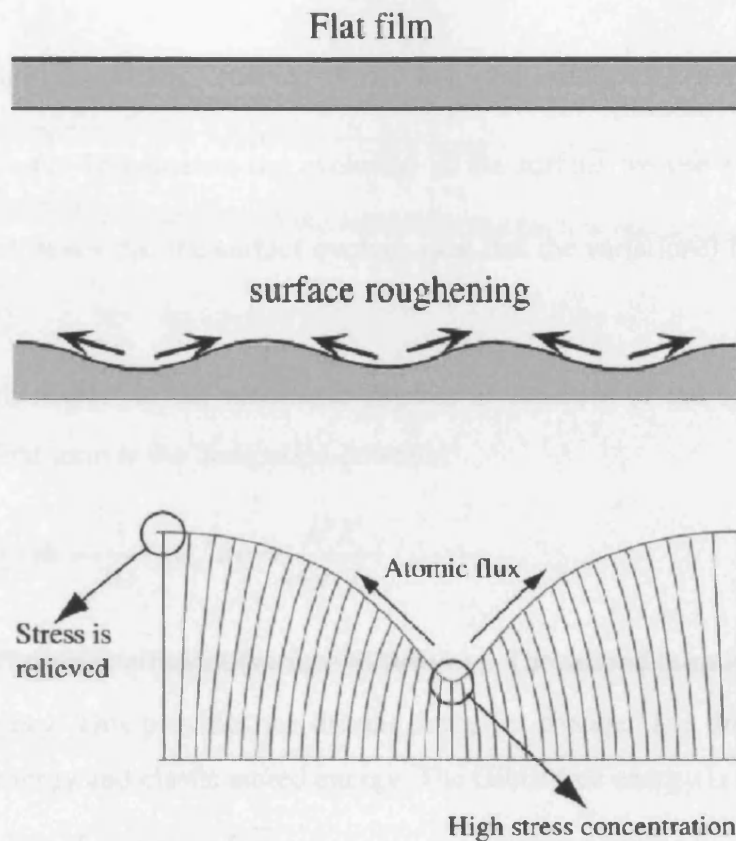


Figure 6.1 : Morphological change (roughening) of a strained surface is induced by a reduction in the elastic strain energy [4].

6.2 Stability of strained surfaces

6.2.1 Continuum theory

A sinusoidal surface profile is chosen to investigate the evolution of a strained surface. The height of the surface is $h(x, t) = A(t) \cos\left(\frac{2\pi}{\lambda} x\right)$, where λ is the wavelength of the sinusoidal perturbation and $A(t)$ is the amplitude of the perturbation at time t . Assuming that the perturbation slope is always small (i.e. $A \ll \lambda$) the normal velocity of the surface is given by

$$v_n \approx \frac{dh}{dt} = \dot{A} \cos\left(\frac{2\pi}{\lambda} x\right),$$

where the dot indicates differentiation with respect to time. Mass

conservation gives

$$\frac{\partial J_s}{\partial s} + v_n = 0 \quad , \quad (6-1)$$

where J_s is the volumetric surface flux. For the sinusoidal surface morphology,

$$J_s = -\frac{\dot{A}\lambda}{2\pi} \sin\left(\frac{2\pi}{\lambda}x\right).$$

To calculate the evolution of the surface we use a kinetic variational principle [5] which states that the surface evolves such that the variational functional

$$\Pi = \Psi + \dot{G} \quad (6-2)$$

is minimised with respect to the kinematic degrees of freedom of the system (in this case simply \dot{A}). The first term is the dissipation potential

$$\Psi = \frac{1}{2} \int_s \frac{J_s^2}{D_s} ds \approx \frac{1}{2D_s} \int_0^\lambda J_s^2 dx = \frac{\dot{A}^2 \lambda^3}{16\pi^2 D_s}, \quad (6-3)$$

where D_s is a diffusion coefficient (surface diffusivity). The second term is the rate of change of Gibbs free energy. This provides the driving force for change. The driving forces in this case are surface energy and elastic stored energy. The Gibbs free energy is therefore

$$G = G_s + G_e = \int_s \gamma_s(\theta) ds + \int_v w dV, \quad (6-4)$$

where γ_s is the surface energy per unit area (which might be a function of the surface orientation θ) and w is the elastic stored energy per unit volume.

The surface energy contribution can be written as

$$G_s = \int_0^\lambda \gamma_s(\theta) \sqrt{1 + \left(\frac{dh}{dx}\right)^2} dx \approx \int_0^\lambda \gamma_s(\theta) (1 + \frac{1}{2}\theta^2) dx$$

where the final expression is in the limit of small slopes, in which case $\theta \approx \frac{dh}{dx}$. To make

analytical progress we expand the surface energy function around the flat surface orientation (taken to be $\theta = 0$) up to second order

$$\gamma_s(\theta) = \gamma_0 + \gamma_1|\theta| + \frac{1}{2}\gamma_2\theta^2. \quad (6-5)$$

where the γ_i are constants. The absolute value of the linear term, $|\theta|$, is taken to satisfy the symmetry requirement that $\gamma_s(-\theta) = \gamma_s(\theta)$. This term produces a cusp (discontinuity in the derivative of the surface energy function) at $\theta = 0$ (see Figure 1.12c). The novelty of this

model is to include the effect of this cusp in the surface energy. The existence of such a cusp is well supported by the simplified analysis for the surface energy density of an unrelaxed, unstrained surface given in appendix F. Therefore, to second order, the surface energy contribution per wavelength is

$$\dot{G}_s = \left(4\gamma_1 + 2\pi^2(\gamma_0 + \gamma_2) \frac{A}{\lambda} \right) \dot{A}.$$

The elastic strain energy, $w(x)$, at a point, x , on the surface of a film with a slightly undulating surface varies from the strain energy of an unperturbed film, $w_0 = \frac{1}{2} p E \epsilon_0^2$, by a small amount, where ϵ_0 is the mismatch strain and $p = 1$ for plane stress and $p = (1 - \nu^2)^{-1}$ for plane strain conditions. This perturbation to the elastic field can be represented by imposing a continuous distribution of infinitesimal point forces over the surface [35]. In this case

$$w(x) = w_0 \left[1 - \frac{4}{\pi} \int_{-\infty}^{\infty} \frac{\frac{dh(\zeta)}{d\zeta} d\zeta}{(x - \zeta)} \right] = w_0 \left[1 - \frac{8A\pi}{\lambda} \cos\left(\frac{2\pi}{\lambda}x\right) \right], \quad (6-6)$$

where ζ is the surface location of a given point force. The rate of change of the elastic strain energy per wavelength is

$$\dot{G}_e = \int_s w v_n ds = \int_0^\lambda w(x) v_n(x) dx = -4\pi w_0 A \dot{A}$$

which predicts that the strain energy in the film is always reduced by roughening and that this is independent of the roughening wavelength.

The variational function of (6-2) is therefore

$$\Pi = \frac{\dot{A}^2 \lambda^3}{16\pi^2 D_s} + \left(4\gamma_1 + 2\pi^2 \hat{\gamma} \frac{A}{\lambda} - 4\pi w_0 A \right) \dot{A}, \quad (6-7)$$

where the surface stiffness parameter, $\hat{\gamma} = \gamma_s(0) + \frac{\partial^2 \gamma_s}{\partial \theta^2} \Big|_{\theta=0} = \gamma_0 + \gamma_2$, has been introduced.

This is minimised when $\frac{\partial \Pi}{\partial \dot{A}} = 0$, so

$$\dot{A} = \frac{8\pi^2 D_s}{\lambda^3} \left(2\pi \left(2w_0 - \frac{\pi\hat{\gamma}}{\lambda} \right) A - 4\gamma_1 \right).$$

Integration with respect to time gives the evolution equation for the surface profile as

$$A(t) = (A_0 - B_0) \exp(t/\tau) + B_0 \quad (6-8)$$

where $\tau = \frac{\lambda^4}{16\pi^3 D_s (2w_0\lambda - \pi\hat{\gamma})}$ is the characteristic roughening time, A_0 is the amplitude at

time $t=0$, and $B_0 = \frac{2\gamma_1\lambda}{\pi(2w_0\lambda - \hat{\gamma}\pi)}$. The fastest growing wavelength, λ_m , is the wavelength

that is expected to be physically observed. This maximises the growth rate \dot{A} such that

$\frac{d}{d\lambda} \left[\frac{(A_0 - B_0)}{\tau} \right] = 0$ and is given by

$$\lambda_m = \frac{2\pi\hat{\gamma}}{3(w_0 - w_c)} \quad (6-9)$$

where $w_c = \frac{\gamma_1}{\pi A_0}$ is a critical strain energy density. No growth is predicted to occur for strain

energy densities below the critical strain energy density. The optimum growth rate at the

optimal wavelength is $\frac{(A_0 - B_0)}{\tau} = \frac{27D_s(w_0 - w_c)^2 A_0}{\hat{\gamma}^3}$. Note that the optimal growth rate is

independent of the kinetic model, i.e. the alternative kinetic model of section 5.3c would also predict the result of (6-9), although the growth rate would be different.

Equation (6-9) is a novel result because it shows that a cusp in the surface energy can stabilise a thin film against roughening. If there is no cusp ($\gamma_1 = 0$) then the critical strain energy for roughening is zero and the surface is always unstable. In this case the classical ATG result [1][2] is reproduced, i.e. $\lambda_m = \frac{2\pi\hat{\gamma}}{3w_0}$. If the surface energy is cusped the critical

strain energy density is inversely proportional to the initial amplitude, A_0 , indicating that the surface is only stable to perturbations below a certain size. Typically one might consider the initial perturbation to be the height of an atomic step such that $A_0 = \sqrt{3}/2 a_0$.

6.2.2 Roughness parameters

In nature most surfaces are rough rather than smooth, especially at a very small scale. Roughness parameters need to be extracted or estimated statistically to characterise the roughness of a surface. Many roughness parameters exist [94] such as the average surface height, the root-mean-square (RMS) roughness, the skewness & the kurtosis, the auto-correlation function, the height-height correlation function and the power spectrum. A few of these are useful in the analysis of surfaces with a periodic roughness and these are introduced here.

(a) RMS roughness

The RMS roughness is also known as the interface width, ω . It is one of the most important parameters to characterise a rough surface and is defined for our discrete atomic surface as

$$\langle \omega \rangle_N = \left[\frac{1}{N} \sum_{i=1}^N (h_i - \langle h \rangle_N)^2 \right]^{1/2} \quad (6-10)$$

where $\langle h \rangle_N = \frac{1}{N} \sum_{i=1}^N h_i$ is the (constant) mean surface height.

(b) Height-height correlation function

Sometimes very different rough surfaces have the same RMS roughness. This is because the frequencies of the height fluctuations are different. A connection between two heights in different positions needs to be constructed. The height-height correlation function provides this information and is defined as

$$\langle H(m) \rangle_N = \frac{1}{N-m} \sum_{i=1}^{N-m} (h_{i+m} - h_i)^2, \quad (6-11)$$

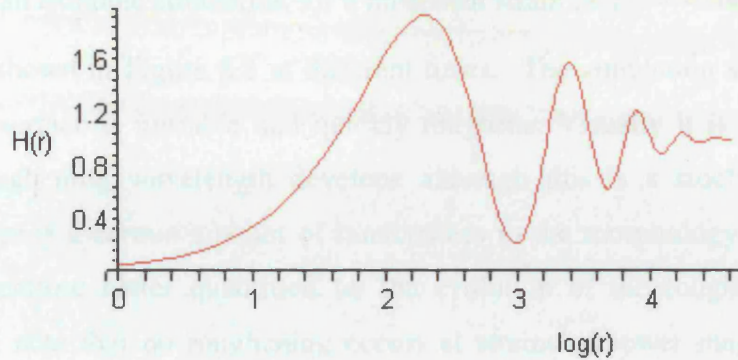
where m is the distance between two heights in different positions. Note that the height-height correlation function is not accurate for large m values as the number of data points is small.

In the analysis of mounded surfaces, Zhao et al. [95][96] proposed that the height-height correlation function has the following form

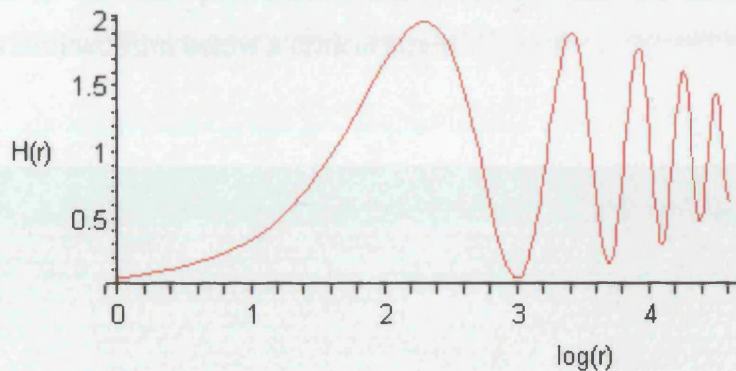
$$H(r) = 2\omega^2 \left[1 - \exp\left(-\left(r/\zeta\right)^{2\alpha}\right) \cos(2\pi r/\lambda) \right], \quad (6-12)$$

where ζ is the system correlation length, λ is the average mound separation and α is the roughness exponent ($0 \leq \alpha \leq 1$). This describes how wiggly the surface is. For example, $\alpha = 0.7$ corresponds to a locally smooth surface structure while $\alpha = 0.3$ corresponds to a

more jagged local surface morphology. The expected form of this function is plotted in Figure 6.2 for a small and a large system correlation length.



(a)



(b)

Figure 6.2 : The height-height correlation function for $\alpha = 1$ and $\lambda = 20$ for a correlation length that is (a) small (40) and (b) large (100). The distance between the first two peaks is the most accurate estimate of the mound separation.

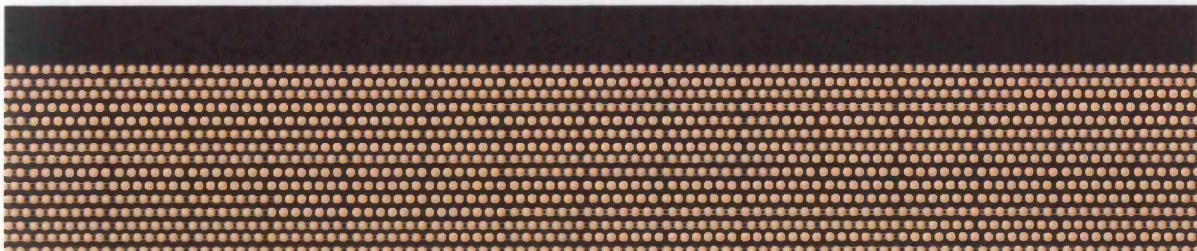
6.2.3 Off-lattice KMC simulation

The off-lattice KMC model of chapter 5 is naturally suitable for investigating the evolution of strained surfaces. The atoms can relax to find the global minimum elastic energy configuration and the effect of strain on the activation energy for surface diffusion is fully accounted for. A lattice block of 100×30 atoms was chosen with an initially flat surface. The atoms of the two bottom layers were fixed so as to apply a uniform mismatch strain. Periodic

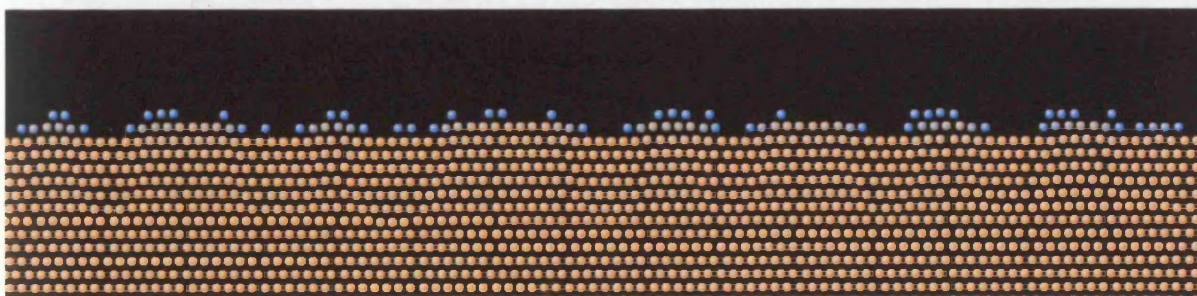
boundary conditions were used on the vertical sides of the sample. All other atoms are free to move in any way. Simulations were performed using the LJ and LJ+BO potentials.

(a) Roughening of an LJ surface

Snapshots of an example simulation for a mismatch strain of $\epsilon_x = -0.06$ and a temperature of $\bar{T} = 0.5$ are shown in Figure 6.3 at different times. The simulation shows that the initially flat strained surface is unstable and quickly roughens. Visually it is possible to see that a particular roughening wavelength develops although this is a stochastic process and, as expected, there is a certain amount of randomness to the morphology. The evolution of the surface is therefore better quantified by the evolution of the roughness parameters. It is interesting to note that no roughening occurs at strains of lower magnitude. The expected wavelength is approaching the order of the system size which may be a factor, but the surface would still be expected to roughen at a wavelength below the optimum value. This supports the predictions of the small perturbation theory of (6-9) that the anisotropic surface energy can stabilise a strained film below a critical strain.



(a) N=0



(b) N=500

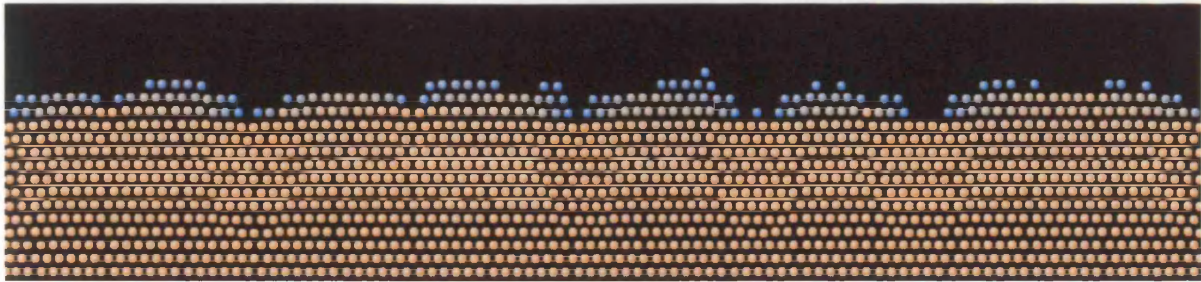
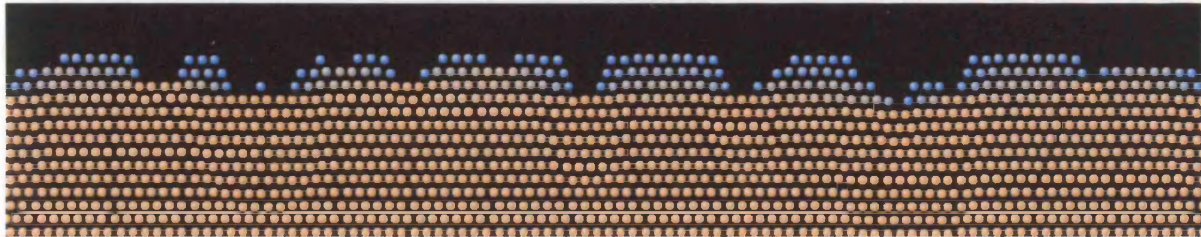
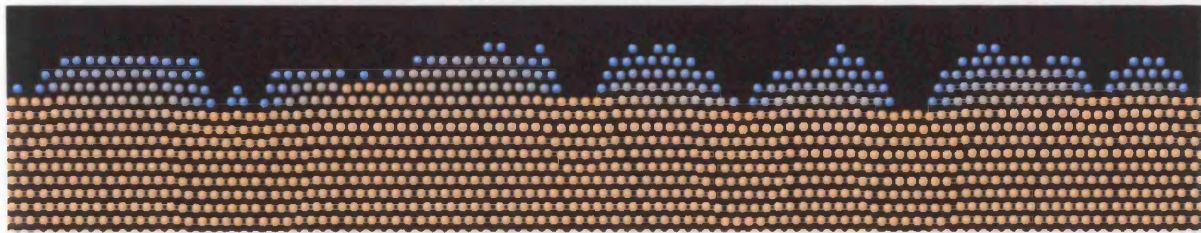
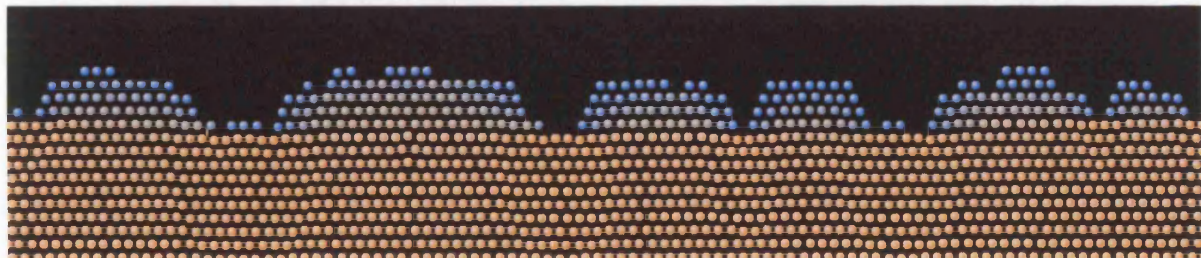
(c) $N=5,000$ (d) $N=10,000$ (e) $N=20,000$ (f) $N=75,000$

Figure 6.3 : Snapshots of an off-lattice KMC simulation of the roughening of an LJ surface subject to a mismatch strain of $\epsilon_x = -0.06$. N is the number of atomic jumps performed to achieve the structure shown. Note that only part of the bulk region is shown. The colours indicate the strain energy of each atom where blue indicates low strain energy and red indicates high.

The RMS roughness is shown in Figure 6.4 as a function of time for a range of off-lattice KMC simulations at different compressive mismatch strains. The roughness is initially zero as the surface is flat. It increases rapidly at first and then proceeds to grow more slowly over

time. Small perturbation theory predicts that the initial growth rate of the roughness (amplitude) will be exponential. This happens so rapidly at the beginning that it is difficult to observe. The second slower growth phase must therefore be due to large perturbation effects. This is expected as the roughness cannot continue to grow indefinitely (at a particular wavelength). It is of interest to note that the surfaces roughen more quickly at smaller strains ($\epsilon_x = -0.06$) and less quickly at large strains ($\epsilon_x = -0.08$). At first sight this is not expected

as the characteristic growth rate (from section 6.2.1) is $\frac{27D_s(w_0 - w_c)^2 A_0}{\hat{\gamma}^3}$. This predicts that

an increase in strain energy should increase the growth rate. However, the surface diffusivity is also strongly dependent on strain. This result indicates that the evolution occurs more slowly on a highly compressed surface. Also, this result applies to the initial rapid growth stage rather than the slower growth stage of the developed mounds.

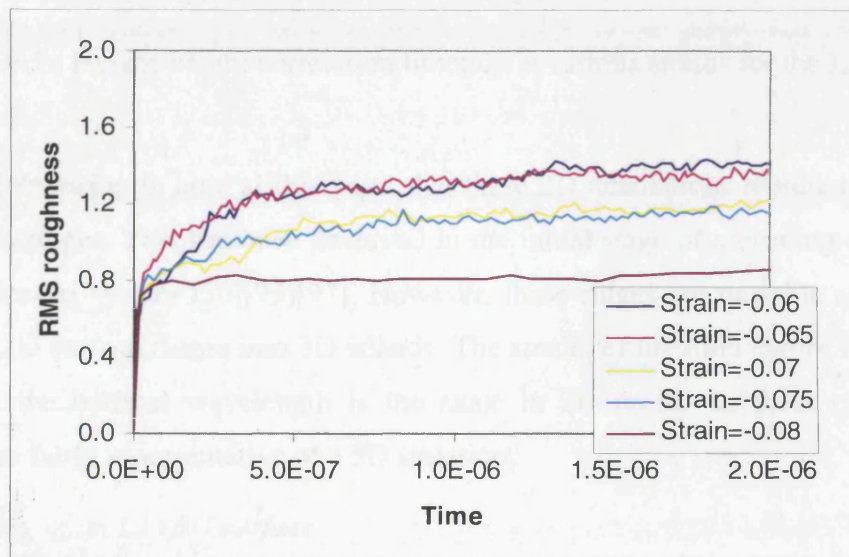


Figure 6.4 : RMS roughness for various strains for the LJ surface

The height-height correlation functions for various strains are plotted in Figure 6.5. They are all similar to the example height-height correlation function in Figure 6.2b indicating that the system correlation length is large compared to the mound separation. This indicates a strong driving force for global organisation of the structure. However, the correlation length is of the order of the system size so it is also probably an artefact of the small system size and periodic boundary conditions. As stated in section 6.2.2b, the average mound separation λ can be extracted from the distance between the first two peaks of the height-height correlation

functions. This is a much more accurate and representative means of determining the wavelength than a simple visual inspection of the surface.

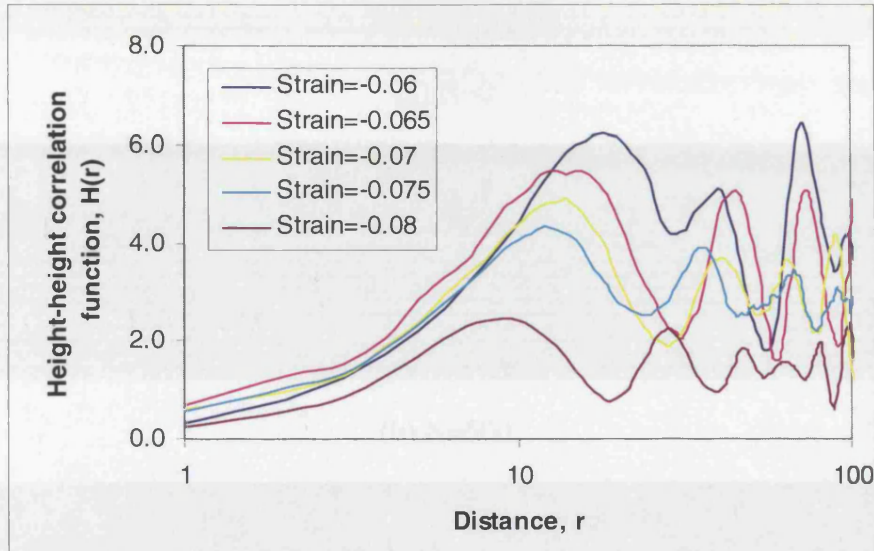
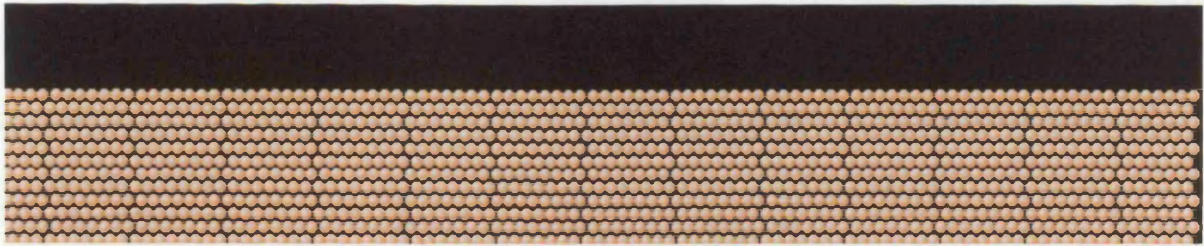


Figure 6.5 : Height-height correlation function at various strains for the LJ surface

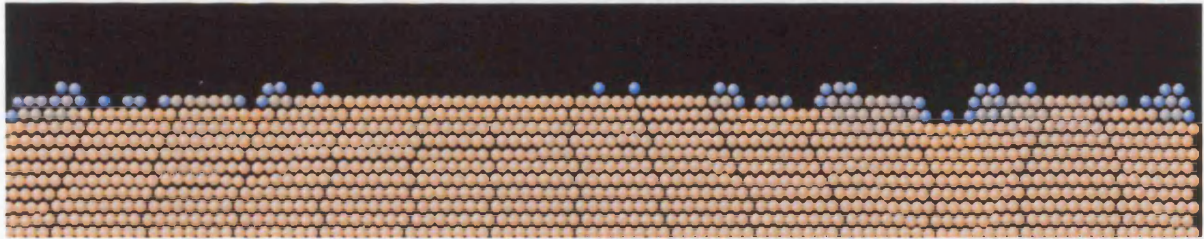
It is interesting to note at this point that these 2D simulations represent the evolution of 2D surface ridges. This has been observed in the initial stage of annealing experiments of the heteroepitaxial system [50][93][97]. However, these ridges are unstable and a transition occurs from 2D surface ridges into 3D islands. The small perturbation theory in section 6.2.1 predicts that the optimal wavelength is the same in 2D or 3D so these calculations are expected to be fairly representative of a 3D situation.

(b) Roughening of an LJ+BO surface

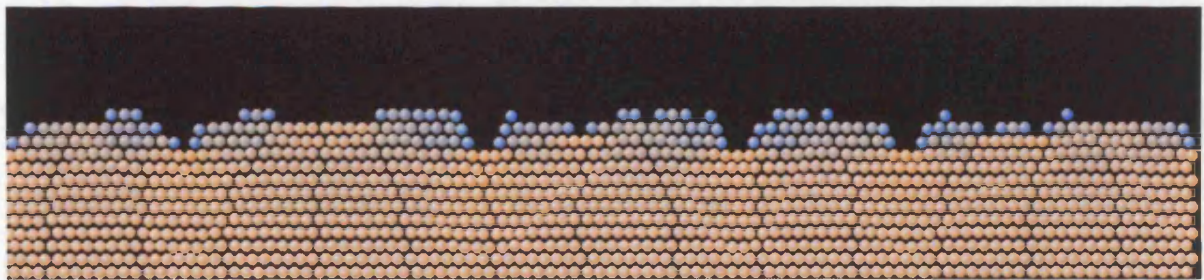
The effects of surface stress on the roughening of a strained surface are now considered with the introduction of the bond order term. The simulation conditions are identical to those used for the LJ potential in the previous subsection. The evolution of a surface subject to a mismatch strain of $\epsilon_x = -0.06$ is shown in Figure 6.6. The relaxation process is very similar to that of an LJ surface seen in Figure 6.3, although the initial evolution of the roughness in Figure 6.6b is not as uniform as that in Figure 6.3b. The most obvious difference between them is the chosen roughening wavelength. The wavelength for LJ+BO is longer than that for LJ as the surface stress tends to flatten the perturbed surface.



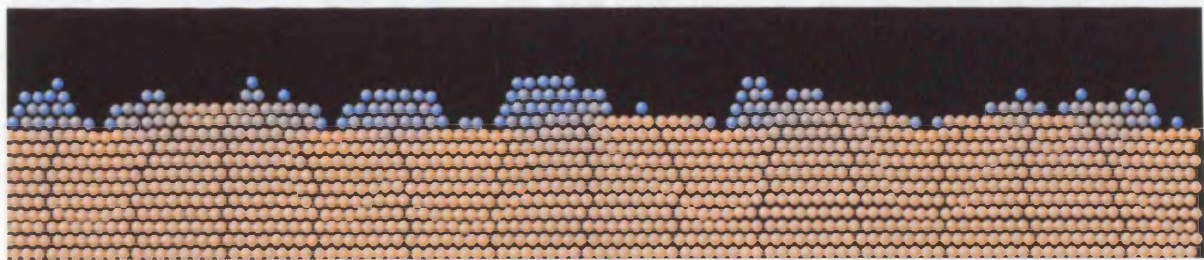
(a) $N=0$



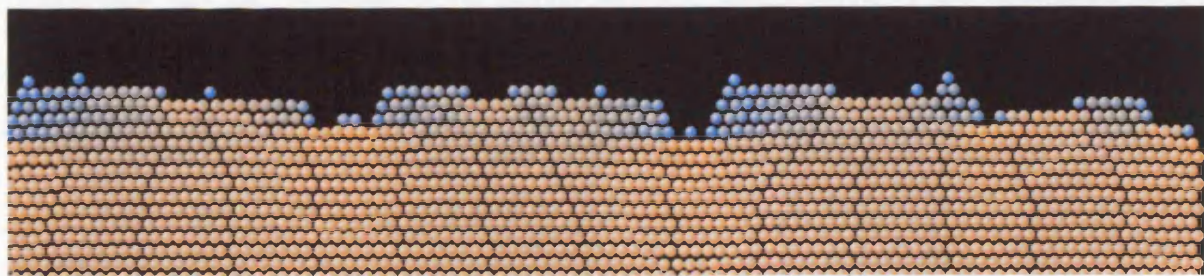
(b) $N=500$



(c) $N=5,000$



(d) $N=10,000$



(e) $N=20,000$

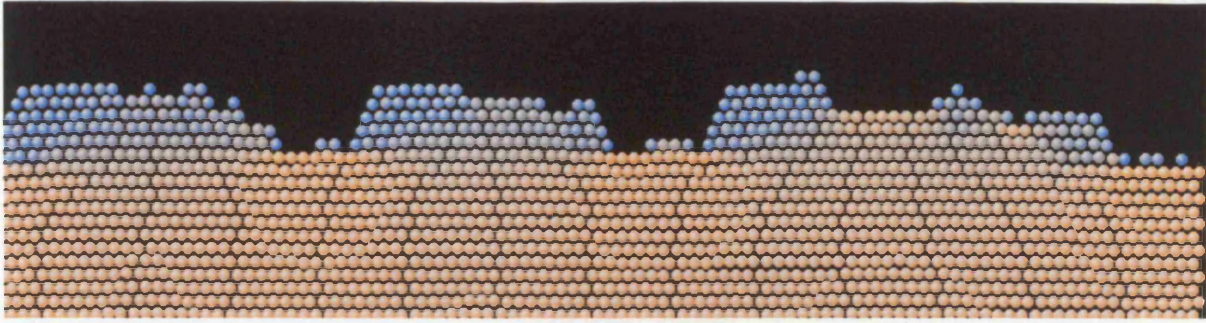
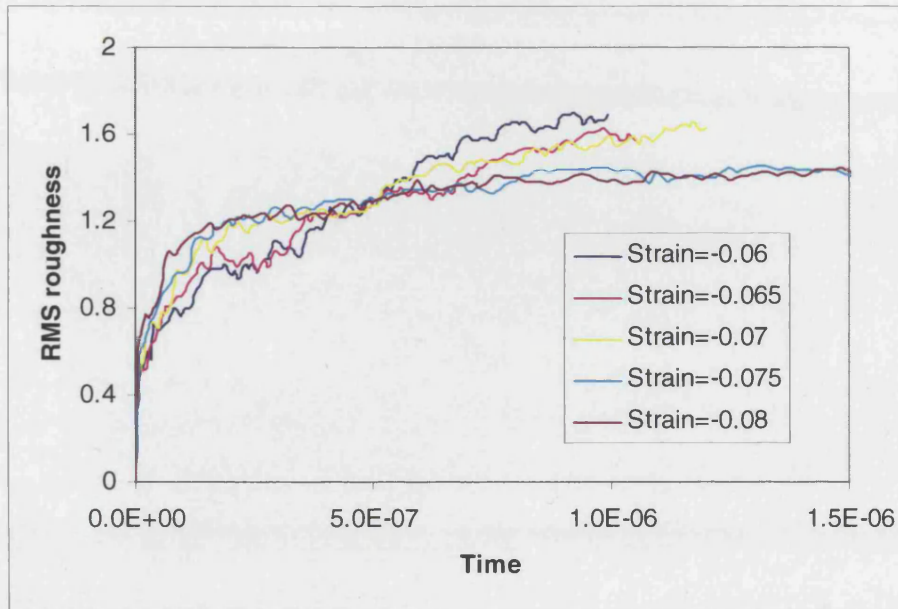
(f) $N=56,500$

Figure 6.6 : Roughening of a strained LJ+BO surface for a mismatch strain of $\epsilon_x = -0.06$ using an off-lattice KMC simulation.

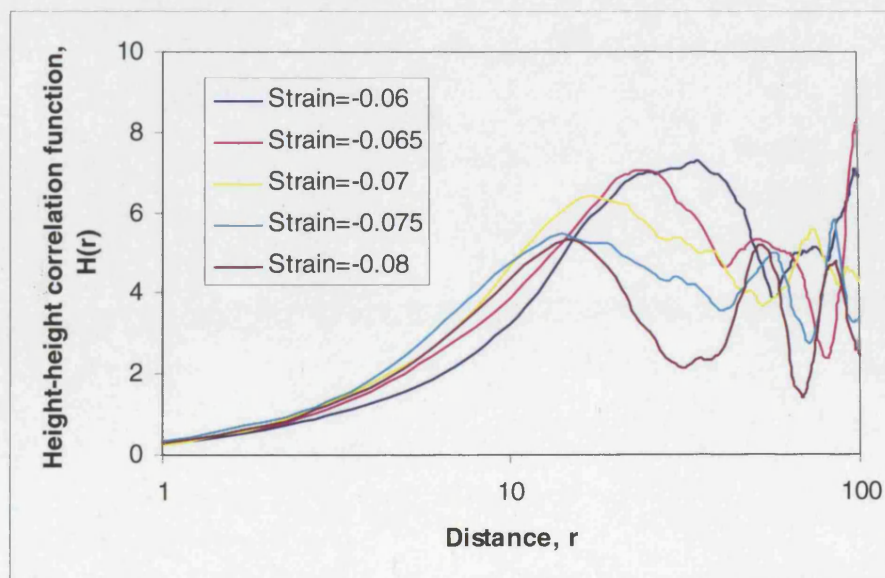
As before, the roughness parameters for these simulations at various strains have been calculated and are shown in Figure 6.7. Comparison between the LJ and LJ+BO RMS roughness evolution in Figure 6.4 and Figure 6.7a immediately shows a difference that is not readily observed by visual inspection. They are similar in the sense that they both undergo a very rapid roughening in the initial stages and that the final roughness of the large strain simulations ($\epsilon_x = -0.08$) is smaller than that of the smaller strain ones ($\epsilon_x = -0.06$). However, the large strain simulations roughen more quickly at the beginning for the LJ+BO surface which is not the case for the LJ surface. The final roughness of the LJ+BO surface is also much larger over a similar time scale. One explanation for this is that the surface strain in the LJ+BO simulation is lower than that in the LJ simulation. Recall from section 2.4.1 that the surface stress of (2.28) is minimised when $\epsilon_x = -0.026$. This means that the surface strain energy will be lowered by the bond-order terms when the surface is in a state of compression near this value. It was seen for the LJ surface that the smaller strain values ($\epsilon_x = -0.06$) produced a surface which roughened more quickly than the more highly strained surfaces. It is expected that the reduction in the surface strain in compression by the bond-order terms means that the LJ+BO surface behaves a bit like an LJ surface at a mismatch strain of reduced magnitude. This is consistent with the RMS roughness results. One point of interest about the LJ+BO surface is that the thermodynamics in tension are expected to be different from that in compression. This could be an explanation for some results of Gao and Nix [4] who observed different behaviour between Ge on Si (compression) and Si on Ge (tension).

The height-height correlation results in Figure 6.7b are similar to the example in Figure 6.2a possibly indicating a lower system correlation length. The second peak is less

well defined so the roughening wavelength is not as accurately measured. This is partly due to the longer wavelengths in the LJ+BO systems (again consistent with a lower strain) which in some cases are approaching the system size.



(a)



(b)

Figure 6.7 : Roughness parameters from off-lattice KMC simulation for the LJ+BO surface at various mismatch strains. (a) RMS roughness and (b) height-height correlation function.

(c) Comparison between the roughening wavelength of the LJ and LJ+BO surfaces

The wavelengths obtained from the height-height correlation plots in Figure 6.5 and Figure 6.7b for the roughening of the LJ and LJ+BO surfaces respectively are shown as a function of mismatch strain in Figure 6.8. From (6-9) the wavelength is expected to vary as

$$\lambda_m = \frac{4\pi\hat{\gamma}}{3E(\varepsilon^2 - \varepsilon_c^2)}$$

where the non-dimensionalised Young's modulus, E , is 72 (see section 2.2) and ε_c is a critical strain below which no roughening occurs. Two curves of this form are fitted to the data and are shown in Figure 6.8. The fit is clearly very good. For the LJ surface the fitting parameters are $\hat{\gamma} = 1$ and $\varepsilon_c = 0.028$. For the LJ+BO surface they are $\hat{\gamma} = 1.4$ and $\varepsilon_c = 0.028$. The critical strain for each is the same. Given that ε_c^2 is proportional to the strength of the surface energy cusp, γ_1 , this is not surprising as the unstrained surface energy density models of (F-1) and (F-2) predict similar values for this parameter, with $\gamma_1 = 0.577$ and $\gamma_1 = 0.558$ for the LJ and LJ+BO surfaces respectively. However, both models predict that $\hat{\gamma} = 0$ which implies that the optimal roughening wavelength is zero. This is clearly not the case. The difference could be for two reasons.

Predictions for the surface stiffness, $\hat{\gamma} = \gamma_s(0) + \left. \frac{\partial^2 \gamma_s}{\partial \theta^2} \right|_{\theta=0}$, are very sensitive as the second

derivative can be an order of magnitude larger than the surface energy density and can change rapidly given small changes in the surface energy model. Also, the surface energy density models are for unrelaxed, unstrained surfaces. It is expected that the surface parameters will be heavily modified by the effects of strain, including step relaxation and step-step interactions, which are ignored in Appendix F. The difference between the two models can be simply stated: the LJ+BO wavelength is 40% larger than that of its LJ counterpart at the same strain.

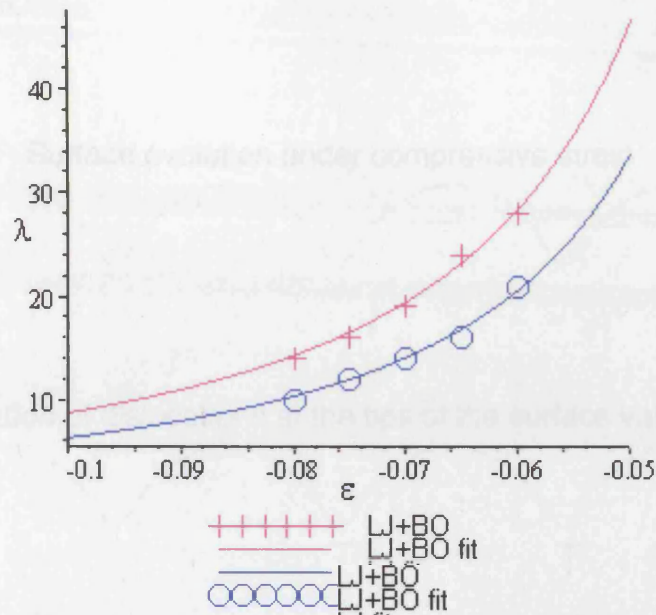


Figure 6.8 : Roughening wavelength as a function of mismatch strain for LJ and LJ+BO surfaces obtained from off-lattice KMC simulations.

6.3 Relaxation of a rough surface by dislocation nucleation

As seen in the off-lattice KMC simulations of section 6.1, critically strained surfaces are unstable and will roughen at a particular wavelength. As the roughening process proceeds the amplitude of the surface undulation increases and the stress in the troughs grows. This stress concentration can lead to rapid migration of atoms from this region causing the formation of a deep, sharp groove, commonly referred to as a cusp [4]. This is illustrated in Figure 6.9a. The high stresses at the cusp tip make them strong potential sources for the nucleation of dislocations. This suggests that there is a critical point during the evolution at which a misfit dislocation will be nucleated at a surface valley. This is shown in Figure 6.9b. It is expected that the nucleation of a dislocation will locally reduced the elastic strain energy at the cusp tip making it a favourable site for atoms to jump into again. This will lead to a refilling of the cusp trough and a coalescence of the two islands between. Also, it is a process by which a dislocation can enter a material without glide. This process is shown in Figure 6.9c. Here we simulate the process of dislocation nucleation on roughened surfaces using the off-lattice KMC model. This is ideal for this simulation as it allows for the rapid creation of highly non-linear elastic features such as dislocations but also evolves the surface over the much longer

diffusive time scales. The following simulations are the first to combine diffusion and dislocation nucleation.

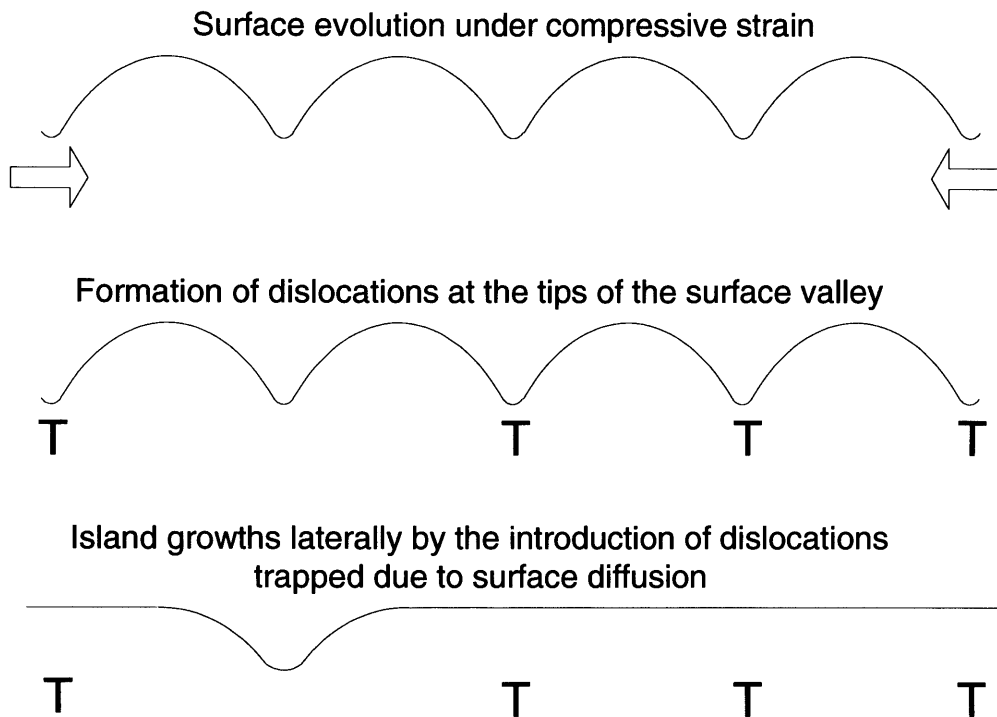
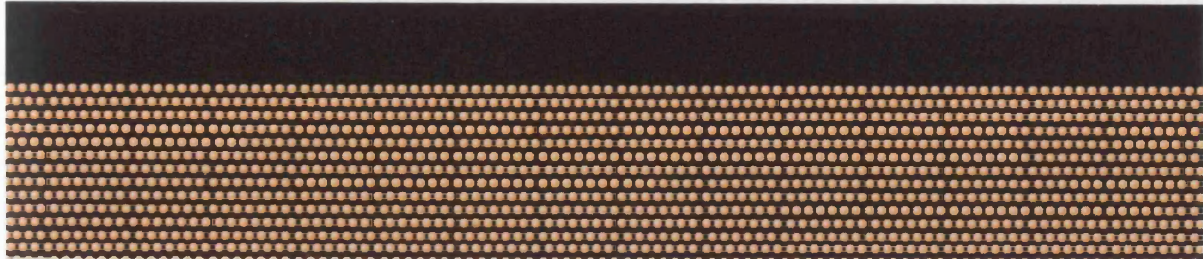


Figure 6.9 : Relaxation of the high stress concentration at the cusp tips by the formation of dislocations leads to the creation of low energy sites above the dislocation and the subsequent filling of the cusp [4].

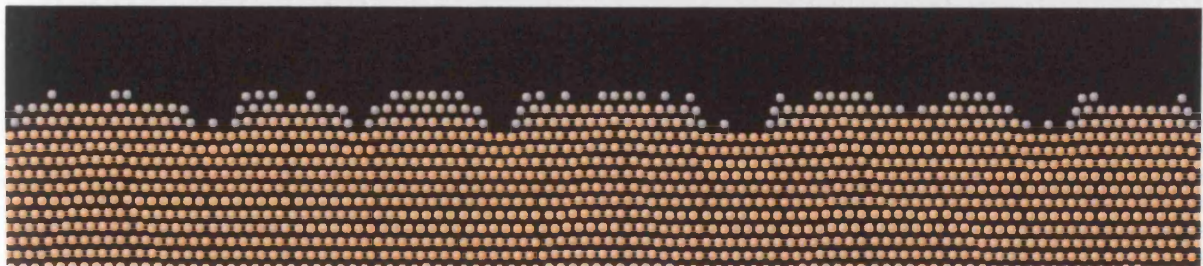
(a) Formation of a single dislocation

This section presents the results on an off-lattice KMC simulation of an LJ surface for a sample size of 100×30 atoms, normalized temperature of $\bar{T} = 0.5$ and mismatch strain of $\varepsilon_x = -0.06$. Snapshots of the evolution are shown in Figure 6.10. Initially the surface roughens at a particular wavelength as seen before. Sharp, deep grooves are formed in the surface creating effective islands of material between them. In Figure 6.10c it can be seen that a dislocation is generated at one of these surface valleys. Figure 6.10d shows that it is subsequently trapped behind the free surface by the motion of surface atoms back into the trough. This leads to the effective coalescence of the islands after a long time (as shown in Figure 6.10f). The dislocation appears below the first surface monolayer and is therefore nucleated by a rapid atomic rearrangement. The dislocation can then move along the glide plane underneath the island to find its minimum energy position. The change in the strain

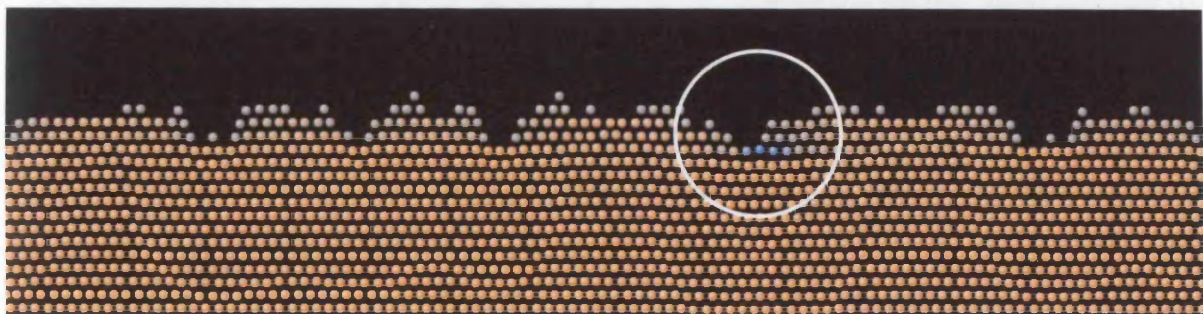
energy breaks the balance between the previous strain energy and surface energy and drives a change in the surface morphology. Another mechanism for dislocation nucleation could be atoms jumping on to surfaces sites which do not correspond to fully coherent lattice sites.



(a) $N=0$



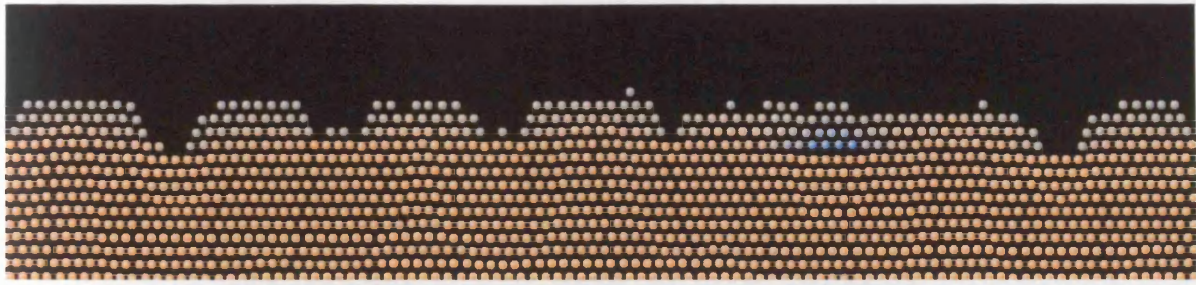
(b) $N=13 \times 500$



(c) $N=14 \times 500$



(d) $N=20 \times 500$



(e) $N=40 \times 500$



(f) $N=185 \times 500$

Figure 6.10 : Formation of the a misfit dislocation during the roughening of a strained LJ surface by off-lattice KMC simulation. Note that not all of the bulk atoms are shown. N is the number of atomic jumps.

Formation of misfit dislocations from cusps in roughened heteroepitaxial thin films have been found in experiments [50]. An example of such a dislocation is shown in Figure 6.11. The dislocation is found in the bottom of a rounded trough which was initially sharp and has refilled once the dislocation has relieved the local strain energy.

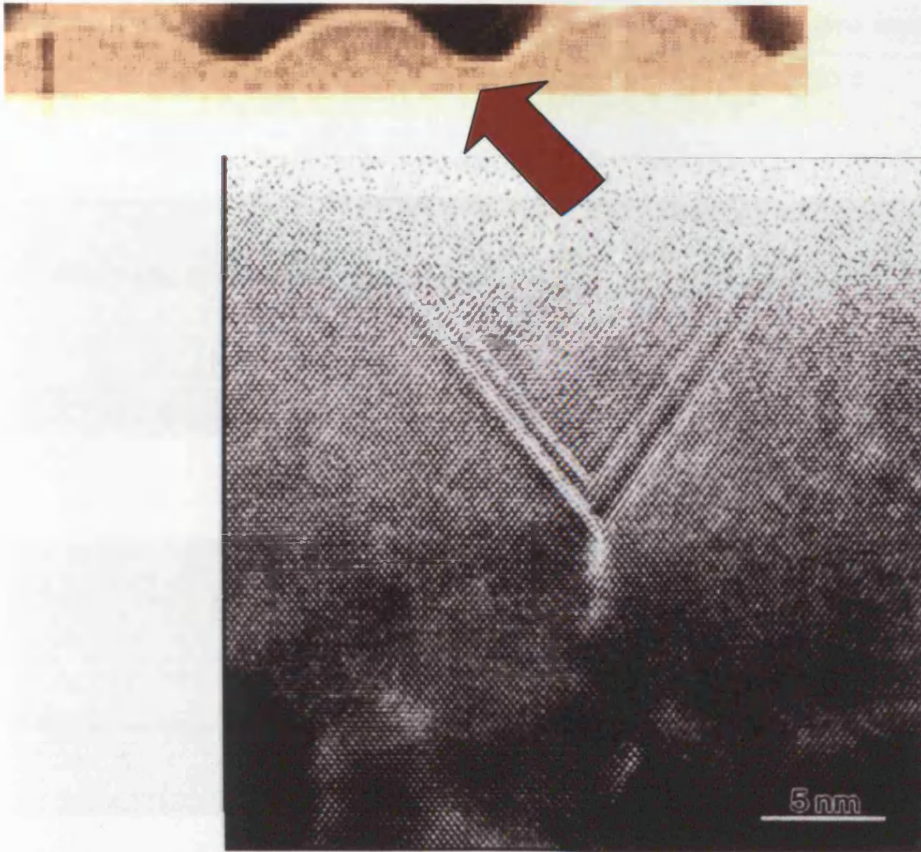
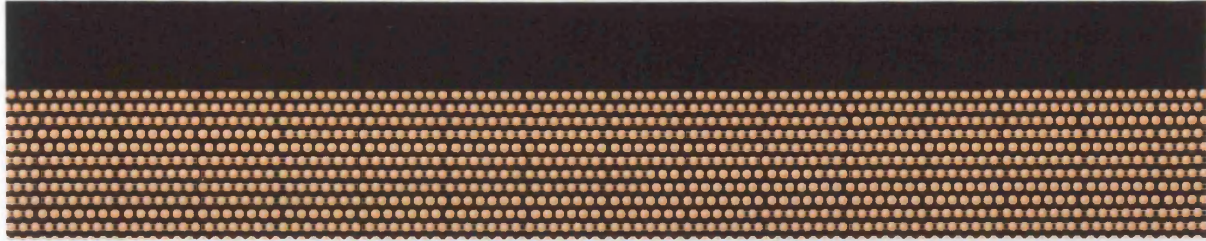


Figure 6.11 : Cross-section TEM image of a V-shaped defect at the tip of the cusp valley for a 500-Å-thick $Si_{0.78}Ge_{0.22}/Si$ film [50].

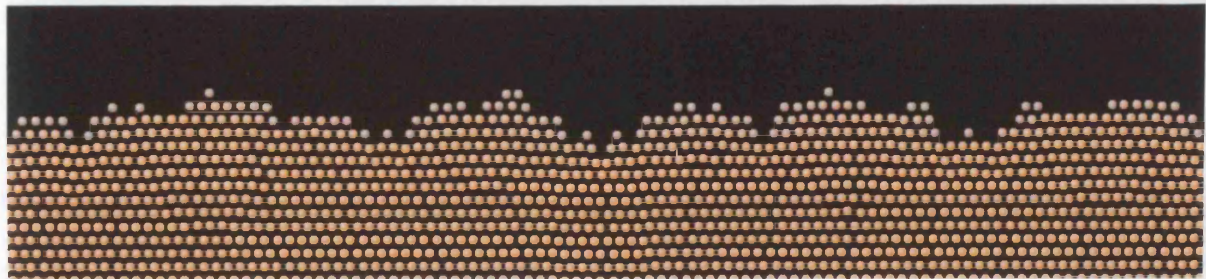
(b) Formation of multiple dislocations

The results presented here are produced in a similar way to those presented in the previous subsection, except the compressive strain has been increased from $\epsilon_x = -0.06$ to $\epsilon_x = -0.065$. Snapshots of the evolution are taken every 500 atomic jumps. Particular profiles of interest are shown in Figure 6.12. As before, the surface is unstable and roughens. The first misfit dislocation is formed at a surface valley and then trapped as shown in Figure 6.12c. The second dislocation is generated at the surface valley in a similar fashion to the first one in Figure 6.12e. The third dislocation is nucleated in Figure 6.12f. This is of more interest as it is formed in a different way to the others. The previous dislocations formed under the surface monolayer, whereas this misfit dislocation is formed at the edge of the island. It then glides along the slip plane underneath the island to a lower energy position. This movement occurs without significant atomic rearrangement on the surface. The nucleation site is referred to as an edge as the cusp is not sharp. Instead there is a small flat region which separates the

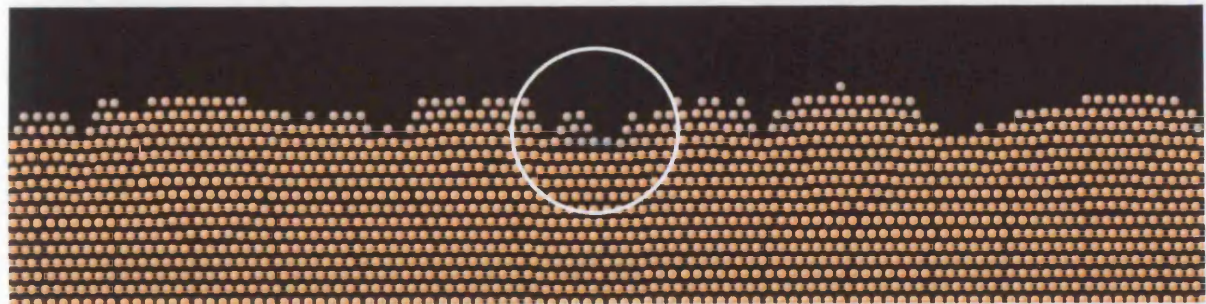
islands. Finally a fourth dislocation is formed at one of the two remaining cusps in Figure 6.12i. The cusp is then refilled and the dislocation buried as before.



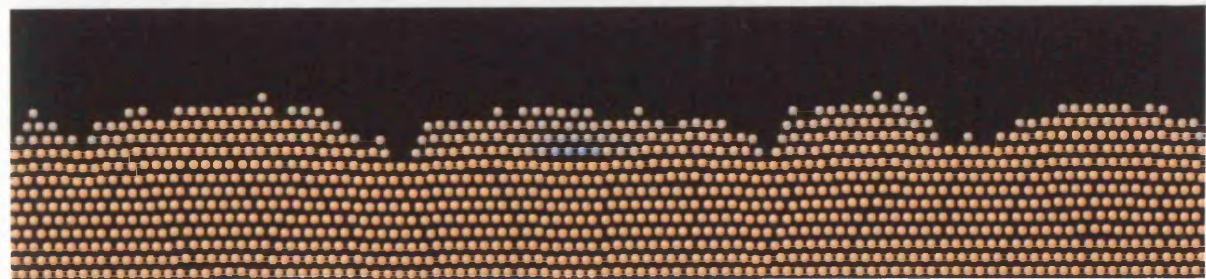
(a) $N=0$



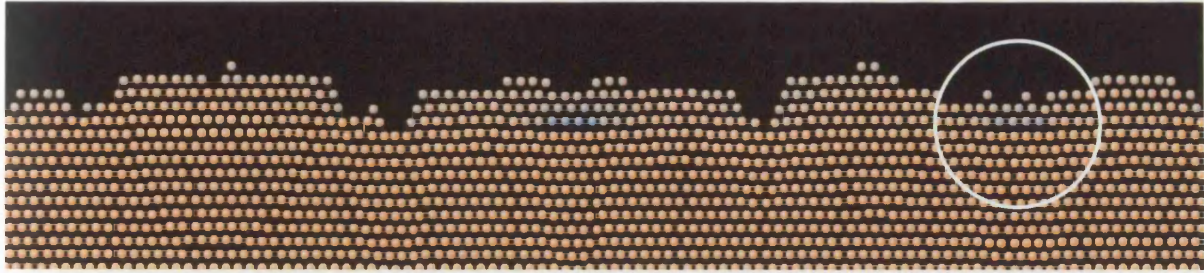
(b) $N=12*500$



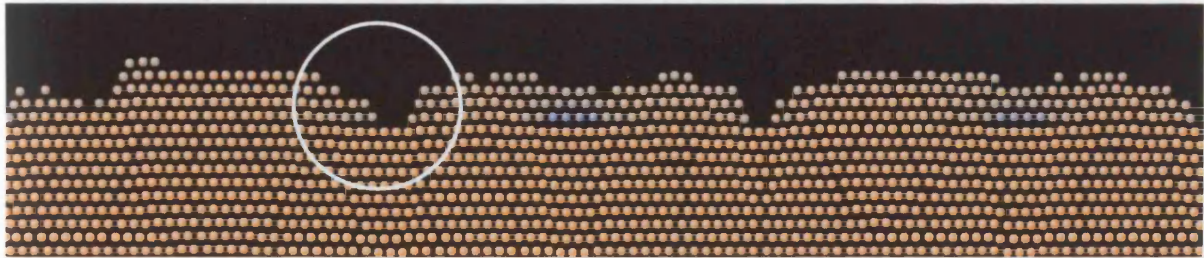
(c) $N=13*500$, the first dislocation is generated.



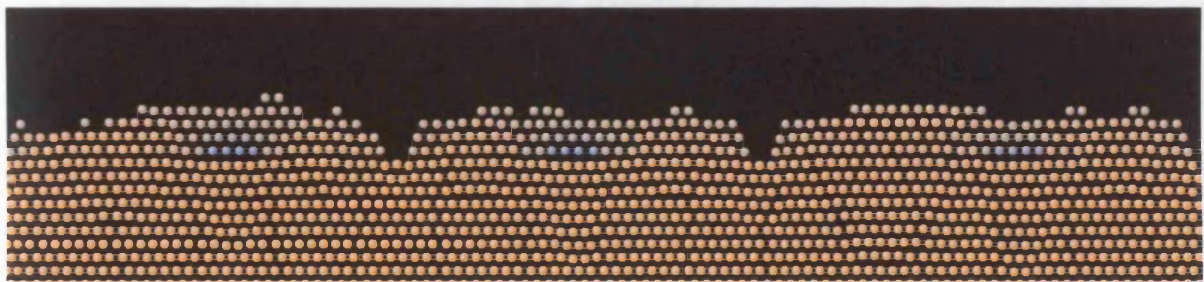
(d) $N=30*500$



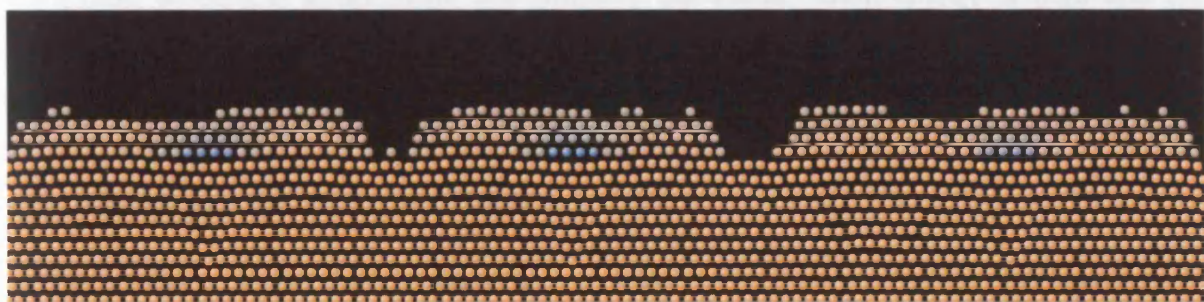
(e) $N=31*500$, the second dislocation is generated.



(f) $N=54*500$, the third is formed at the edge of an island.



(g) $N=55*500$, the third misfit dislocation glides into the island along the plane of the bottom of the island.



(h) $N=109*500$

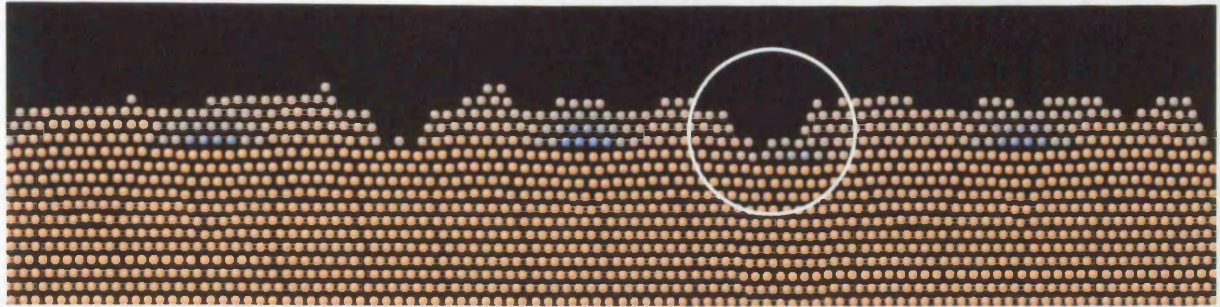
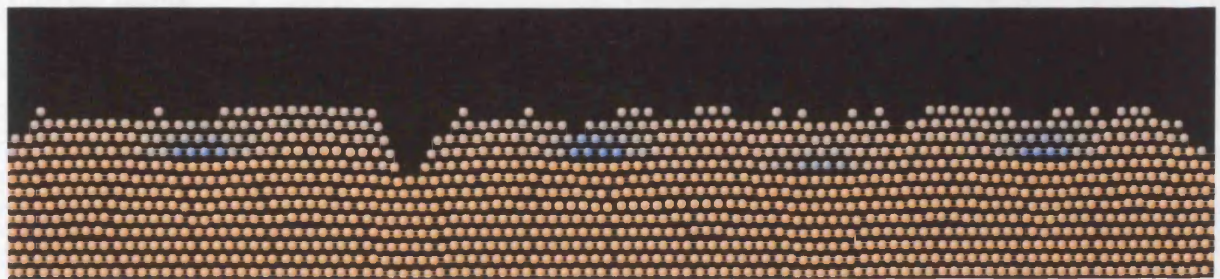
(i) $N=110*500$, the fourth is formed at the surface valley.(j) $N=460*500$

Figure 6.12 : Dislocation-induced coalescence of islands by off-lattice KMC simulation using the LJ potential.

One interesting observation on the nucleation process is that the time of the dislocation formation can be approximately fitted as $2^{n-1}t_{disloc}$, where n is the number of dislocations and t_{disloc} is the time of forming the first dislocation. This suggests that the nucleation process is a stochastic one. Initially the elastic strain energy is high and the probability of dislocation is large. As the strain energy decreases by successive dislocation formation the probability for further dislocation nucleation diminishes.

6.4 Summary

In this section, the morphological stability of a strained surface has been investigated from both a continuum perspective and an atomistic perspective. Both of these approaches show that the flat strained surface is unstable above a critical strain magnitude, but that a discontinuous minima in the strain energy can stabilise a strained film below this strain magnitude. The competition between the strain energy and the surface energy leads to the surface roughening at a particular wavelength. This is consistent with the results of experiments. The wavelengths seen in the off-lattice KMC simulations are in good agreement with the general predictions of small perturbation analysis but the exact fitting parameters are

not clearly determined from analytical calculations. The initial small amplitude sinusoidal waviness of the surface is seen to develop into a cusped profile for large perturbations in the non-linear regime. These cusps are stress concentration sites and act as preferential locations for dislocation nucleation. The off-lattice KMC simulations presented demonstrate two mechanisms for the formation of the misfit dislocations: (1) a misfit dislocation is generated at a surface valley and then trapped by the motion of the surface; (2) a misfit dislocation is nucleated at the edge of the island and then glides along the plane of the bottom of the island into the island.

7.0 Discussion and Conclusions

This thesis has proposed and investigated models for the thermodynamics and kinetics of heteroepitaxial systems at different length and time scales. In this final chapter, the main achievements of this work are summarized and discussed in the context of progress in the subject area and further work.

In chapter 2, an atomistic model based on the Lennard-Jones (LJ) potential with and without bond-order (BO) has been used to derive macroscopic bulk properties such as Young's modulus and Poisson ratio, and macroscopic surface properties such as surface energy and surface stress. The latter property arises due to the difference in lattice spacing between bulk and surface atoms in the LJ+BO model. The predicted surface energy for the LJ+BO potential is only 21% of the LJ value. The thermodynamics of the two systems would therefore be expected to differ substantially at the nanoscale. This difference has been explored further in subsequent chapters. As discussed below, a difference has been observed, although it is less substantial than the values for the surface energy would suggest. This is because the surface energy values are for a flat surface. It is well known that steps on the surface are often the principal features in controlling the thermodynamics of a vicinal surface. The kinetics must also be considered.

The thermodynamics of an individual surface step were considered in chapter 3. This introduced the problem of multiple length scales, as the elastic field generated by a discontinuity in the surface stress (which only occurs with the LJ+BO potential) acts over a long range. The large atomistic lattice statics model required to represent the substrate and surface would involve too many degrees-of-freedom for efficient calculation. A novel hybrid atomistic-continuum models has been developed to remove many of the redundant degrees-of-freedom by combining the atomistic model with an equivalent continuum one. Both a force dipole model and a finite element model were used to model the continuum. Complications in this type of concurrent multiscale model arise for two reasons. Firstly, the surface and bulk elastic properties of the atomistic model must be derived to construct a consistent continuum representation. In this case this was achieved in chapter 2. Secondly, the transfer of information between the two descriptions must be smooth and accurate. This was achieved by creating a linkage between the displacements on the boundary between the atomistic and

continuum regions. The surface stress in the LJ+BO model was represented by a transformation strain in the surface layer in the continuum region. This naturally introduces a length scale into the continuum region. Using a continuum approximation for the surface in this way is unique. Other multiscale approaches have retained the atomistic representation for the surface [12][16]. These models are all zero-temperature models in that only the equilibrium positions of atoms are considered whilst their finite temperature lattice vibrations are ignored. Finite temperature effects are important for dynamic effects such as dislocation motion (which is easier at higher temperatures). Some preliminary work has been done on finite-temperature multiscale models [66][67] but they are still in their infancy. This type of dynamics is ignored in this thesis, as the time scales of interest are diffusive (of the order of seconds) rather than inertial (of the order of nanoseconds). This evolution of surfaces by surface diffusion has been investigated in the remaining chapters.

Chapters 4 and 5 explored the flattening of a rough (sinusoidal) surface by surface diffusion. The driving force is a reduction in surface energy, although there is also a small elastic driving force in the case of the LJ+BO potential due to the presence of a surface stress. Chapter 4 investigated this phenomena using an appropriate atomistic model. A novel off-lattice Kinetic Monte Carlo (KMC) model has been developed. This essentially allows a fully relaxed lattice statics simulation to evolve over time via diffusive events which occur over long time scales. The only significant limitation is that the possible events must be prescribed previously. This is not a major setback in 2D where the events are obvious, but is more limiting in 3D. The off-lattice KMC model allows for full, non-linear atomic interactions and calculates the transition energy barrier between states accurately for each event. It can therefore include the effect of strain on the thermodynamics and kinetics, and also allow for the possibility of defect nucleation and motion in the atomic lattice. However, as with all atomistic simulations, the computational overhead is large which places a limitation on the size of the samples that can be considered. Overall it has been found that the decay of the amplitude of the sine wave is found to be exponential in the majority of cases, consistent with the standard Herring-Mullins' continuum theory for surface diffusion over an isotropic surface. However, the surface mobility is found to have a λ^{-2} dependence (for a sinusoid of wavelength λ) which is not consistent with this theory. The LJ+BO potential model decays slightly faster than the LJ potential model. This goes against our initial expectation as the surface energy for the LJ+BO model is only 21% of that in the LJ model. Also, the decay for the LJ+BO potential model for the short wavelength sinusoid at low temperature is not well

described by an exponential curve, indicating that the kinetics of step attachment and detachment are significant at low terrace lengths and temperatures.

A continuum microscopic step flow model has been developed in chapter 5 to predict the results of the atomistic simulations in chapter 4. The motivation for this is three-fold. Firstly, this process allows us to gain further understanding of the dominant mechanisms involved in the surface evolution. Secondly, the step flow simulations are very fast compared to the atomistic ones. Development of a representative step flow model for a surface would allow much larger problems to be investigated. Thirdly, the step flow model is a useful intermediate stage between the atomistic and a higher order continuum model and has allowed a relationship between the atomistic potentials and macroscopic surface parameters to be developed. It was found that a symmetric step flow model in the literature was insufficient to predict the flattening of the surface. The model was consequently expanded to look at asymmetries in the step behaviour. Parameters in the new step flow model were related to the diffusion barriers for the five fundamental surface diffusion processes around a step. Simulations of step flow were then compared with the off-lattice KMC results. Diffusion Limited (DL) growth was found to dominate the kinetics (i.e. motion of atoms across terraces rather than around steps). The results were found to be in very good agreement for the LJ potential. This demonstrated that the individual diffusion barriers could be assembled in a non-trivial way to correctly predict the macroscopic surface mobility. The λ^{-2} dependence of the surface mobility was explained. However, the results were not in good agreement for the LJ+BO potential. This was assumed to be due to the additional complexity of surface strain and its effect on the diffusion barriers and interactions between steps, adatoms and other steps. This suggests that this area would benefit from further investigation, possibly making the transition energy barriers dependent on strain.

The full scenario of heteroepitaxial surface evolution is explored in chapter 6. The widely accepted continuum Azaro-Grinfeld-Tiller (ATG) theory proposes that an initially flat surface under an applied strain is unstable and will roughen at a particular wavelength due to the competition between surface energy and elastic strain energy. This theory was investigated using the off-lattice KMC model of chapter 4, which naturally accounts for the full effects of strain. The simulation results showed that the surface was stable below a certain strain magnitude, contradicting the predictions of the well established ATG theory. However, the films did roughen at a strain magnitude above about 5%. Height-height correlation functions were used to characterise the surface morphology and demonstrated that a particular

roughening wavelength developed. A novel extension of the ATG theory has been proposed which removes the assumption that the surface energy is a smooth function of surface orientation and considers a cusped surface energy function. This theory correctly predicts the form of the relationship between the roughening wavelength and the applied strain, although the exact fitting parameters are not easily related to the assumed macroscopic properties precisely due to the complexity of the problem. The wavelengths for the LJ+BO potential are larger than those for the LJ potential by 40% indicating that this system possesses a higher surface stiffness. Again this goes against the expectations of the simple surface energy model of chapter 2 which predicts that the LJ+BO potential has a much lower surface energy. This shows that these systems exhibit a rich range of phenomena which requires further research. Periodic surface profiles of 2D ridges formed in the initial stages of roughening have been observed in annealing experiments of SiGe heteroepitaxial thin films[50][97]. However, these 2D ridges always evolves into 3D isolated islands. It would be a challenging but useful extension of this work to extend the off-lattice KMC simulation to three dimensions. This would allow for real transition energy barriers to be calculated (without the necessity for the removal of an extra Ehrlich-Schwoebel barrier) and allow for purely 3D phenomena such as surface reconstructions and diffusion along steps.

Finally, chapter 6 concludes with a highly novel investigation into the interaction between diffusion and defect nucleation. Annealing experiments have shown that a surface can roughen to such an extent that sharp cusps form at surface valleys. These stress concentration features are expected to play a crucial role in the nucleation of misfit dislocations. Off-lattice KMC simulations demonstrate this process and provide useful information about the mechanics of dislocation formation and the consequent change of surface morphology. Misfit dislocations are inevitably generated in heteroepitaxial thin films at large misfit strains. Traditionally, the formation of dislocation has been modelled in terms of a gliding process [103][104], [109]. Assuming the free surface is fixed, a dislocation loop after nucleation expands on a preferred glide plane. If mass transport over the surface takes part in the misfit strain relieving, dislocations can be formed without glide [105]. Off-lattice KMC simulations demonstrate such nucleation of dislocations during the roughening of a strained surface.

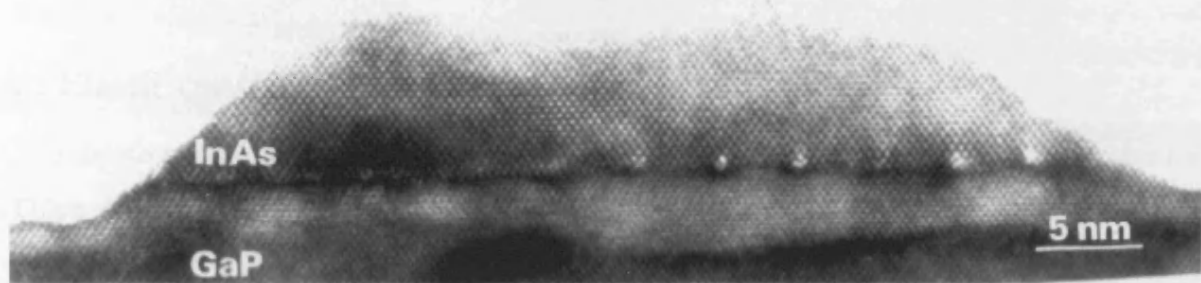


Figure 7.1 : High-resolution electron microscopy (HREM) image of InAs island on GaP [100]

As mentioned before, the atomistic off-lattice KMC simulations are slow. This restricts the size of the sample that can be considered. This is particularly restrictive in the analysis of strained films as there are long range elastic interactions. The formation of mounds with a wavelength which is a significant fraction of the system size is therefore undesirable and only avoidable at very high strains at which the wavelength is small. It would be useful to improve the implementation of the off-lattice KMC algorithm by making the calculations more efficient and more intelligent [108]. This would allow for actual heteroepitaxial systems using more representative interatomic potentials to be considered. Amongst other things, this could be used to model the phenomena of step bunching, or the growth of heteroepitaxial islands by the Stranski-Krastanov mode (e.g., Ge on Si with -4% mismatch strain) or the Volmer-Weber mode (e.g. InAs on GaP with -11% mismatch). The latter requires a two species model which is a trivial extension to the existing off-lattice KMC model. In general, epitaxial growth at high mismatches is by island formation rather than layer by layer growth. Several experiments have been done for the growth of heteroepitaxial thin films at high mismatches to study the formation of strain-relieving dislocations [98] [99][100]. Initially the island growth is almost vertical until the formation of a dislocation at the edge of an island. This reduces the strain energy of the island as it is no longer coherent with the substrate and leads to rapid lateral growth of the island. These islands grow by periodic lateral growth each time that a new dislocation is formed at the edge of the island. Figure 7.1 shows the results of this process in a high-resolution electron microscopy (HREM) image of an InAs island grown on GaP.

Appendix

A : Elastic constants from the atomistic model

Co-ordinate transformation is illustrated in **Figure A-1** due to the deformation. The strains for 2D are defined as

$$\begin{bmatrix} \underline{x}' \\ \underline{y}' \end{bmatrix} = \begin{bmatrix} (1 + \varepsilon_{xx}) & \varepsilon_{xy} \\ \varepsilon_{xy} & (1 + \varepsilon_{yy}) \end{bmatrix} \begin{bmatrix} \underline{\hat{x}} \\ \underline{\hat{y}} \end{bmatrix}, \quad (\text{A-1})$$

where $\underline{\hat{x}}$ and $\underline{\hat{y}}$ are unit vectors, \underline{x}' \underline{y}' are deformed unit vectors, ε_{xx} , ε_{yy} and ε_{xy} are the strains in x-direction, y-direction and shear strains. And $\varepsilon_{xy} \equiv \frac{1}{2} \gamma_{xy}$.

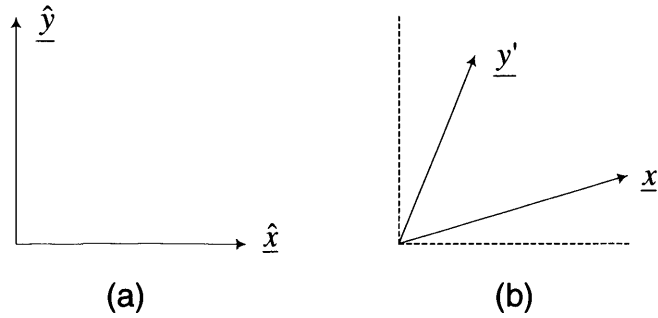


Figure A-1 : Co-ordinate transformation. (a) Undeformed basis, $\underline{\hat{x}}$ and $\underline{\hat{y}}$ are unit vectors. (b) Deformed basis.

A segment $\underline{P}_i \underline{P}_j$ is deformed to $\underline{P}_i' \underline{P}_j'$ as shown in **Figure A-2**. $\underline{P}_i, \underline{P}_j, \underline{P}_i', \underline{P}_j'$ can be expressed as

$$\begin{aligned} \underline{P}_i &= x_i \underline{\hat{x}} + y_i \underline{\hat{y}}, \\ \underline{P}_j &= x_j \underline{\hat{x}} + y_j \underline{\hat{y}}, \\ \underline{P}_i' &= x_i \underline{x}' + y_i \underline{y}', \\ \underline{P}_j' &= x_j \underline{x}' + y_j \underline{y}'. \end{aligned} \quad (\text{A-2})$$

where $\underline{x}' = (1 + \varepsilon_{xx}) \underline{\hat{x}} + \varepsilon_{xy} \underline{\hat{y}}$ and $\underline{y}' = \varepsilon_{xy} \underline{\hat{x}} + (1 + \varepsilon_{yy}) \underline{\hat{y}}$ are obtained from eqn(A-1).

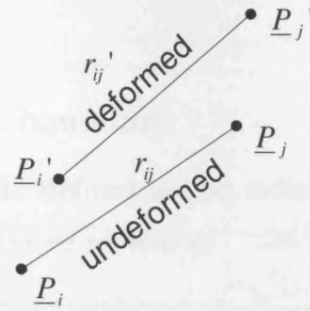


Figure A-2 : A segment $\underline{P}_i \underline{P}_j$ is deformed to $\underline{P}_i' \underline{P}_j'$.

For undeformed segment $\underline{P}_i \underline{P}_j$,

$$r_{ij}^2 = (x_j - x_i)^2 + (y_j - y_i)^2 \quad (\text{A-3})$$

For deformed segment $\underline{P}_i' \underline{P}_j'$,

$$r_{ij'}^2 = [(x_j - x_i)(1 + \epsilon_{xx}) + (y_j - y_i)\epsilon_{xy}]^2 + [(x_j - x_i)\epsilon_{xy} + (y_j - y_i)(1 + \epsilon_{yy})]^2. \quad (\text{A-4})$$

For 6-nearest neighbour atoms illustrated in **Figure A-3**, the deformed distances between atom i and j are calculated in terms of equation (A-4). They are expressed as

$$r_{i1}^2 = r_{i4}^2 = r_0^2(1 + \rho_1)$$

$$r_{i2}^2 = r_{i5}^2 = r_0^2(1 + \rho_2),$$

$$r_{i3}^2 = r_{i6}^2 = r_0^2(1 + \rho_3)$$

where

$$\rho_1 = 2\epsilon_{xx} + \epsilon_{xx}^2 + \epsilon_{xy}^2$$

$$\rho_2 = \frac{1}{2}\epsilon_{xx} + \frac{1}{4}\epsilon_{xx}^2 + \frac{3}{2}\epsilon_{yy} + \frac{3}{4}\epsilon_{yy}^2 + \epsilon_{xy}^2 + \frac{\sqrt{3}}{2}\epsilon_{xy}(2 + \epsilon_{xx} + \epsilon_{yy})$$

$$\rho_3 = \frac{1}{2}\epsilon_{xx} + \frac{1}{4}\epsilon_{xx}^2 + \frac{3}{2}\epsilon_{yy} + \frac{3}{4}\epsilon_{yy}^2 + \epsilon_{xy}^2 - \frac{\sqrt{3}}{2}\epsilon_{xy}(2 + \epsilon_{xx} + \epsilon_{yy})$$

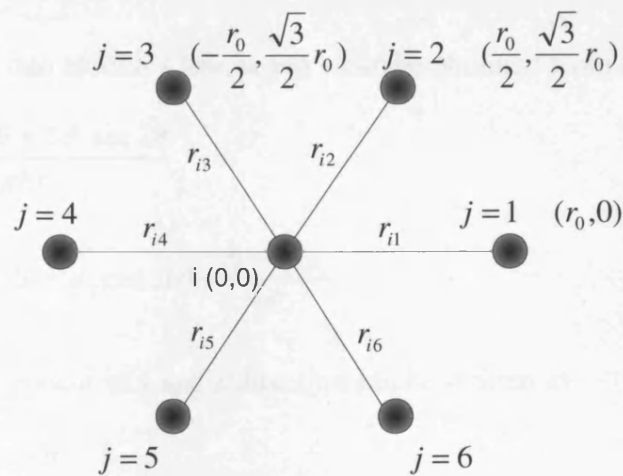


Figure A-3 : Atom i with 6 nearest-neighbour atoms.

B : The displacement on the boundary

In polar co-ordinates, u and v are defined as the radial and tangential component of the displacement. Strain components can be written as

$$\varepsilon_r = \frac{\partial u}{\partial r} \quad (\text{B-1})$$

$$\varepsilon_\theta = \frac{u}{r} + \frac{\partial v}{r \partial \theta} \quad (\text{B-2})$$

$$\gamma_{r\theta} = \frac{\partial u}{r \partial \theta} + \frac{\partial v}{\partial r} - \frac{v}{r} \quad (\text{B-3})$$

where ε_r is the strain in radial direction, ε_θ is the tangential strain, and $\gamma_{r\theta}$ is the shearing strain [76].

Hooke's law for plane stress is

$$\varepsilon_r = \frac{1}{E}(\sigma_r - \nu \sigma_\theta), \quad (\text{B-4})$$

$$\varepsilon_\theta = \frac{1}{E}(\sigma_\theta - \nu \sigma_r), \quad (\text{B-5})$$

$$\gamma_{r\theta} = \frac{1}{G} \tau_{r\theta}, \quad (\text{B-6})$$

where $G = \frac{E}{2(1+\nu)}$, and E & ν are Young's modulus and Poisson ratio. Substituting

expression (B-4~B-6) into Hooke's law, u and v can be obtained from (B-1~B-3) as follows

$$u = -\frac{2d_x \cos 2\theta + 2d_z \sin 2\theta}{\pi E r} \quad (\text{B-7})$$

$$v = \frac{1-\nu}{\pi E r} (d_x \sin 2\theta - d_z \cos 2\theta) + \frac{(1+\nu)d_z}{\pi E r} \quad (\text{B-8})$$

The displacement component in x and z direction can be written as

$$u_x = u \sin \theta + v \cos \theta \quad (\text{B-9})$$

$$u_z = u \cos \theta - v \sin \theta \quad (\text{B-10})$$

C : The relationship between the strains and displacements

The elastic energy of the element can be then rewritten as

$$\begin{aligned}
 U_e &= \frac{1}{2} \int_{V_e} [u^e]^T [B^e]^T [C^e] [B^e] [u^e] dV \\
 &= \frac{1}{2} [u^e]^T [k^e] [u^e]
 \end{aligned}
 \tag{C-0}$$

where $[k^e] = \int_{V_e} [B^e]^T [C^e] [B^e] dV$ is the elemental stiffness matrix. It can be calculated numerically by using Gaussian integration in **Appendix D**.

C.1 Three-noded triangular element

In practice the elements are not the same shape. An isoparametric element is used to map general triangular element as shown in **Figure C.1**.

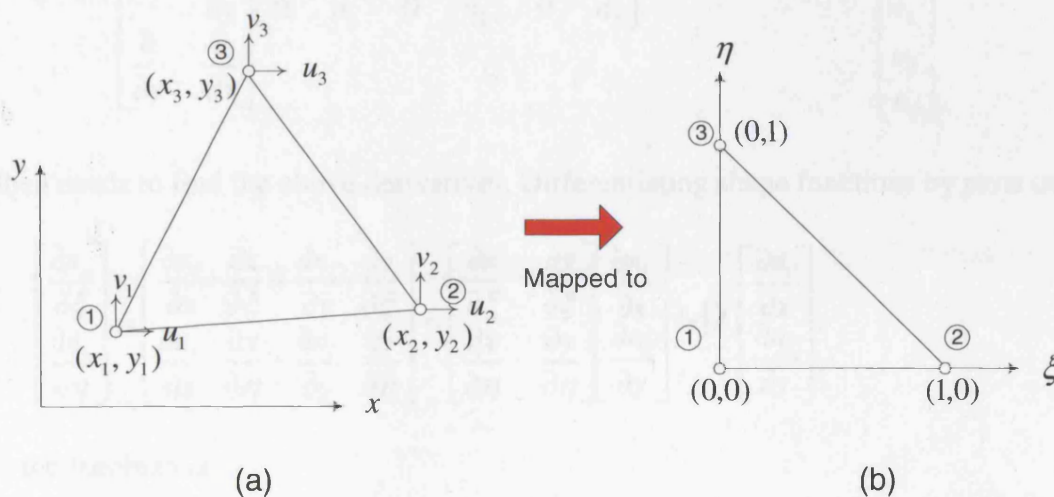


Figure C.1 : Three-noded linear triangular element: (a) real three-noded triangular element, (b) Isoparametric element

A linear mapping function is introduced to express point displacement (u, v) within general element in Figure C.1a in terms of the point (ξ, η) in Figure C.1b as

$$u(\xi, \eta) = n_1(\xi, \eta)u_1 + n_2(\xi, \eta)u_2 + n_3(\xi, \eta)u_3, \quad (C-1)$$

$$v(\xi, \eta) = n_1(\xi, \eta)v_1 + n_2(\xi, \eta)v_2 + n_3(\xi, \eta)v_3, \quad (C-2)$$

where u_1, v_1, u_2, v_2, u_3 and v_3 are nodal displacements. The shape functions are

$$n_1(\xi, \eta) = 1 - \xi - \eta,$$

$$n_2(\xi, \eta) = \xi,$$

$$n_3(\xi, \eta) = \eta.$$

We know the strains $\epsilon_x = \frac{\partial u(\xi, \eta)}{\partial x}$, $\epsilon_y = \frac{\partial v(\xi, \eta)}{\partial y}$ and $\gamma_{xy} = \frac{\partial u(\xi, \eta)}{\partial y} + \frac{\partial v(\xi, \eta)}{\partial x}$ for 2D case.

So the strain vector is expressed as

$$[\epsilon] = [B^e] [u^e],$$

where the strain displacement matrix in 2D for three-noded triangular element is

$$[B^e] = \begin{bmatrix} \frac{\partial}{\partial x} & 0 \\ 0 & \frac{\partial}{\partial y} \\ \frac{\partial}{\partial y} & \frac{\partial}{\partial x} \end{bmatrix} \begin{bmatrix} n_1 & 0 & n_2 & 0 & n_3 & 0 \\ 0 & n_1 & 0 & n_2 & 0 & n_3 \end{bmatrix} \quad \text{and} \quad [u^e] = \begin{bmatrix} u_1 \\ v_1 \\ u_2 \\ v_2 \\ u_3 \\ v_3 \end{bmatrix}.$$

One then needs to find the above derivatives. Differentiating shape functions by parts one has

$$\begin{bmatrix} \frac{\partial n_i}{\partial \xi} \\ \frac{\partial n_i}{\partial \eta} \end{bmatrix} = \begin{bmatrix} \frac{\partial n_i}{\partial x} \cdot \frac{\partial x}{\partial \xi} + \frac{\partial n_i}{\partial y} \cdot \frac{\partial y}{\partial \xi} \\ \frac{\partial n_i}{\partial x} \cdot \frac{\partial x}{\partial \eta} + \frac{\partial n_i}{\partial y} \cdot \frac{\partial y}{\partial \eta} \end{bmatrix} = \begin{bmatrix} \frac{\partial x}{\partial \xi} & \frac{\partial y}{\partial \xi} \\ \frac{\partial x}{\partial \eta} & \frac{\partial y}{\partial \eta} \end{bmatrix} \begin{bmatrix} \frac{\partial n_i}{\partial x} \\ \frac{\partial n_i}{\partial y} \end{bmatrix} = [J] \begin{bmatrix} \frac{\partial n_i}{\partial x} \\ \frac{\partial n_i}{\partial y} \end{bmatrix},$$

where the Jacobian is

$$[J] = \begin{bmatrix} (x_2 - x_1) & (y_2 - y_1) \\ (x_3 - x_1) & (y_3 - y_1) \end{bmatrix}.$$

Hence

$$\begin{bmatrix} \frac{\partial n_i}{\partial x} \\ \frac{\partial n_i}{\partial y} \end{bmatrix} = \frac{1}{|J|} \begin{bmatrix} (y_3 - y_1) & -(y_2 - y_1) \\ -(x_3 - x_1) & (x_2 - x_1) \end{bmatrix} \begin{bmatrix} \frac{\partial n_i}{\partial \xi} \\ \frac{\partial n_i}{\partial \eta} \end{bmatrix},$$

where $|J| = |(y_3 - y_1)(x_2 - x_1) - (y_2 - y_1)(x_3 - x_1)|$ is the determinant of the Jacobian matrix.

Thus the strain displacement matrix for three-noded triangular element is written as

$$[B^e] = \frac{1}{|J|} \begin{bmatrix} -(y_3 - y_2) & 0 & (y_3 - y_1) & 0 & -(y_2 - y_1) & 0 \\ 0 & (x_3 - x_2) & 0 & -(x_3 - x_1) & 0 & (x_2 - x_1) \\ (x_3 - x_2) & -(y_3 - y_2) & -(x_3 - x_1) & (y_3 - y_1) & (x_2 - x_1) & -(y_2 - y_1) \end{bmatrix}.$$

C.2 Six-noded quadratic triangular element

The above three-noded element is known as the constant strain element. It doesn't approximate well to a continuous strain field. Generally six-noded quadratic triangular elements are most widely used 2D elements as shown in Figure C.2.

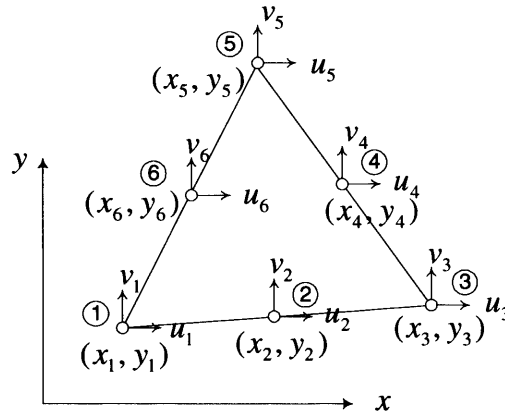


Figure C.2 : Six-noded quadratic triangular element

The Jacobian matrix can be expressed generally as

$$[J] = \begin{bmatrix} \frac{\partial x}{\partial \xi} & \frac{\partial y}{\partial \xi} \\ \frac{\partial x}{\partial \eta} & \frac{\partial y}{\partial \eta} \end{bmatrix} = \begin{bmatrix} n_{i,\xi}(\xi, \eta)x_i & n_{i,\xi}(\xi, \eta)y_i \\ n_{i,\eta}(\xi, \eta)x_i & n_{i,\eta}(\xi, \eta)y_i \end{bmatrix},$$

where $i = 1, 2, \dots, 6$ is a number of nodes and $n_{i,\xi}(\xi, \eta) = \frac{\partial n_i(\xi, \eta)}{\partial \xi}$. The shape function can

be written as

$$n_1 = (1 - \eta - \xi)(1 - 2\eta - 2\xi),$$

$$n_2 = \xi(2\xi - 1),$$

$$n_3 = \eta(2\eta - 1),$$

$$n_4 = 4(1 - \eta - \xi)\xi,$$

$$n_5 = 4\xi\eta,$$

$$n_6 = 4\eta(1 - \eta - \xi).$$

Hence

$$\begin{bmatrix} \frac{\partial n_i}{\partial x} \\ \frac{\partial n_i}{\partial y} \end{bmatrix} = \frac{1}{|J|} \begin{bmatrix} n_{i,\eta} y_i & -n_{i,\xi} y_i \\ -n_{i,\eta} x_i & n_{i,\xi} x_i \end{bmatrix} \begin{bmatrix} \frac{\partial n_i}{\partial \xi} \\ \frac{\partial n_i}{\partial \eta} \end{bmatrix},$$

where the determinant of the Jacobian is $|J| = (n_{i,\xi} n_{j,\eta} - n_{i,\eta} n_{j,\xi}) x_i y_j = N_{ij} x_i y_j$.

Thus the strain displacement matrix is presented as

$$[B^e] = \frac{1}{|J|} [b_1^e \quad b_2^e \quad \dots \quad b_i^e \quad \dots \quad b_6^e],$$

where

$$[b_i^e] = \begin{bmatrix} N_{ij} y_j & 0 \\ 0 & -N_{ij} x_j \\ -N_{ij} x_j & N_{ij} y_j \end{bmatrix}.$$

D : Gaussian Quadrature

In my case there may be two types of triangular elements to be considered: three-noded linear element and six-noded quadratic element as shown in Figure D.1.

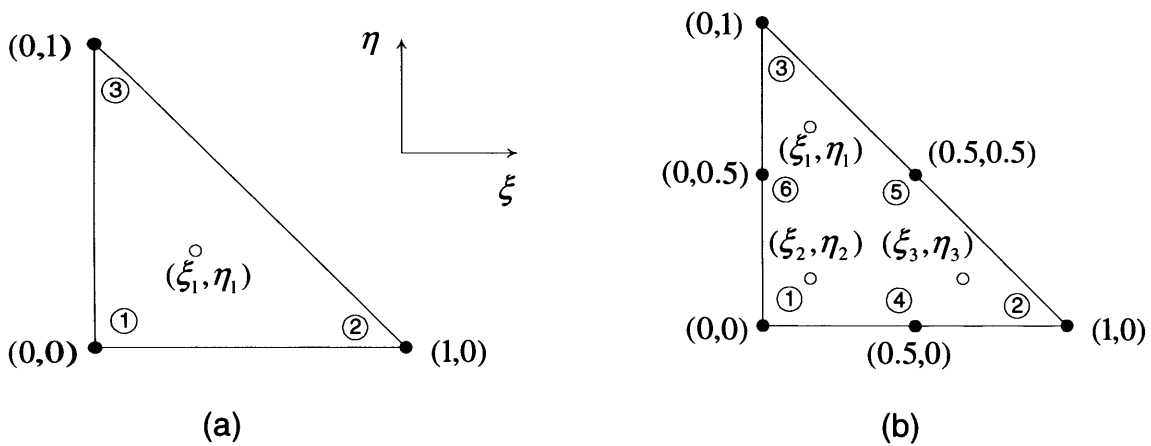


Figure D.1 : Local numbering and positioning of nodes (filled circle) and integration points (open circle) for (a) three-noded triangular element and (b) six-noded triangular element

For triangular elements there are two local coordinates (ξ and η), as described in Appendix C. The linear interpolation of displacements is provided for three-noded triangular element. In order to obtain the elemental stiffness matrix $[k^e]$, the integral over the area within the triangular element is numerically estimated as

$$[k^e] = \iint [B^e(\xi, \eta)]^T [C] [B^e(\xi, \eta)] J(\xi, \eta) d\xi d\eta = \iint f(\xi, \eta) d\xi d\eta \approx \sum_{i=1}^k f(\xi_i, \eta_i) w_i, \quad (D-1)$$

where $f(\xi_i, \eta_i)$ is the value of the function f at the Gaussian point (ξ_i, η_i) and w_i is the weight factor of the Gaussian point i .

Three-noded linear triangular elements have one Gaussian point (see Figure D.1) with position $(\xi_1, \eta_1) = (1/3, 1/3)$ and weight factor $w_1 = 1$.

Six-noded quadratic triangular element have three Gauss points. The position and weight factors of the integration points are given in Table D.1. Note that the sum of the weight factors is equal to 1.

Point	ξ_i	η_i	w_i
1	1/6	2/3	1/3
2	1/6	1/6	1/3
3	2/3	1/6	1/3

Table D.1 : 3-point Gaussian integration for 6-noded triangular elements

E : Surface diffusion and shape change

A sinusoidal surface profile is used to analyse the process of the surface diffusion here. The height of sine wave at any point is given as

$$h(x,t) = A(t) \sin\left(\frac{2\pi}{\lambda} x\right) \quad (\text{E-1})$$

where $A(t)$ is the amplitude in the time t and λ is wavelength. The driving force for evolution of the surface is the surface energy

$$E_s = \gamma_s A_s, \quad (\text{E-2})$$

where γ_s is the surface energy density or an additional energy which the surface is cleaved from the bulk, and A_s is the surface area.

A system will tend to reduce the total chemical potential, i.e. atoms will travel along the gradient of a chemical potential, μ . The flux J_s crossing unit length on the surface is proportional to the chemical potential gradient

$$J_s = -\frac{D_s \delta}{k_B T} \frac{\partial \mu}{\partial s}, \quad (\text{E-3})$$

where D_s is the surface diffusivity or diffusion coefficient, $k_B T$ is the thermal energy, δ is the number of atoms per unit area (adatom density), and the derivative along the surface $\partial/\partial s$ approximates to $\partial/\partial x$ for small slopes.

For mass conservation, the rate of the change of height of the surface is given as

$$\frac{\partial h}{\partial t} = -\Omega \frac{\partial J_s}{\partial s} \quad (\text{E-4})$$

where Ω is an atomic volume. Substituting (E-3) into (E-4) one can obtain

$$\frac{\partial h}{\partial t} = \frac{D_s \delta \Omega}{k_B T} \frac{\partial^2 \mu}{\partial s^2}. \quad (\text{E-5})$$

The velocity of a surface profile is therefore proportional to the second derivative of the chemical potential of surface atoms.

We only have surface energy to drive the surface diffusion in the system. It can be shown that in this case the chemical potential is

$$\mu = -\Omega\gamma_s K \quad (\text{E-6})$$

where γ_s is surface energy density and $K = \frac{\frac{d^2h}{dx^2}}{\left(1 + \left(\frac{dh}{dx}\right)^2\right)^{3/2}}$ is the curvature of the surface.

Assuming $dh/dx \ll 1$, (E-5) can be rewritten as

$$\frac{\partial h}{\partial t} = -B \frac{\partial^4 h}{\partial x^4} \quad (\text{E-7})$$

where $B = \frac{D_s \gamma_s \Omega^2 \delta}{k_B T}$. For a purely sinusoidal surface the decay of the amplitude is

$$\frac{dA}{dt} = -B \left(\frac{2\pi}{\lambda}\right)^4 A.$$

This has solution $A(t) = A_0 \exp(-\alpha t)$ where A_0 is the amplitude at the time $t = 0$ and

$$\alpha = B \left(\frac{2\pi}{\lambda}\right)^4 = \frac{D_s \gamma_s \Omega^2 \delta}{k_B T} \left(\frac{2\pi}{\lambda}\right)^4.$$

F : Orientational dependence of the surface energy for an unstrained surface

F.1 An LJ surface

As we have seen in Chapter 2, the surface energy density for an unstrained flat atomic surface constructed from atoms which interact via the LJ potential given in (2.1) is simply the saturated bond energy per unit area. The energy of bonds at the surface is the same as in the bulk for this potential, so some simple analytical expressions can be derived. Consider the surface step shown in Figure F.1. The unsaturated (dangling) bonds on the surface are shown as dotted lines. Each dangling bond contributes half the energy of an unstrained saturated bond of $\frac{1}{2}\omega_0$ (the energy from this bond is divided evenly between the two surfaces that are created when the bond is broken).

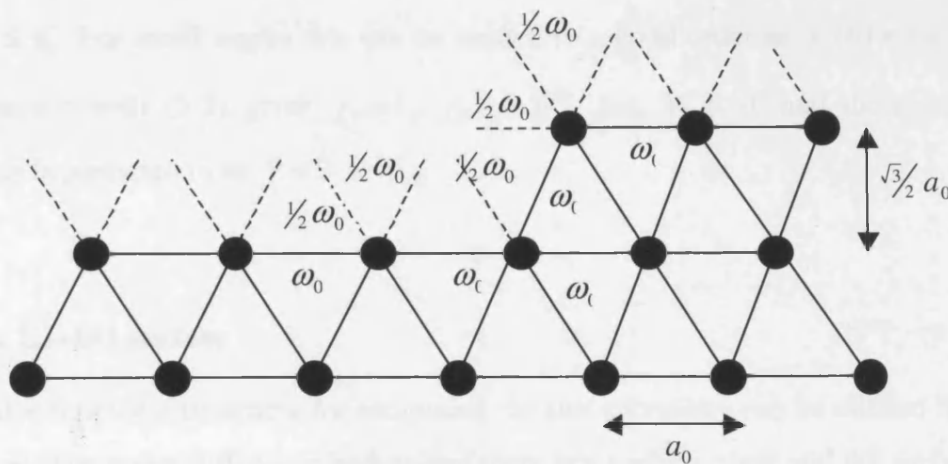


Figure F.1 : An LJ surface with a surface step. An unstrained saturated bond (solid lines) contributes ω_0 to the bulk energy. Each unsaturated (dangling) bond (dotted lines) contributes half the saturated bond energy, $\frac{1}{2}\omega_0$, to the surface energy.

A flat surface containing N atoms will have a surface energy of $2Nx \frac{1}{2}\omega_0 = N\omega_0$ and a length Na_0 . The surface energy density is therefore $\gamma(0) = \frac{N\omega_0}{Na_0} = \frac{\omega_0}{a_0}$ as found before in section 2.3.

If one surface step is introduced to the flat surface, as shown in Figure F.1, then the surface energy of N atoms will be $2Nx \frac{1}{2}\omega_0 = N\omega_0$ as before (as the atom at the bottom of the step contributes $\frac{1}{2}\omega_0$ and the atom at the top of the step contributes $3x \frac{1}{2}\omega_0$ equalling a total of $2\omega_0$ for 2 atoms). The horizontal dimension of the N atom surface is $(N - \frac{1}{2})a_0$ and the height is $\frac{\sqrt{3}}{2}a_0$ so the macroscopic surface length is taken to be $a_0\sqrt{(N - \frac{1}{2})^2 + (\frac{\sqrt{3}}{2})^2} = a_0\sqrt{N^2 - N + 1}$. The surface energy density of the unstrained stepped surface is therefore

$$\gamma_s(\theta) = \frac{N}{\sqrt{N^2 - N + 1}} \frac{\omega_0}{a_0}$$

for $2 \leq N \leq \infty$, where the macroscopic slope is given by $\tan \theta = \frac{\sqrt{3}}{2N - 1}$. Substituting θ for N in this equation yields a non-dimensionalised surface energy density of

$$\bar{\gamma}_s(\theta) = \cos \theta + \frac{1}{\sqrt{3}} |\sin \theta| \tag{F-1}$$

for $|\theta| \leq \frac{\pi}{6}$. For small angles this can be written to second order as $\bar{\gamma}_s(\theta) = 1 + \frac{1}{\sqrt{3}} |\theta| - \frac{1}{2}\theta^2$. Comparison with (6-5) gives $\gamma_0 = 1$, $\gamma_1 = 0.577$ and $\gamma_2 = -1$ and therefore the surface stiffness is predicted to be $\hat{\gamma} = 0$.

F.2 An LJ+BO surface

A similar simplistic treatment for estimating the surface energy can be utilised for the LJ+BO potential. The major difference here is that there is a surface stress and the surface undergoes an elastic relaxation due to this. A flat surface was fully analysed with elastic relaxation in section 2.4 and predicted that $\bar{\gamma}_s = 0.21$ at zero applied strain. An atom on the surface has a coordination number of 4 and has two (shared) 4-4 bonds with other surface atoms and two 4-6 bonds with bulk atoms (coordination number of 6). The change in potential energy of these bonds with respect to the energy of a bulk bond ($-\omega_0$) is shown in Table F.1

Bond type (i-j)	Change in energy from bulk bond, $\Delta V_{ij} = 2 - b_i - b_j$
3-4	$-0.406 \omega_0$
3-5	$-0.313 \omega_0$
3-6	$-0.222 \omega_0$
4-4	$-0.368 \omega_0$
4-5	$-0.275 \omega_0$
4-6	$-0.184 \omega_0$
5-6	$-0.091 \omega_0$
6-6	0

Table F.1 : The difference between the energy of a LJ+BO bond in the bulk (with full coordination, 6-6) and a bond near the surface (with reduced coordination, i-j).

The energies of poorly coordinated atoms are much lower (stronger) than that of a bulk bond at the bulk lattice spacing (although the total energy per atom is lower in the bulk due to the greater number of bonds). The non-dimensionalised surface energy density on a flat LJ+BO surface is $1 + 2x \frac{1}{2} \Delta V_{44} + 2\Delta V_{46} = 0.264$. This compares quite favourably with the fully relaxed value of 0.21. Therefore we proceed as in section F.1 and look at the change in energy due to the introduction of a step. The atom at the base of the step has a coordination of 5 and the atom at the top of the step has a coordination of 3. The surface energy of a surface of N atoms will therefore have an energy of $0.264(N - 4) + 4 + \Delta V_{34} + \Delta V_{35} + \Delta V_{36} + \Delta V_{44} + \Delta V_{45} + 4\Delta V_{46} + 3\Delta V_{56} = 0.264N + 0.351$. The surface energy density is thus

$$\bar{\gamma}_s(\theta) = \frac{0.264N + 0.351}{\sqrt{N^2 - N + 1}} = 0.264 \cos \theta + 0.558 |\sin \theta| \quad (\text{F-2})$$

Comparison with (6-5) gives $\gamma_0 = 0.264$, $\gamma_1 = 0.558$ and $\gamma_2 = -0.264$ and therefore the surface stiffness is again predicted to be $\hat{\gamma} = 0$.

G : Newton-Raphson scheme for atomistic energy minimization

The total energy (3-6) can be approximated as a quadratic using Taylors expansion

$$E(\underline{d}_0 + \underline{\Delta d}) = E(\underline{d}_0) + \left. \frac{\partial E}{\partial d_i} \right|_{\underline{d}=\underline{d}_0} \underline{\Delta d} + \frac{1}{2} \underline{\Delta d}^T \frac{\partial^2 E}{\partial d_i \partial d_j} \underline{\Delta d}, \quad (\text{G-1})$$

where \underline{d}_0 is the initial guess for the degrees of freedom (DOF) vector, $\underline{\Delta d}$ is the change of DOF. Minimizing the energy, one can obtain the simultaneous linear equations as follows

$$[K][D] = [F], \quad (\text{G-2})$$

where

$$\text{the components of the stiffness matrix are } k_{ij} = \frac{\partial^2 E}{\partial d_i \partial d_j},$$

$$\text{the components of the force vector are } f_i = -\frac{\partial E}{\partial d_i},$$

the components of the change in the DOF vector are Δd_i .

In this case, the local components for the atomistic region are determined by the interaction between two bonded atoms. All local components can then be superposed into a global matrix or vector. The detailed procedure of forming the local simultaneous linear equations will be introduced below.

There are three kinds of the interatomic interaction: (1) both atoms are located within the atomistic region, (2) one atom within the atomistic region and the other on the boundary, (3) both atoms on the boundary. For case (1), the interatomic potential can be written as

$$e_a = \omega_0 \left[\left(\frac{r_0}{r_{ij}} \right)^{12} - (b_{ij1} + b_{ij2}) \left(\frac{r_0}{r_{ij}} \right)^6 \right]. \quad (\text{G-3})$$

Let $\alpha = \frac{x_j - x_i}{l} = \frac{\Delta x}{l}$ and $\beta = \frac{y_j - y_i}{l} = \frac{\Delta y}{l}$, where $l = \sqrt{(x_j - x_i)^2 + (y_j - y_i)^2}$ is the distance between atom i and j . One can then write

$$[K_a^e][D_a^e] = [F_a^e], \quad (\text{G-4})$$

where

$$[K_a^e] = \begin{bmatrix} \frac{A_1}{l} \beta^2 + A_2 \alpha^2 & -\frac{A_1}{l} \alpha \beta + A_2 \alpha \beta & -\frac{A_1}{l} \beta^2 - A_2 \alpha^2 & \frac{A_1}{l} \alpha \beta - A_2 \alpha \beta \\ -\frac{A_1}{l} \alpha \beta + A_2 \alpha \beta & \frac{A_1}{l} \alpha^2 + A_2 \beta^2 & \frac{A_1}{l} \alpha \beta - A_2 \alpha \beta & -\frac{A_1}{l} \alpha^2 - A_2 \beta^2 \\ -\frac{A_1}{l} \beta^2 - A_2 \alpha^2 & \frac{A_1}{l} \alpha \beta - A_2 \alpha \beta & \frac{A_1}{l} \beta^2 + A_2 \alpha^2 & -\frac{A_1}{l} \alpha \beta + A_2 \alpha \beta \\ \frac{A_1}{l} \alpha \beta - A_2 \alpha \beta & -\frac{A_1}{l} \alpha^2 - A_2 \beta^2 & -\frac{A_1}{l} \alpha \beta + A_2 \alpha \beta & \frac{A_1}{l} \alpha^2 + A_2 \beta^2 \end{bmatrix},$$

$$[F_a^e]^T = A_1 [\alpha, \beta, -\alpha, -\beta],$$

$$[D_a^e]^T = [u_{xi}, u_{yi}, u_{xj}, u_{yj}],$$

with $A_1 = \left. \frac{\partial e_a}{\partial r} \right|_{r=l}$.

For cases (2) and (3), atom i or j or both is located at the boundary. The degrees of freedom will be exchanged from atomic displacement to d_x and d_z . For example, one may assume that atom i is located on boundary. One rewrites the terms of (G-4) as follows

$$[D_a^e]^T = [\Delta d_x, \Delta d_z, u_{xj}, u_{yj}],$$

$$[F_a^e]^T = \left[-\frac{\partial e_a}{\partial d_x}, -\frac{\partial e_a}{\partial d_z}, \frac{\partial e_a}{\partial x_j}, \frac{\partial e_a}{\partial y_j} \right],$$

where

$$\frac{\partial e_a}{\partial d_x} = \frac{\partial e_a}{\partial x_i^b} \cdot \frac{\partial x_i^b}{\partial d_x} + \frac{\partial e_a}{\partial y_i^b} \cdot \frac{\partial y_i^b}{\partial d_x} = -A_1 \alpha \frac{\partial x_i^b}{\partial d_x} - A_1 \beta \frac{\partial y_i^b}{\partial d_x},$$

$$\frac{\partial e_a}{\partial d_z} = \frac{\partial e_a}{\partial x_i^b} \cdot \frac{\partial x_i^b}{\partial d_z} + \frac{\partial e_a}{\partial y_i^b} \cdot \frac{\partial y_i^b}{\partial d_z} = -A_1 \alpha \frac{\partial x_i^b}{\partial d_z} - A_1 \beta \frac{\partial y_i^b}{\partial d_z},$$

$$\frac{\partial e_a}{\partial x_j} = A_1 \alpha,$$

$$\frac{\partial e_a}{\partial y_j} = A_1 \beta,$$

and

$$\frac{\partial x_i^b}{\partial d_x} = \frac{2 \sin \theta}{\pi ER} [1 - (1 + \nu) \cos^2 \theta] = a_{xx},$$

$$\frac{\partial y_i^b}{\partial d_x} = \frac{2 \cos \theta}{\pi ER} [(1 + \nu) \sin^2 \theta - 1] = a_{yx},$$

$$\frac{\partial x_i^b}{\partial d_z} = \frac{2 \cos \theta}{\pi ER} [\nu - (1 + \nu) \sin^2 \theta] = a_{xz},$$

$$\frac{\partial y_i^b}{\partial d_z} = \frac{2 \sin \theta}{\pi ER} [-1 - (1 + \nu) \cos^2 \theta] = a_{yz},$$

where $R = \sqrt{(x_i - x_0)^2 + (y_i - y_0)^2}$ is the distance between atom i and the step, θ is the angle between R and the z -direction, and a_{xx} , a_{yx} , a_{xz} and a_{yz} all are constants.

The local stiffness matrix is

$$[K_a^e] = \begin{bmatrix} \frac{\partial^2 e_a}{\partial d_x^2} & \frac{\partial^2 e_a}{\partial d_x \partial d_z} & \frac{\partial^2 e_a}{\partial d_x \partial x_j} & \frac{\partial^2 e_a}{\partial d_x \partial y_j} \\ \frac{\partial^2 e_a}{\partial d_x \partial d_z} & \frac{\partial^2 e_a}{\partial d_z^2} & \frac{\partial^2 e_a}{\partial d_z \partial x_j} & \frac{\partial^2 e_a}{\partial d_z \partial y_j} \\ \frac{\partial^2 e_a}{\partial d_x \partial x_j} & \frac{\partial^2 e_a}{\partial d_z \partial x_j} & \frac{\partial^2 e_a}{\partial x_j^2} & \frac{\partial^2 e_a}{\partial x_j \partial y_j} \\ \frac{\partial^2 e_a}{\partial d_x \partial y_j} & \frac{\partial^2 e_a}{\partial d_z \partial y_j} & \frac{\partial^2 e_a}{\partial x_j \partial y_j} & \frac{\partial^2 e_a}{\partial y_j^2} \end{bmatrix},$$

where

$$\frac{\partial^2 e_a}{\partial d_x^2} = a_{xx}^2 \frac{\partial^2}{\partial x_i^{b2}} + 2a_{xx}a_{yx} \frac{\partial^2}{\partial x_i^b \partial y_i^b} + a_{yx}^2 \frac{\partial^2}{\partial y_i^{b2}},$$

$$\frac{\partial^2 e_a}{\partial d_x \partial d_z} = a_{xx}a_{xz} \frac{\partial^2}{\partial x_i^{b2}} + (a_{xx}a_{yz} + a_{yx}a_{xz}) \frac{\partial^2}{\partial x_i^b \partial y_i^b} + a_{yx}a_{yz} \frac{\partial^2}{\partial y_i^{b2}},$$

$$\frac{\partial^2 e_a}{\partial d_z^2} = a_{xz}^2 \frac{\partial^2}{\partial x_i^{b2}} + a_{xz}a_{yz} \frac{\partial^2}{\partial x_i^b \partial y_i^b} + a_{yz}^2 \frac{\partial^2}{\partial y_i^{b2}},$$

$$\frac{\partial^2 e_a}{\partial d_x \partial x_j} = a_{xx} \frac{\partial^2}{\partial x_i^b \partial x_j} + a_{yx} \frac{\partial^2}{\partial y_i^b \partial x_j},$$

$$\frac{\partial^2 e_a}{\partial d_x \partial y_j} = a_{xx} \frac{\partial^2}{\partial x_i^b \partial y_j} + a_{yx} \frac{\partial^2}{\partial y_i^b \partial y_j},$$

$$\frac{\partial^2 e_a}{\partial d_z \partial x_j} = a_{xz} \frac{\partial^2}{\partial x_i^b \partial x_j} + a_{yz} \frac{\partial^2}{\partial y_i^b \partial x_j},$$

$$\frac{\partial^2 e_a}{\partial d_z \partial y_j} = a_{xz} \frac{\partial^2}{\partial x_i^b \partial y_j} + a_{yz} \frac{\partial^2}{\partial y_i^b \partial y_j},$$

$$\frac{\partial^2 e_a}{\partial x_j^2} = \frac{A_1}{l} \beta^2 + A_2 \alpha^2,$$

$$\frac{\partial^2 e_a}{\partial x_j \partial y_j} = -\frac{A_1}{l} \alpha \beta + A_2 \alpha \beta,$$

$$\frac{\partial^2 e_a}{\partial y_j^2} = \frac{A_1}{l} \alpha^2 + A_2 \beta^2.$$

with $A_2 = \left. \frac{\partial^2 e_a}{\partial r^2} \right|_{r=l}$. Note that the motions of atoms on the boundary are constrained by continuum theory as opposed to Lattice Statics.

REFERENCES:

- [1]. Grinfeld, M.A.(1993), The Stress Driven Instability in Elastic Crystals: Mathematical Models and Physical Manifestations, *J. Nonlinear Sci.*, 3, pp35-83.
- [2]. Srolovitz, D.J.(1989), On the Stability of Surface of Stressed Solids, *Acta Metall.*, 37, pp621-625.
- [3]. Kordos, P. and Novak, J., eds. (1998), *Heterostructure Epitaxy and Devices*, Boston: Kluwar.
- [4]. Gao, H. and Nix, W.D. (1999), Surface Roughening of Heteroepitaxial Thin Films, *Annu.Rev.Mater.Sci.*, 29, pp173-209.
- [5]. Cocks, A.C.F., Gill, S.P.A. and Pan, J.(1999), Modeling Microstructure Evolution in Engineering Materials, *Advances in Applied Mechanics*, 36, pp81-162.
- [6]. Suo, Z.(1997), Motions of Microscopic Surfaces in Materials, *Advances in Applied Mechanics*, 33, pp193-294.
- [7]. Gill, S.P.A., Cornforth, M.G. and Cocks, A.C.F.(2001), Modelling Microstructure Evolution in Engineering Materials, *International Journal of Plasticity*, 17(4), pp 669-690.
- [8]. Shenoy, V.B. and Freund, L.B.(2002), A Continuum Description of the Energetics and Evolution of Stepped Surfaces in Strained Nanostructures, *Journal of the Mechanics and Physics of Solids*, 50, pp1817-1841.
- [9]. Tersoff, J.(1988), New Empirical Approach for the Structure and Energy of Covalent Systems, *Physical Review B*, 37(12), pp6991-7000.
- [10]. Battaile, C.C. and Srolovitz, D.J.(2002), Kinetic Monte Carlo Simulation of Chemical Vapor Deposition, *Annu. Rev. Mater. Res.*, 32 pp297-319.
- [11]. Dong, L., Schnitker, J., Smith, R.W. and Srolovitz, D.J.(1998), Stress Relaxation and Misfit Dislocation in the Growth of Misfitting Films: A Molecular Dynamics Simulation Study, *J. Appl.Phys.*, 83(1), pp217-227.
- [12]. Kohlhoff, S., Gumbsch, P. and Fischmeister, H.F.(1991), Crack Propagation in b.c.c Crystals Studied with a Combined Finite-Element and Atomistic Model, *Philosophical Magazine A*, 64(4), pp851-878.
- [13]. Tadmor, E.B., Ortiz, M. and Phillips, R.(1996), Quasicontinuum Analysis of Defects in Solids, *Philosophical Magazine A*, 73(6), pp1529-1563.

- [14]. Shenoy, V.B., Miller, R., Tadmor, E.B., Rodney, D., Phillips, R. and Ortiz, M.(1999), An Adaptive Finite Element Approach to Atomic-scale Mechanics - the Quasicontinuum Method, *Journal of the Mechanics and Physics of Solids*, 47, pp611-642.
- [15]. Rudd, R.E. and Broughton, J.Q.(1998), Coarse Grained Molecular Dynamics and the Atomic Limit of Finite Elements, *Physical Review B*, 58(10), ppR5893-5896.
- [16]. Broughton, J.Q., Abraham, F.F, Bernstein, N. and Kaxiras, E.(1999), Concurrent Coupling of Length Scales: Methodology and Application, *Physical Review B*, 60(4), pp2391-2403.
- [17]. Ortiz, M. and Phillips, R.(1999), Nanomechanics of Defects in Solids, *Advances in Applied Mechanics*, 36, pp1-79.
- [18]. Phillips, R.(2001), *Crystals, Defects and Microstructures – Modeling Across Scales*, Cambridge University.
- [19]. Marchenko, V.I. and Parshin, A.Ya.(1980), Elastic Properties of Crystal Surfaces, *Sov. Phys. JETP* 52(1), pp129-131.
- [20]. Rickman, J.M. and Srolovitz, D.J.(1993), Defect Interactions on Solid Surfaces, *Surface Science*, 284, pp211-221.
- [21]. Stewart, J., Pohland O. and Gibson, J. M.(1994), Elastic-displacement Field of an Isolated Surface Step, *Physical Review B*, 49(19), pp13848-13858.
- [22]. Kukta, R.V. and Bhattacharya, K.(2002), A Micromechanical Model of Surface Steps, *Journal of the Mechanics and Physics of Solids*, 50, pp615-649.
- [23]. Professor Jack M. Blakely's research group, Surface science research at Cornell University Materials Science and Engineering Department and Materials Science Center, web reference: <http://people.ccmr.cornell.edu/~blakely/>.
- [24]. Nielsen, J.F.(2001), Energetically and kinetically Driven Step Formation and Evolution on Silicon Surface, PhD Thesis, Ohio State University.
- [25]. Tersoff, J., Phang, Y.H., Zhang, Z. and Lagally, M.G.(1995), Step-Bunching Instability of Vicinal Surfaces under Stress, *Physical Review Letters*, 75(14), pp2730-2733.
- [26]. Burton, W.K., Cabrera, N. and Frank, F.C.(1951), The Growth of Crystals and the Equilibrium Structure of their Surfaces, *Phil. Trans. Roy. Soc. A*, 243, pp299-358.
- [27]. Xiang, Y. and E, W.(2004), Misfit Elastic Energy and a continuum Model for Epitaxial Growth with Elasticity on Vicinal Surfaces, *Physical Review B*, 69, pp035409-1-16.

-
- [28]. Luth, H.(1997), Surfaces and Interfaces of Solid Materials, Third Edition, Updated Printing, Springer-Verlag.
- [29]. Bengu, E., Plass, R. and Marks, L.D.(1996), Imaging the Dimers in Si(111)-(7x7), Physical Review Letters, 77(20), pp4226-4228.
- [30]. Attard, G. and Barnes, C.(1998), Surfaces, Oxford University Press Inc., New York.
- [31]. Monch, W.(1995), Semiconductor Surfaces and Interfaces, Second Edition, Springer-Verlag.
- [32]. Jeong, H. and Williams, E.D.(1999), Steps on Surfaces: Experiment and Theory, Surface Science Reports, 34, pp171-294.
- [33]. Asaro, R.J. and Tiller, W.A.(1972), Interface Morphology Development during Stress Corrosion Cracking: Part I. Via Diffusion, Metall. Trans. 3, pp1789-1796.
- [34]. Grinfeld, M.A.(1986), Instability of the Separation Boundary between Non-hydrostatically Stressed Elastic Solid and Melt, Sov.Phys.Dokl. 31, pp831-834.
- [35]. Freund, L.B.(1995), Evolution of Waviness on the Surface of a Strained Elastic Solid due to Stress-Driven Diffusion, International Journal of Solids and Structures, 32(6/7), pp911-923.
- [36]. Gao, H.(1991), Morphological Instabilities Along Surfaces of Anisotropic Solid, In Modern Theory of Anisotropic Elasticity and Applications, ed. JJ Wu, TCT Ting, DM Barnett, pp139-150, Philadelphia: SIAM.
- [37]. Gao, H.(1991), A boundary Perturbation Analysis for Elastic Inclusions and Interfaces, International Journal of Solids and Structures, 28(6), pp703-725.
- [38]. Zhang, Y.W., Bower, A.F.(1999), Numerical Simulations of Island Formation in a Coherent Strained Epitaxial Thin Film System, Journal of the Mechanics and Physics of Solids, 47 pp2273-2297.
- [39]. Long, F., Gill, S.P.A. and Cocks, A.C.F.(2001), Effect of Surface-Energy Anisotropy on the Kinetics of Quantum Dot Formation, Physical Review B, 64(12), 121307(R)-1-4.
- [40]. Starrost, F. and Carter, E.A.(2002), Modeling the Full Monty: Baring the Nature of Surfaces across Time and Space, Surface Science, 500, pp323-436.
- [41]. Daw, M. S. and Baskes, M. I.(1983), Semiempirical, Quantum Mechanical Calculation of Hydrogen Embrittlement in Metals, Physical Review Letters, 50, pp1285-1288.
- [42]. Abell, G.C.(1995), Empirical Chemical Pseudopotential Theory of Molecular and Metallic Bonding, Physical Review B, 31(10), pp6184-6196.

- [43]. Stillinger, F. and Weber, T.(1985), Computer Simulation of Local Order in Condensed Phases of Silicon, *Physical Review B*, 31(8), pp5262-5271.
- [44]. Dodson, B. W.(1986), Evaluation of the Stillinger-Weber Classical Interaction Potential for Tetragonal Semiconductors in Nonideal Atomic Configurations, *Physical Review B*, 33(10), pp7361-7363.
- [45]. Landman, Uzi, Luedtke, W. D. et al.(1986), Faceting at the Silicon (100) Crystal-melt Interface: Theory and Experiment, *Physical Review Letter*, 56(2), pp155-158.
- [46]. Abraham, F.F. and Broughton, J.Q.(1986), Pulsed Melting of Silicon (111) and (100) Surfaces Simulated by Molecular Dynamics, *Physical Review Letter*, 56(7), pp734-737.
- [47]. Biswas, R. and Hamann, D. R.(1985), Interatomic Potentials for Silicon Structural Energies, *Physical Review Letter*, 55(19), pp2001-2004.
- [48]. Tersoff, J.(1986), New Empirical Model for the Structural Properties of Silicon, *Physical Review Letter*, 56, pp632-635.
- [49]. Rudd, R.E. and Broughton, J.Q.(2000), Concurrent coupling of Length Scales in Solid State Systems, *Phys. Stat. Sol. (b)* 217, pp251-291.
- [50]. Ozkan, C.S., Nix, W.D. and Gao, H.(1997), Strain relaxation and defect formation in heteroepitaxial $Si_{1-x}Ge_x$ films via surface roughening induced by controlled annealing experiments, *Appl. Phys. Lett.* 70, pp2247-2249.
- [51]. Floro, J.A., Chason, E., Freund, L.B., Twisten, R.D., Hwang, R.Q. and Lucadamo, G.A.(1999), Evolution of coherent islands in $Si_{1-x}Ge_x / Si(001)$, *Physical Review B*, 59(3), pp1990-1998.
- [52]. Brihuega, I., Custance, O., Perez, R. and Gomez-Rodriguez, J.M.(2005), Intrinsic Character of the (3×3) to $(\sqrt{3} \times \sqrt{3})$ Phase Transition in Pb/Si(111), *Physical Review Letters*, 94, pp046101-1-4. And <http://focus.aps.org/story/v15/st6>
- [53]. Pohland, O., Tong, X. and Gibson, J.M.(1993), Imaging Subsurface Strain at Atomic Steps on Si(111), *J.Vac. Sci. Technol. A*, 11(4), pp1837-1842.
- [54]. Martinez, R.E., Augustyniak, W.M. and Golovchenko, J.A.(1990), Direct Measurement of Crystal Surface Stress, *Physical Review Letters*, 64(9), pp1035-1038.
- [55]. Israeli, N. and Kandel, D.(2000), Decay of One-dimension Modulations. *Physical Review B*, 62(20), pp13 707-13 717.
- [56]. Ozdemir, M. and Zangwill, A.(1990), Morphological Equilibration of a Corrugated Crystalline Surface, *Physical Review B*, 42(8), pp5013-5024.

- [57]. Shenoy, V. B., Ramasubramaniam, A. and Freund, L. B.(2003), A Variational Approach to Nonlinear Dynamics of Nanoscale Surface Modulations, *Surface Science*, 529 (1-3), pp365- 383.
- [58]. Friesecke, G. and James, R.D.(2000), A Scheme for the Passage from Atomic to Continuum Theory for Thin Films, Nanotubes and Nanorods, *Journal of the Mechanics and Physics of Solids*, 48, pp1519-1540.
- [59]. Knap, J. and Ortiz, M.(2001), An Analysis of the Quasicontinuum Method, *Journal of the Mechanics and Physics of Solids*, 49, pp1899-1923.
- [60]. Hardikar, K., Shenoy, V. and Philips, R.(2001), Reconciliation of Atomic-level and Continuum Notions Concerning the Interaction of Dislocations and Obstacles, *Journal of the Mechanics and Physics of Solids*, 49, pp1951-1967.
- [61]. Ortiz, M., Cuitino, A.M., Knap, J. and Koslowski, M.(2001), Mixed Atomistic-Continuum Models of Material Behaviour: The Art of Transcending Atomistics and Informing Continua, *MRS Bulletin*, 26(3), pp216-221.
- [62]. Miller, R., Tadmor, E.B., Phillips, R. and Ortiz, M.(1998), Quasicontinuum Simulation of Fracture at the Atomic Scale, *Modeling and Simulation in Materials Science and Engineering*, 6, pp607-638.
- [63]. Shenoy, V.B., Miller, R., Tadmor, E.B., Phillips, R. and Ortiz, M.(1998), Quasicontinuum Models of Interfacial Structure and Deformation, *Physical Review Letters*, 80(4), pp742-745.
- [64]. Tadmor, E.B., Smith, G.S., Bernstein, N. and Kaxiras, E.(1999), Mixed Finite Element and Atomistic Formulation for Complex Crystals, *Physical Review B*, 59(1), pp235-245.
- [65]. Phillips, R., Dittrich, M. and Schulten, K.(2002), Quasicontinuum Representations of Atomic-Scale Mechanics: From Proteins to Dislocations, *Annu. Rev. Mater. Res.*, 32, pp219-33.
- [66]. E, W. and Huang, Z.(2001), Matching Conditions in Atomistic-Continuum Modeling of Materials, *Physical Review Letters*, 87(13), pp135501-1-135501-4.
- [67]. Cai, W., Koning, M., Bulatov, V.V. and Yip, S.(2000), Minimizing Boundary Reflections in Coupled-Domain Simulations, *Physical Review Letters*, 85(15), pp3213-3216.
- [68]. Voter, A.F., Montalenti, F and Germann, T.C.(2002), Extending the Time Scale in Atomistic Simulation of Materials, *Annu. Rev. Mater. Res.*, 32, pp321-346.

-
- [69]. Voter, A.F.(1986), Classically Exact Overlayer Dynamics: Diffusion of Rhodium Clusters on Rh(100), *Physical Review B*, 34(10), pp6819-6829.
- [70]. Fichthorn, K.A. and Weinberg, W.H.(1991), Theoretical Foundations of Dynamical Monte Carlo Simulations, *J. Chem. Phys.* 95(2), pp1090-1096.
- [71]. Biehl, M. and Much, F.(2003) Off-lattice Kinetic Monte Carlo Simulations of Stranski-Krastanov-like Growth, *Quantum Dots: Fundamentals, Applications, and Frontiers*, June 2003, proceedings to be published by Kluwer.
- [72]. Biehl, M., Ahr, M., Kinzel, W. and Much, F.(2003), Kinetic Monte Carlo Simulations of Heteroepitaxial Growth, *Thin Solid Film*, 428, pp52-55.
- [73]. Gill, S.P.A., unpublished paper.
- [74]. Shilkrot, L.E. and Srolovitz, D.J.(1996), Elastic Field of a Surface Step: Atomistic simulations and Anisotropic Elastic Theory, *Physical Review B*, 53(16), pp11 120-11 127.
- [75]. Srolovitz, D.J. and Hirth, J.P.(1991), Elastic Analysis of the Energy and Relaxation of Stepped Surfaces, *Surface Science*, 255, pp111-119.
- [76]. Timoshenko, S.P. and Goodier, J.N.(1970), *Theory of Elasticity (Third Edition)*, McGraw-Hill.
- [77]. Ottosen, N. and Petersson, H. (1992), *Introduction to the Finite Element Method*, Prentice Hall.
- [78]. Shewchuk, J.R., *Triangle: Engineering a 2D Quality Mesh Generator and Delaunay Triangulator*, Triangle is freely available on the Web at <http://www.cs.cmu.edu/~quake/triangle.html>.
- [79]. Khor, K.E. and Sarma, S.D.(2000), Quantum Dot Self-assembly in Growth of Strained-layer Thin Films: A Kinetic Monte Carlo Study, *Physical Review B*, 62(24), pp16 657-16 664.
- [80]. Meixner, M., Scholl, E., Shchukin, V.A. and Bimberg, D.(2001), Self-assembled Quantum Dots: Crossover from Kinetically Controlled To Thermodynamically Limited Growth, *Physical Review Letters*. 87(23), pp236101-1-4.
- [81]. Spjut, H. and Faux, D.A.(1994), Computer Simulation of Strain-induced Diffusion Enhancement of Si Adatoms on the Si(100) Surface, *Surface Science*, 306, pp233-239.
- [82]. Schroeder, M. and Wolf, D.E.(1997), Diffusion on Strained Surfaces, *Surface Science*, 375, pp129-140.
- [83]. Jensen, F.(1999), *Introduction to Computational Chemistry*, John Wiley & Son.

- [84]. Shewmon, P.(1989), Diffusion in Solids (Second Edition), A Publication of The Minerals, Metals & Materials Society.
- [85]. Cammarata, R.C.(1994), Surface and Interface Stress Effects in Thin Films. Progress in Surface Science, 46(1), pp1-38.
- [86]. Dennery, P.(1972), An Introduction to Statistical Mechanics, George Allen & Unwin Ltd.
- [87]. Sornette, D.(2004), Critical Phenomena in Natural Sciences – Chaos, Fractals, Selforganization and Disorder: Concepts and Tools (Second Edition), Springer.
- [88]. Kukta, R.V., Peralta, A. and Kouris, D.(2002), Elastic Interaction of Surface Steps: Effect of Atomic-scale Roughness, Physical Review Letters, 88(18), pp186102-1-4.
- [89]. Gill, G.P.A., Spencer, P.E. and Cocks, A.C.F.(2004), A Hybrid Continuum/kinetic Monte Carlo Model for Surface Diffusion, Materials Science and Engineering A, 365, pp66-72.
- [90]. Dupuy, L., Tadmor, E. B., Miller, R. and Phillips, R. (2005), Finite Temperature Quasicontinuum: Molecular Dynamics Simulations without All the Atoms, to appear in Phys. Rev. Lett.
- [91]. Gill, G.P.A., private notes.
- [92]. Freund, L.B. and Suresh, S. (2003), Thin Film Materials- Stress, Defect Formation and Surface Evolution, Cambridge University Press.
- [93]. Ozkan, C.S., Nix, W.D. and Gao, H. (1997), Anisotropic Behaviour of Surface Roughening in Lattice Mismatched Heteroepitaxial Thin Films, Mat. Res. Soc. Symp. Proc., 436, pp487-492.
- [94]. Zhao, Y.P., Wang, G.C. and Lu, T.M. (2001), Characterization of Amorphous and Crystalline Rough Surface: Principles and Applications, Experimental Methods in the Physical Sciences (Editors: Celotta, R. and Lucatorto, T.), Volume 37, Academic Press.
- [95]. Zhao, Y.P., Yang, H.N., Wang, G.C. and Lu, T.M. (1998), Diffraction from Diffusion-barrier-induced Mound Structures in Epitaxial Growth Fronts, Physical Review B, 57(3), pp1922-1934.
- [96]. Yang, H.N., Zhao, Y.P., Chan, A., Lu, T.M. and Wang, G.C. (1997), Sampling-induced Hidden Cycles in Correlated Random Rough Surfaces, Physical Review B, 56(7), pp4224-4232.

-
- [97]. Cullis, A.G., Robbins, D.J., Pidduck, A.J. and Smith, P.W. (1992), The Characteristics of Strain-modulated Surface Undulations Formed upon Epitaxial $Si_{1-x}Ge_x$ Alloy Layers on Si, *Journal of Crystal Growth*, 123, pp333-343.
- [98]. LeGouse, F.K., Reuter, M.C., Tersoff, J., Hammar, M. and Tromp, R.M. (1994), Cyclic Growth of Strain-Relaxed Islands, *Physical Review Letters*, 73(2), pp300-303.
- [99]. Gopal, V., Vasiliev, A.L. and Kvam, E.P. (2001), Misfit Dislocation Introduction During the Epitaxial Growth of InAs Islands on GaP, *Mat. Res. Soc. Symp. Proc.*, 673, pp4.3.1-4.3.6.
- [100]. Gopal, V., Vasiliev, A.L. and Kvam, E.P. (2001), Strain Relaxation and Dislocation Introduction in Lattice-Mismatched InAs/GaP Heteroepitaxy, *Philosophical Magazine A*, 81(10), pp2481-2501.
- [101]. Kassner, M.E., Nemat-Nasser, S., Suo, Z., Bao, G., Barbour, J.C., Brinson, L.C., Espinosa, H., Gao, H., Granick, S, Gumbsch, P., Kim, K., Knauss, W., Kubin, L., Langer, J., Larson, B.C., Mahadevan, L., Majumdar, A., Torquato, S., and Swol, F. (2005), *New Directions in Mechanics, Mechanics of Materials*, 37, pp231-259.
- [102]. Gao, H. (1994), Some General Properties of Stress-driven Surface Evolution in a Heteroepitaxial Thin Film Structure, *J. Mech, Phys. Solids*, 42(5), pp741-772.
- [103]. Nix, W.D. (1989), Mechanical Properties of Thin Films, *Metall. Trans. A*, 20, pp2217-2245.
- [104]. Beltz, G.E. and Freund, L.B. (1993), Nucleation of a Dislocation Loop at the Free Surface of a Crystal, *Physica Status Solidi B*, 180, pp303-313.
- [105]. Gao, H., Ozkan, C.S., Nix, W.D., Zimmerman, J.A. and Freund, L.B. (1999), Atomistic Models of Dislocation Formation at Crystal Surface ledges in $Si_{1-x}Ge_x/Si(100)$ Heteroepitaxial Thin Films, *Philosophical Magazine A*, 79(2), pp349-370.
- [106]. Zimmerman, J.A. and Gao., H (1996), Investigation of Relationships between Dislocations and Crystal Surface Ledges, *Mat. Res. Soc. Symp. Proc.* 399, pp401-406.
- [107]. Liu, Z.J. and Shen, Y.G. (2003), Roughening Kinetics of Thin Films in the Presence of both Stress and Ehrlich-Schwobel barrier, *Applied Physics Letters*, 83(26), pp5404-5406.
- [108]. Lam, C.H., Lee, C.K. and Sander, L.M. (2002), Competing Roughening Mechanisms in Strained Heteroepitaxy: A Fast Kinetic Monte Carlo Study, *Physical Review Letters*, 89(21), pp216102-1-4.

- [109]. Xu, G. and Zhang, C. (2003), Analysis of Dislocation Nucleation from a Crystal Surface Based on the Peierls-Nabarro Dislocation Model, *Journal of the Mechanics and Physics of Solids*, 51, pp1371-1394.
- [110]. Israeli, N. and Kandel, D. (2002), Comment on “Nonclassical Smoothing of Nanoscale Surface Corrugations”, *Physical Review Letters*, 88(16), pp169601-1.
- [111]. Erlebacher, J., Aziz, M.J. Chason, E., Sinclair, M.B. and Floro, J.A. (2000), Nonclassical Smoothing of Nanoscale Surface Corrugations, *Physical Review Letters*, 84(25), pp5800-5803.
- [112]. Gill, S.P.A., Spencer, P.E. and Cocks, A.C.F. (2005), Mixed KMC/Continuum Models for Surface Diffusion, *International Journal for Multiscale Computational Engineering*, 3(2) , pp239-256.
- [113]. Udink, C. and Frenkel, D. (1987), Orientational Order and Solid-liquid Coexistence in the Two-dimensional Lennard-Jones System, *Phys. Rev. B*, 35, pp6933-6939.